UNIVERSITY OF SOUTHAMPTON

FACULTY OF PHYSICAL SCIENCES AND ENGINEERING

Electronics and Computer Science

Nanoscale Raman Spectroscopy of graphene nanodevice structures

by

Taharh Zelai

Thesis for the degree of Doctor of Philosophy

July_2017

UNIVERSITY OF SOUTHAMPTON

ABSTRACT

FACULTY OF PHYSICAL SCIENCES AND ENGINEERING

Electronics and Computer Science

Doctor of Philosophy

NANOSCALE RAMAN SPECTROSCOPY OF GRAPHENE NANODEVICE STRUCTURES

Taharh Zelai

Graphene is an atomically-thin 2-dimentional layer of carbon atoms. Since 2004, it has been attracting significant attention for various type of device applications due to its unique properties. In particular, applications of graphene for micro- and nanoscale devices is one of the most demanded and promising research fields. For further advancement of technological flexibility in designing graphene nanodevices, introducing defects to graphene could be a useful method to modify its material properties. Therefore, how to control defects in graphene and how to observe the effects of defects are one of the most important issues. For instance, the defect formed on graphene has been observed to make influence on the charge carrier concentration. Moreover, the defect introduction to graphene will change the phase of the graphene from crystalline to amorphous.

Tip-enhanced Raman Spectroscopy (TERS) is a combination of Scanning Probe Microscopy (SPM) and micro-Raman spectroscopy. While micro Raman has played a crucial role to characterise graphene material properties at a microscale level, TERS is considered to be a powerful tool to investigate and characterise nanostructure devices, defect density, and doping with high spatial resolution down to sub 100 nm.

In this work my aim is to establish TERS measurement techniques for various types of graphene. Then the TERS is applied for evaluating defect density, edge properties and strain induced in the graphene nanoelectronic and nanoelectromechanical devices to investigate the physics of graphene nanodevices. I have started to optimise the TERS tools on graphene to achieve high spatial resolution. Then I have applied TERS for studying the stress and strain and defect formation on suspended graphene on SiNWs. The result shows that the peak position is shifted in the TERS spectra and additionally the local defects at the edge of SiNW have been observed

with a spatial resolution of ~ 100 nm. Then I have introduced defects using helium ion irradiation on graphene nanoribbon (GNR). TERS is used to study the graphene edges and irradiation boundary of in the graphene channels. I have succeeded in taking TERS spectra across the edge of the He-ion-irradiated region on graphene for the first time and confirmed that higher spatial resolution is achievable with TERS.

TABLE OF CONTENTS

DECLARATION OF AUTHORSHIP

I, Taharh Zelai, declare that this thesis and the work presented in it are my own and has been generated by me as the result of my own original research.

Nanoscale Raman Spectroscopy of graphene nanodevice structures

I confirm that:

1. This work was done wholly or mainly while in candidature for a research degree at this University;
2. Where any part of this thesis has previously been submitted for a degree or any other qualification at this University or any other institution, this has been clearly stated;
3. Where I have consulted the published work of others, this is always clearly attributed;
4. Where I have quoted from the work of others, the source is always given. With the exception of such quotations, this thesis is entirely my own work;
5. I have acknowledged all main sources of help;
6. Where the thesis is based on work done by myself jointly with others, I have made clear exactly what was done by others and what I have contributed myself;
7. [Delete as appropriate] None of this work has been published before submission[or] Parts of this work have been published as: [please list references below]:

Signed: .....

Date: .....

LIST OF PUBLICATIONS

Journals:

Iwasaki, Takuya, Zelai, Taharh, Ye, Sheng, Tsuchiya, Yoshishige, Chong, Harold and Mizuta, Hiroshi(2017) **Local hole doping concentration modulation on graphene probed by tip-enhanced Raman spectroscopy** *Carbon*, 111, pp. 67-73. (doi:10.1016/j.carbon.2016.09.068).

Conferences:

Taharh Zelai, Takuya Iwasaki, Stuart Boden, Harold Chong, Hiroshi Mizuta and Yoshishinge Tsuchiya; **Tip-Enhanced Raman characterization of He-ion-irradiated CVD graphene channels**, 43rd International Conference on Micro and NanoEngineering 2017, Braga, Portugal, 18-22 September.

Y Nagahisa, T. Zelai, J. Reynolds, L. Boodhoo, C. -C. Huang, D. Hewak, E. Tokumitsu, H. Mizuta and Y. Tsuchiya; **Tip-enhanced Raman Spectroscopy for Suspended Graphene Integrated with Silicon Nanowire Array**, Microscopy Microscience Congress 2015, Manchester, UK, 29 June - 2 July 2015

Seminar:

Taharh Zelai "**Tip-enhanced Raman Spectroscopy for graphene nanostructure**"; Nanoelectronics and Nanotechnology Group Annual Conference; Southampton, UK, 1 July 2016.

Taharh Zelai, Takuya Iwasaki, Stuart Boden, Harold Chong, Hiroshi Mizutaand YoshishigeTsuchiya;**Tip Enhanced Raman spectroscopy for Helium-ion-irradiated Graphene**, Nano Group Annual Conference, Southampton, UK, 4 July 2017.

ACKNOWLEDGEMENTS

I would like to express my sincerest gratitude to my supervisors, Dr Yoshishige Tsuchiya and Dr.Harold Chong for their encouragement and support during my PhD research. I would not have been able to produce this work without their active and enthusiastic approach to research. They give me this unique opportunity to the world of nanotechnology.

I would like to especially thank from my heart to my husband Dr Othman Hakami and my son Mohannad Hakami for their incredible patience, endless of motivation and support throughout my PhD work. From my heart, I would like to thank them for every minute they were in there to give me support and sweet word.

Special thanks to my family, my mum, my dad, my brothers, and my sisters whose unconditional love, support and wearied. I would like finally to thank my brother Mohammed Zelai for his support and help.

Special thanks must be given to Dr.Stuart Boden and Shi Xiaoqing for their time, help and suggestions. I would like to thank them for giving me the opportunity to use Helium ion microscopy. In addition, I would like to thanks, Prof. Daniel W.Hewak and Dr Kevin Chung-Che from Optoelectronics Research Centre (ORC)for providing us with graphene material.

I am grateful for all the technicians at Southampton Nanofabrication Centre, particularly Mr Peter Ayliffe, Mr Michael G. Perry, Zondy Webber and Mr Richard S. Kean. In addition, I extended my deepest thanks towards our collaborating researchers from the Japan Advanced Institute of Science and Technology (JAIST); Mr Takuya Iwasaki for useful discussions and assistance for setup Tip-Enhanced Raman Spectroscopy (TERS), and Dr Yuichi Nagahisa of Tokyo Institute of Technology.

I would like to thank my colleagues in Nano Research group for their help and suggestions through my PhD. I would like to express myself to thank Dr Sheng Ye, Dr Liam Boodhoo, Dr Jamie Reynolds, Dr Swe Zin Oo, Ms PG Hj Petra, Miss Illaria Sanzari for their assistance and support during my work.

I would like to acknowledge the Ministry of Higher Education of the Kingdom of Saudi Arabia (University of Jazan) for founding me and supporting my PhD.

LIST OF FIGURES

LIST OF ACRONYMS AND ABBREVIATION

0D,1D,2D,3D	Zero,one,Two,three dimensional
SPM	Scanning Probe Microscopy
AFM	Atomic Force Microscopy
STM	Scanning Tunneling Microscopy
FETs	Field-Effect Transistors
XPS	X-ray photoelectron spectroscope
Si	Silicon
TEM	Transmission Electron Microscopy
TERS	Tip-Enhanced Raman Spectroscopy
SEM	Scanning Electron Microscopy
FIB	Focused Ion Beam
HIM	Helium Ion Microscopy
SiO_2	Silicon dioxide
CVD	Chemical vapour deposition
EBL	Electron beam lithography
FWHM	Full width at half maximum
GNR	Graphene Nanoribbon
hBN	Hexagonal boron nitride
MIBK	Methyl isobutyl ketone
HMDS	Hexamethyldisilazane
MMA	Methyl methacrylate
NMP	N-Methyl-2-pyrrolidone
PMMA	Poly(methyl methacrylate)

RIE	Reactive ion etching
SE	Secondary electrons
SET	Single electron transistor
SV	Single vacancy
SW	Stone-Wales (defect)
Ar	Argon
Au	Gold
C	Carbon
H2	Hydrogen
He	Helium
N2	Nitrogen
Ni	Nickel
O2	Oxygen

LIST OF SYMBOLS

$I(D)$	Intensity of Raman 'D' peak
$I(D')$	Intensity of D' peak
$I(G)$	Intensity of Raman 'G' peak
LD	Average distance between point defects
r_S	Radius of the structurally disordered region in defective graphene
s	Exponent in the field assisted VRH
r_A	the surrounding active region
Vg	Gate voltage
a_1, a_2	Lattice vectors of graphene
b_1, b_2	Reciprocal lattice vectors of graphene
δ	vectors in real space
TA	Transverse acoustic
LA,	longitudinal acoustic
LO	longitudinal optic
iTO	in-plan transverse
oTO	out-of-plane transverse optic
$Eform$	Formation energy of defects
Ed	Total energy of graphene containing defects
$Ebulk$	Total energy of perfect graphene
E	Electric field
E_0	Vibrational state
α	Polarizability of the molecule
Δ	Tip-sample separation

r_{tip}	Radius of the tip
$g^2_{\lambda_{laser}}$	Enhancement factor of the excitation light
λ_{Raman}	Raman-scattered light
λ_{laser}	wavelength of excitation light
EF_{TERS}	Enhancement factor of the TERS signals
S_0	refers to the background signal
A_2	Scale factor
x_c	Position of the edge
w_2	Spatial resolution

Chapter 1: **Introduction**

1.1 Graphene

The concepts of nanotechnology and nanoscience have rapidly grown thanks to contribution of considerable numbers of researchers from various scientific fields. Consequently, nanotechnology is increasingly drawing the attentions of industries, academia, and engineering communities. Several applications have been developed at the nanometer scale, and one of these applications is nanoelectronics. In this field, the materials and technologies that are used in the semiconductor industry have been continuously improving and shrinking in size throughout the past decade.

Since the discovery of carbon nanofibers in 1972, a various allotrope of carbon have been studied, such as diamond, graphite, graphene, and nanotube. Graphene as a single atomically-thin planar layer of the two-dimensional form of carbon atoms[1, 2]was discovered in 2004 by Novoselov et al. in Manchester[1, 3].Since 2004, this material has attracted the interests and attention of scientists and engineers because of its extraordinary properties which make it ideal materials to solve many challenges in electronics devices. Graphene has a high mobility that can be reached to ~ 200,000 cm^2V^{-1} s^{-1} at room temperature, so it can be used for high-speed electronics devices[4]. From the mechanical properties point of view, graphene is mechanically strong materials with Young's modulus of ~1 TPa[5], and this can be used for flexible electronics devices. Moreover, the single atomic layer graphene has a high thermal conductivity of ~ $4.84x10^3$ to $5.30x10^3$ W/mK at room temperature [6].

Thanks to its excellent electronic properties and high mobility, graphene can be replaced from silicon (Si) electronic devices. Graphene is a great material providing a natural platform for the field-effect transistor (FET) [7].To use graphene as a switching device, however, zero band gap of graphene being hard to switch off in FETs. Therefore, as a solution engineering aspects can be used as inducing doping or strain [7, 8], downscale patterned graphene devices to one-dimensional (1D) graphene nanoribbons with smooth edges and the width of sub- 10nm has been reported in [9], it is lead to generate the effective quantum confinement which is open a tunable bandgap. At room temperature, this GNR transistor has been produced on-off ratios of ~10^7.The roadmap for graphene and other two-dimensional materials has been drawn by the researchers and industrialists as shown in

Fig.1.1 [10]. This roadmap starts from 2013 and extends over 12 years. The roadmap provides a guidance to researchers and the industries throughout the development of products based on graphene as a promising 2D materials. This roadmap based on three main areas; first from the industrial and academic point of view to find this 2D material, study the positional of these materials, and find the safe fabrication procedures to create these materials in industrial scale. Develop a new device based on graphene and their technology component. The last area is to combine the graphene structure and the components in devices to provide a new function and application to be used. Moreover, these roadmap is presented many application can be excited using graphene with timelines, such as the electronic devices sensors, flexible electronics, energy conversion and storage, biomedical devices science, health and environment, etc..

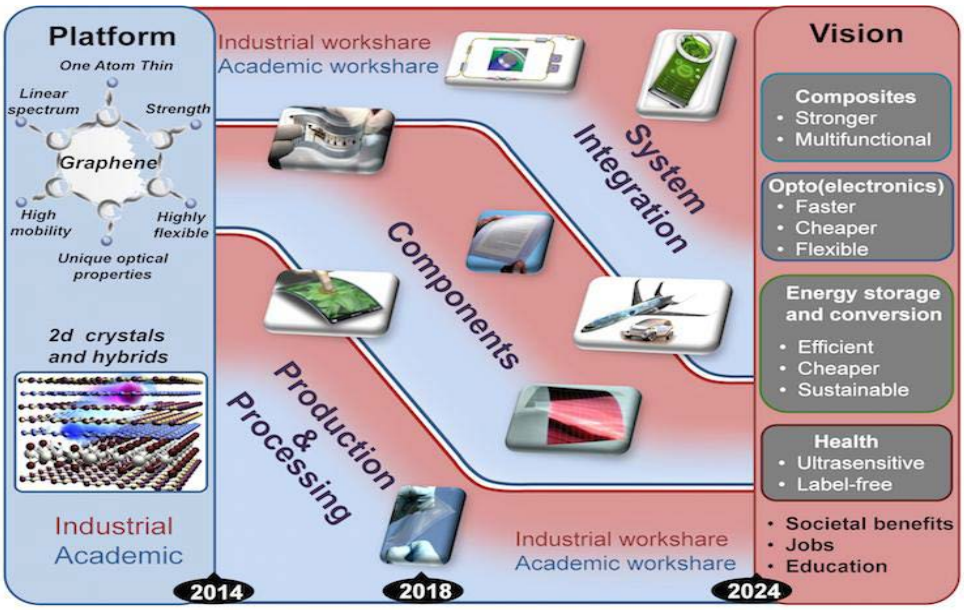

Figure 1.1: Illustration roadmap of graphene application from 2013 to 2024[10].

Generally, the solids materials have imperfections in their lattice and graphene is also similar to these materials has imperfections in its lattice[11].There are several imperfections that could appear in the lattice such as distortions, edge or boundaries defects, point defects, and line defects[12].These defects can be formed as a consequence of the processing or growth of materials, and this could be extended after lithography, etching, deposition. The properties of graphene are affected due to these imperfections, so they will affect the performance of the devices. The affected graphene devices have been experimentally studied and the results indicated degradation in electrical conductivity [13, 14]. However, defects in graphene can be useful for some applications for which there is a challenge to make devices by only using pure graphene. Defects on graphene can provide doping by controlling the carrier

concentration for both of n- and p-types. Depending on the grain boundary defect structures, charge transport properties can be affected as proposed in [15]. Gunlycke D reported[16] that one type of defect which is called line defect can provide the filtering of electrons and holes with specific valley polarisation. The materials properties can be also affected by modified phonon dynamics behaviours by isotopic defects. This kind of defect does not change the electronics properties [17].Therefore, understanding the influence of the defects on properties of graphene and other 2D materials is important to field focuses on in my study.

1.2 Tip-enhanced Raman spectroscopy

With the development of science and technology of the nanostructure and nanomaterials, new microscopic and spectroscopic characterisation techniques to observe and examine in nanoscale have been developed. One of those techniques is transmission electron microscopy (TEM). A popular characterisation method in nanoscience is scanning probe microscopy (SPM), which includes atomic force microscopy (AFM) and scanning tunnelling microscopy (STM) is one of the characterisation methods in nanoscience.SPM can be used to study topography in atomic level, chemical composition, and surface quality. On the other hand, Raman spectroscopy is the technology that is used to investigate the structure of materials – e.g. graphene – including its chemical, structure and the number of the layers with the spatial resolution of microscale. The spatial resolution of Raman characterisation is limited in microscale. In other words, one of the obstacles to characterising materials at the nanoscale is the diffraction limitation of light. To overcome this roadblock, tip-enhanced Raman spectroscopy (TERS) is emerging as a novel technology of SPM that can be successfully used to characterise materials at the nanoscale and to investigate their chemical composition with high spatial resolutions [18-20]. This technology combines Raman spectroscopy with SPM. TERS can detect phonons in materials with a spatial resolution down to less than 20 nm [21], which makes it a very promising tool for nanoscience and nanotechnology. Hung et al.[22]are reported the fabrication process of gold array template for coating AFM tips in order to achieve high quilt tips with spatial resolution down to 10nm. The SEM image with a low magnification of the gold array template is showing in Fig.1.2b, and this figure shows two spots bright and the dark, the gold pyramids are bright spots which show that the gold remains on the array, where the missing gold from pyramids are the dark spots. The high-quality zoom SEM image of gold array template is showing in Fig.1.2c.This project, TERS is used for characterising graphene nanostructures in order to use graphene in future nanoelectronic and nanoelectromechanical (NEM) devices such as transistors,

switches, and physical sensors. Recently, The TERS technology is becoming more attractive for the semiconductor industry.

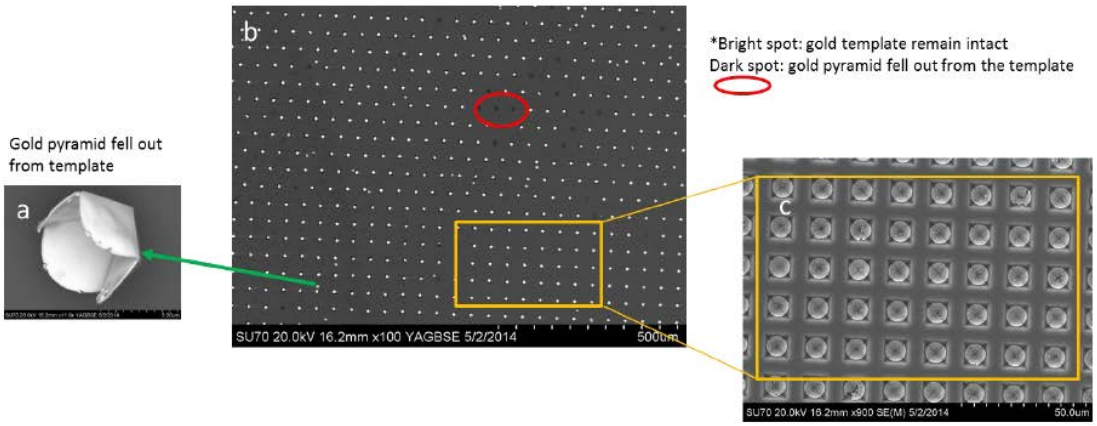

Figure 1.2: Gold pyramids array (a) high-resolution image of gold pyramid using SEM; (b) SEM image with a low magnification of template. Unbroken gold pyramids are present in bright dots in the repeated array, and the dark spots are slots where the gold coating was delaminated and removed during the etching process and (c) SEM image with a high magnification of a finished template reveals the high quality of gold pyramids' array[22].

1.3 Helium ion microscopy

A new kind of surface imaging technique known as Helium-Ion Microscopy (HIM) was presented in 2007 by Carl Zeiss SMT [23-25]. A beam of helium ions is focused on the surface and scanned across with producing the high-resolution image from secondary electron (SE) emission. Thanks to the atomically sharp ion source and bright source combined with the larger momentum and very short de Broglie wavelength of helium ions. In compare with Scanning Electron Microscope (SEM), HIM is able to scan the sample surface to obtain the image of excellent spatial resolution in sub-nanometre scale. In the first ~100 nm of entering the substrate, the He ions produce far fewer collision cascades and so low amount of beam divergence which resulting in very small interaction between the materials and beams and high-resolution images[26-28].

HIM was introduced as imaging technology to scan the surface to acquire ultra-high resolution images. By considering advantage of introducing an intense helium beam with in a focused probe size and that can be sub-nanometre, this technology has the ability for pattering (milling and lithography the surface).As a result, after the discovery of this technology, it becomes as a potential pattering technology for nano-devices fabrication[29-31]. On the other hand, as the ion bombardment introduces defects to graphene, this could be used to introduce defects into graphene. A high level of defects induced to graphene leads

modification of the graphene lattice to amorphous phase [32]. The transition of structure from monocrystalline graphene to amorphous carbon by using gallium ion irradiation on graphene has been reported in [33].In a recent report [34], it was shown that with increasing the dose of helium ions, the transport properties of field effect graphene transistors are changed. The n-type branch started to show insulating behaviour, while the p-type branch shows melting behaviour.

1.4 Thesis overview

The thesis comprises 6 chapters. Chapter 1 presents the general introduction of this work. The relevant literature is critically reviewed in Chapter 2, which is divided into two parts. The first part is about graphene and its general properties. A brief history of graphene, electronic properties, nanodevice applications of graphene, defect engineering on graphene is included. In the second part, Raman spectroscopy for graphene is reviewed. The TERS application to several materials, as well as its application to graphene, are introduced. The general TERS setup and most important components of TERS are also introduced. The TERS experimental setup and optimization of TERS measurements are described in Chapter 3.In Chapter 4, results of micro Raman and TERS studies for suspended graphene structures are described. Detailed investigation of helium-ion-irradiated graphene channels via Raman and TERS is presented in Chapter 5. Chapter 6 is dedicated to Conclusions.

Chapter 1

Chapter 2: **Literature Review**

2.1 General Properties of graphene

2.1.1 Graphene

More than a decade in (2004), Geim and Novoselov at the University of Manchester conducted an investigation into ideal semiconductor materials, and were awarded a Nobel Prize for their experiments regarding two-dimensional graphene. Their study focused on isolating a two-dimensional (2D) monolayer of graphene on SiO_2/Si substrate with a 300 nm SiO_2 layer from graphite bulk using the simple Scotch-tape method. Since its discovery, graphene has been employed by many scientists and engineers because of its unique electronic, mechanical, thermal, and optical properties [35]. After this discovery, research into 2D materials increased rapidly, and is now extensively used in many intersecting fields, as evidenced by more than 60,000 publications on graphene that have since been released[10].

2.1.2 Electrical properties

The electrical properties of graphene are important because of its potential role as a zero-gap semiconductor. The electronic structure of graphene can theoretically be calculated using a tight-binding method [36], which considers two atoms per unit cell. The K space in the BZ of graphene is shown in Fig. 2.1(a) and exhibits high symmetrical points K, K', M, and Γ. Each carbon atom in graphene is connected to three other carbon atoms, with one electron in the three-dimensional (3D) plane free for electronic conduction. Figure 2.1 shows two connected conical points, which are known as Dirac points K and K', with a zero-gap. The schematic structure of graphene device is shown in Figure2.2.The resistivity ρ of a few layers of graphene is showing small change in a temperature range between 100–300 K. The conductivity increases with increasing the temperature 35 to 85 K [37]. The resistance of a few layers of graphene is related to the temperature, and when the temperature increases, the resistance decreases significantly. Furthermore, the number of graphene layers affects the resistivity. When the number of layers increases, the resistivity decreases significantly. The resistivity of graphene was measured by Novoselov et al. [1] on field effect transistors (FETs) on micromechanically cleaved graphene. They found that the resistivity depends on the gate voltage Vg. Figure 2.3(a) shows that the resistivity of graphene has a sharp peak with a value

of several kΩ, and returns to 100 Ω at high values of Vg. Figure 2.2(b) illustrates Vg on both sides of the resistivity peaks along with the conductivity as σ = 1/ρ increases linearly.

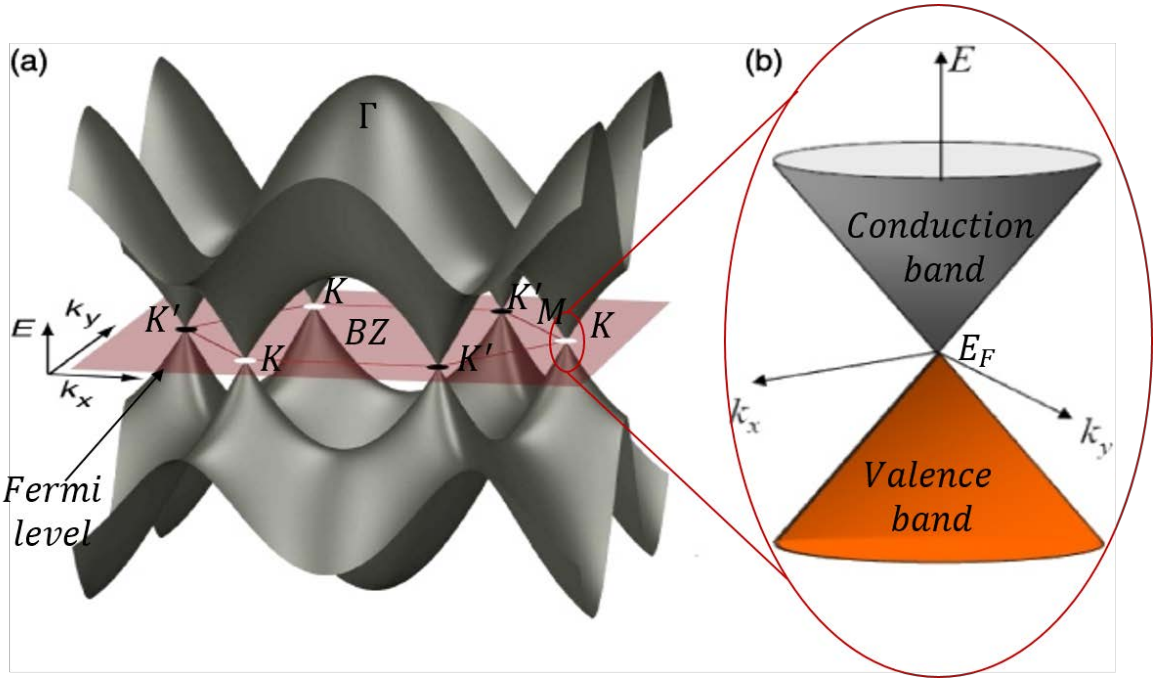

Figure 2.1:(a) Band structure of graphene; (b) low-energy dispersion at one of the K points shows the Dirac cone structure with conduction and valence bands symmetric[38].

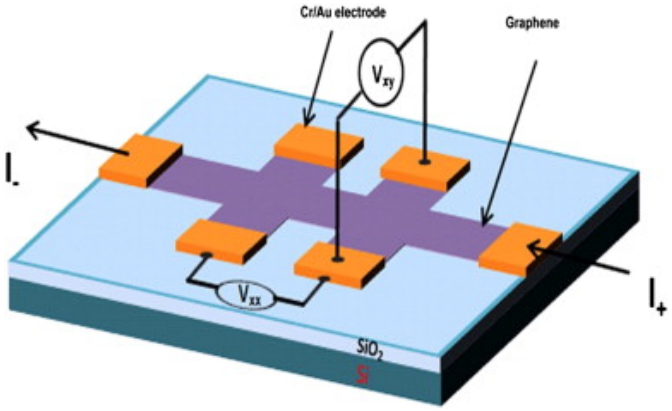

Figure 2.2: Schematic structure of basics graphene device. The arrows are presenting the current path, and the connections between the contact Vxy and Vxx are indicated measuring scheme for the Hall resistance RH [39].

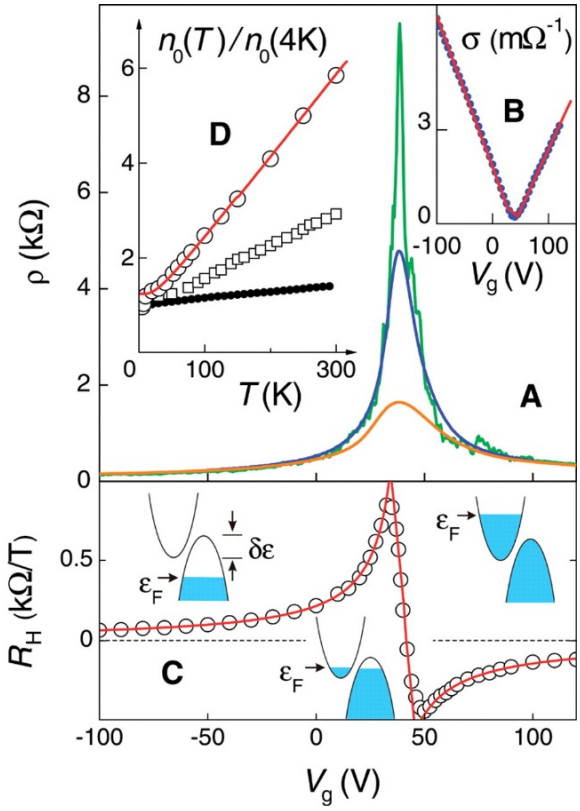

Figure 2.3: Graphene sample field effect: (a) The resistivity (ρ) of graphene sample for three different temperatures (T = 5, 70, and 300 K from the top to bottom curves) with dependence on Vg. (b)The conductivity changes versus V_g example for graphene sample achieved by inverting the curve of 70 K.(c) The R_H hall coefficient versus V_g for the same sample at T=5K [1].

Graphene has a high Young's modulus of E = 1.0 TPa, an intrinsic strength of σ_{int}=130 GPa, and a breaking strength of 42 N/m [5]. These characteristics indicate that graphene is a very strong 2D material. Various standard methods can be used to characterise the intrinsic breaking strength and stiffness of materials, including nanoindentation, microtensile testing, bulge testing, and biaxial strain measurements [40]. Indeed, some of these methods have been used to extract the mechanical properties of a layer of graphene. Figure 2.4(a) presents the results of an atomic force microscopy (AFM) nano-indentation experiment that has been used to measure the force-displacement of suspended exfoliated graphene over a membrane in order to study its mechanical properties (elastic properties and the breaking stress of graphene).

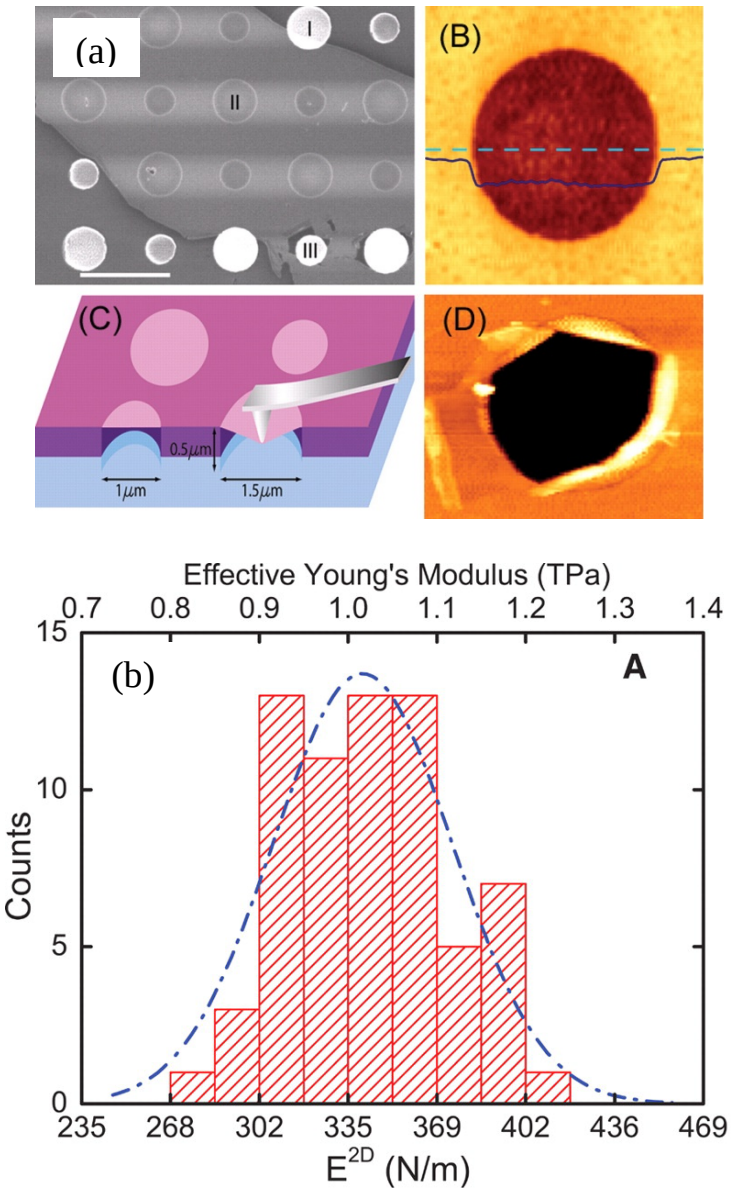

Figure 2.4: (a) Image of suspended graphene using SEM and AFM. (b)Elastic stiffness histogram [5].

The conductivity of graphene can be calculated using $\sigma = en\mu$.Graphene as single carrier concentration of electron or hole is depend on the Fermi level position, and this is describe at high carrier concentrations $n = 10^{12} cm^{-2}$ .The mobility of graphene has been studied at ambient temperature, and it was found that $\mu = 200{,}000\ cm^{-2}v^{-1}s^{-1}$, which is seven times higher than that of Si. The mobility of graphene depends on temperature, which means that when the temperature changes, the mobility also changes. In 2013, Wang et al. [41]performed a theoretical study of the differences in mobility, and found that there were no differences in the mobilities of electrons versus holes, a finding that was confirmed in Ref. [42]. In addition, the conduction of holes in graphene is better than that of electrons, as shown by Lemme et al. in 2007 [43]. The strain effect as a property of graphene was studied

by Wang et al. [41], who found that the amount of strain in graphene affects the charge carriers.

2.1.3 Band Structure

As discussed above, graphene is a 2D honeycomb lattice of carbon atoms, as shown in Fig. 2.5. In order to understand the physical properties of graphene, one must first understand the lattice structure. The lattice of graphene is formed from sp^2 hybridized orbitals, as shown in Fig. 2.5a, in which carbon atoms have four valence electrons in the 2s and 2p orbitals. These orbitals are susceptible to overlapping due to the increased unit energy in the bonds. In single layer graphene, the carbon atoms come together using a mixture of s-orbital 2p-orbital electrons and generate three strong δ bonds between the carbon-carbon atoms using covalent bonds.

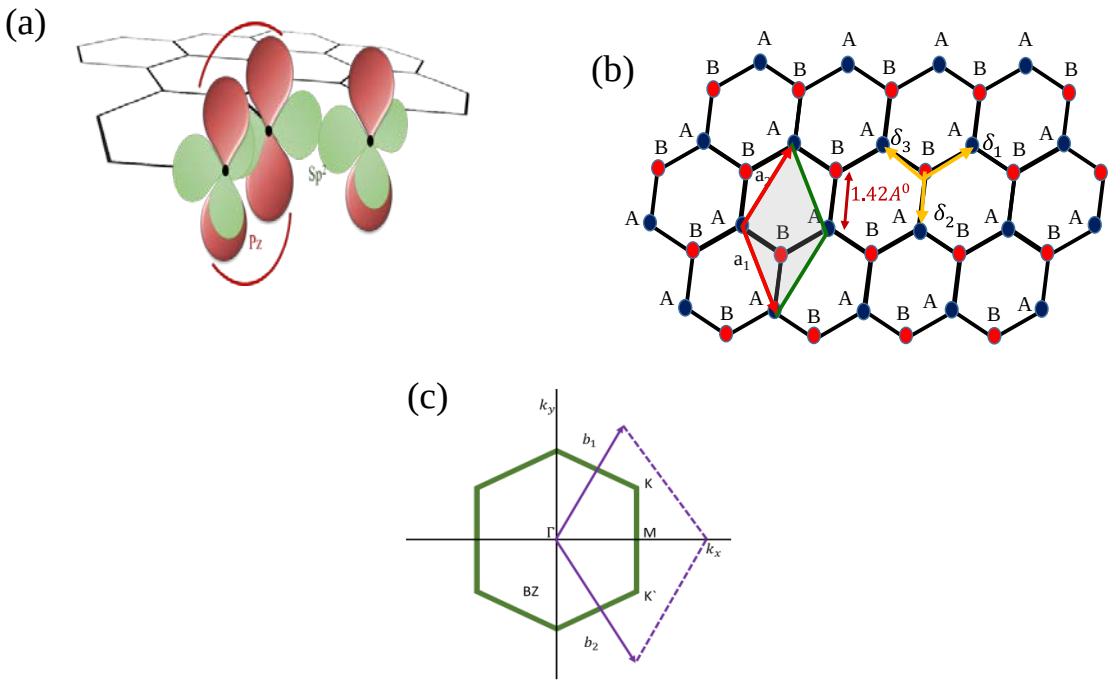

Figure 2.5.: Illustration of the lattice structure of graphene: (a) sp^2 hybridized carbon atoms in the graphene lattice; (b) the graphene lattice with sub-lattices A and B, where the distance between the C-C atoms is a ≈1.42° A; and (c) the Brillouin zone.

As shown in Fig. 2.5b, every unit cell is triangular with two atoms forming the two sub-lattices A and B of graphene. This can be described as:

$$a1 = a/2(3, \sqrt{3}), \tag{2.1}$$

$$a2 = a/2(3, -\sqrt{3}), \tag{2.2}$$

Where the distance between the two C-C atoms is about a ≈ 1.42Å. Moreover, b1 and b2 are reciprocal lattice vectors that can be written as:

$$b1 = 2\pi/3a\ (1, \sqrt{3}), \tag{2.3}$$

$$b2 = 2\pi/3a\ (1, -\sqrt{3}). \tag{2.4}$$

Figure 2.5c illustrates the hexagonal honeycomb lattice of graphene, which is known as a Brillouin zone (BZ). Therefore, the two points at the corners of the graphene lattice K and K' should be taken into consideration. These two points are known as the Dirac points, and their positions in the momentum space are given as:

$$K = (2\pi/3a, 2\pi/3\sqrt{3}a), \tag{2.5}$$

$$K' = (2\pi/3a, -2\pi/3\sqrt{3}a). \tag{2.6}$$

According to Fig. 2.5b, the three nearest-neighbour vectors in real space are:

$$\delta 1 = a/2(1,\sqrt{3}), \tag{2.7}$$

$$\delta 2 = a/2(1,-\sqrt{3}), \tag{2.8}$$

$$\delta 3 = -(1,0). \tag{2.9}$$

2.1.4 Graphene Phonon Dispersion

To study graphene using Raman spectroscopy, the phonon dispersion of graphene should first be understood. The single-layer graphene phonon dispersion bands are shown in Fig. 2.6a. Moreover, as discussed in Section 2.1.3, single-layer graphene has two carbon atoms A and B in the unit cell, and this has six phonon dispersion modes $(\Gamma = A_{2u} + B_{2g} + E_{1u} + E_{2g})$,three acoustic (A) branches, and three optical (o) branches in the ΓM and ΓK directions. The mode E_{2g} is the degenerate in-plane optical mode, and B_{2g} is the out-of-plane optical mode. The three acoustic branches are the transverse acoustic (TA), longitudinal acoustic (LA), and out-of-plane transverse acoustic (oTA) branches. The three optical branches are the longitudinal optic (LO), in-plan transverse (iTO), and out-of-plane transverse optic (oTO) branches. The vibration on sub-lattice A is against sub-lattice B, as shown in Fig. 2.6a.The G peak is correspond of in-plane optical modes iTO and LO degenerate of E_{2g} phonon in the Γ points. The symmetries of iTO and LO along the ΓK line are T3 and T1, respectively, and Σ_3 and Σ_1, respectively, along ΓM. The phonon around the K point is considered to be

the most important, especially for the D and 2D bands, which are related to this phonon. The phonon iTO is non-degenerate in the K point, and this is known as $A_1^{'}$ with E` being doubly degenerate in the K point where E1u (LO and LA) meet each other. In order to understand the phonon LO and TO in the Γ and K points, the Kohn anomaly effect should be considered because it is responsible for the softening of the Γ and K points.

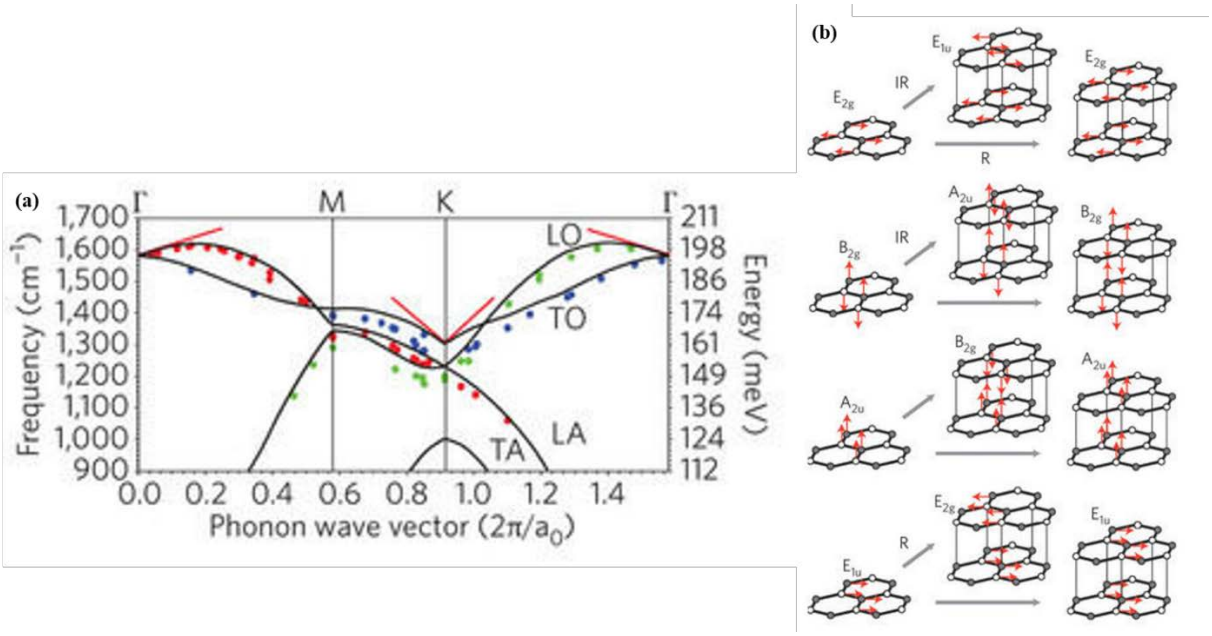

Figure 2.6: a) Phonon dispersion of graphene. The black curves LO, iTO, oTO, LA, TA, and oTA are related to Raman scattering, whereas the red lines correspond to Kohn anomalies. b) The phonon dispersion around the Γ points. The red arrows are atom displacements, and each phonon rise in the graphene is shown by the grey arrows, while those in the graphite phonons rise to two modes These are the Raman active (R), infrared active (IR), and inactive (un-labelled) modes [44].

2.1.5 Defects in graphene

Graphene as a 2D material has attracted the attention of engineers and scientists because the properties of graphene make them ideal candidates for the realisation and advancement of many different technologies. However, the defect structures that appear on the graphene lattice during the fabrication process can significantly affect the performance of graphene devices. Therefore, in this subsection we summarize the important defect structural types that are present in graphene lattices. Graphene has the ability to restructure and arrange its lattice around defects [45].

According to the arrangement convention of bulk materials, defects or external atoms are describe as intrinsic (e.g. dopants and impurities) and extrinsic. The types of defects in terms of their dimensions are: zero-dimension (0D), which refers to point defects (e.g. vacancies

or interstitial atoms); one-dimensional (1D), which refers to line defects; 2D refers to the grain boundaries; and3D defects, although these do not appear in graphene due to the 2D structure.

Point Defects

This defect is the first type of defects in graphene, and includes Stone-Wales defects, single/multiple vacancies, and adatoms. Theoretically, the defects stability quantity in graphene can be calculated using the following equation[46]:-

$$E_{from} = E_d - (E_{bulk} + N\varphi_c) \tag{2.10}$$

where E_d is the total energy of the defects in graphene,E_{bulk} is the total energy of perfect graphite bulk, φ_c is the chemical potential of carbons atoms, and $\pm N$ is the number of carbon atoms [46]. From this equation, the stability of defects in graphene depends on E_{from}, and lower values indicate greater stability.

Stone-Wales defects

As shown in Fig. 2.7 (b), the Stone-Wales (SW) defect is one C-C bond rotated at 90^o, which results in four hexagons being transformed into two heptagons and two pentagons(SW(55-77)) [47, 48],and this type of defects does not include any added or removed atoms. In Figure 2.7(b), the energy barrier of the SW defects is ~5 eV, and a ~10 eV of kinetic energy barrier is required for this change, and with this a high kinetic energy barrier SW defects is produced in graphene at room temperature. At lower energies, ion irradiation is able to introduce this defect on graphene, and thereby displace C atoms.

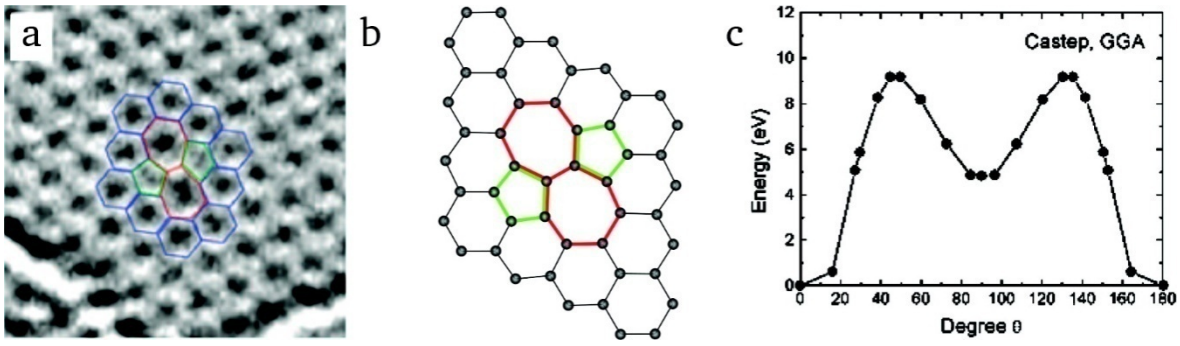

Figure 2.7: a) TEM image of defect carbon-carbon lattices. b) Atomic structure of a Stone−Wales defect. (c) Energy barrier for bond rotation C-C.

Single vacancy defects

Vacancies are generated in graphene when the C atoms leave the lattice due to energy perturbations higher than the displacement threshold (T_d). Approximately 7.5 eV energy is required to produce a single vacancy (SV). When C atoms are removed from the lattice, three dangling bonds are created [49].

Double vacancy defects

Double vacancies (DVs) are more complex because this removes a defective region from a five-atom and nine-atom arrangement and connects it with two dangling bonds to create many shapes [45]. Replacing two C atoms is the simplest way to create a DV from two-pentagon and two-heptagon structures (5-8-5), as presented in Fig. 2.8(b). Whereas, the effects of vacancies are able to move in the graphene lattice. The DVs cannot move a lot because is require high movement energy ~7.5 eV in compare with the SVs which is required ~1.3 eV. These defect are generated by removing single atoms. To produce these vacancies, the lattice is bombarded by ions where the possibility of removing large number of atoms is high. In order to produce this non-hexagonal structures in graphene, the graphene sheet must be folded and use a high energy to formed the structures.

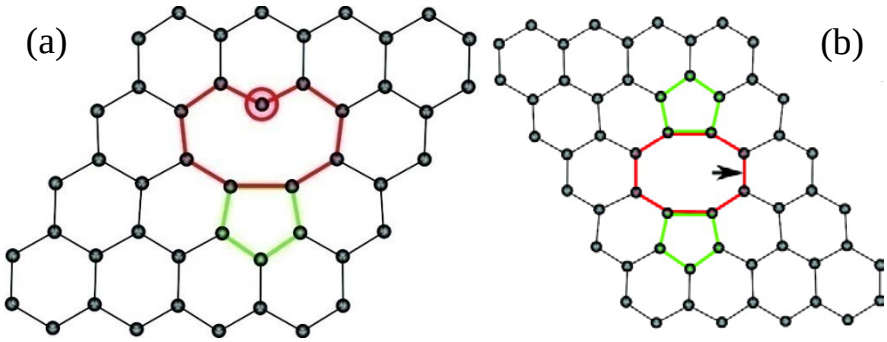

Figure 2.8: a) Single vacancy defects (SV). b)Double vacancy (DV) [50].

Adatom defects

These types of defects also can be occur in graphene[51]. Injected atoms can be used to form covalent bonds with graphene atoms to change from sp^2 to become sp3 hybridization. This occurs when the C atoms come closer to the surface of the graphene. Figures 2.9 (a) and (d) show the adatom position on top of the bonded C-C atoms, and ~2 eV energy is required for binding. This adatom can easily travel with small energy ~0.4 eV around the graphene surface. Any atom removed from the graphene is considered to be an adatom, and it becomes an adatom on the graphene surface. Figures 2.10show examples of these defects, which are the Inverse Stone-Wales defect. The adatom defect not only happens using C atoms, it can

also be used for any external atoms depending on the bonding strength. The adsorption can be either physisorption (weak, van der Waals bond) or chemisorption (strong, covalent bond). With an activation energy of ~0.28 eV, the weak bonding was found between the graphene and the transition metal because it can easily move along the graphene surface. As shown in Fig. 2.10, the adsorption of the graphene surface increases because of the metal atoms are attracted to it due to the strain near the defect. This is a substitutional defect on the graphene with respect to the carbon atom.

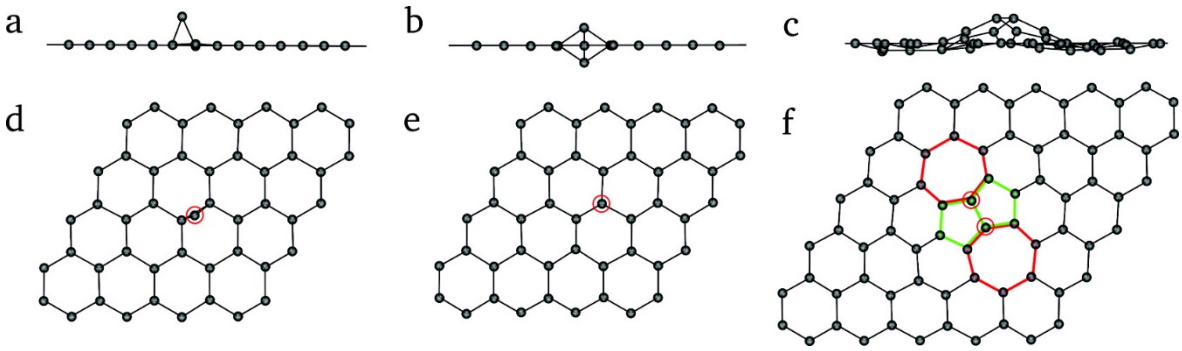

Figure 2.9: Carbon adatoms;(a, d) single adatom on top of C-C atoms; (b, e) the dumbbell configuration; (c, f) the Inverse SW defect [50].

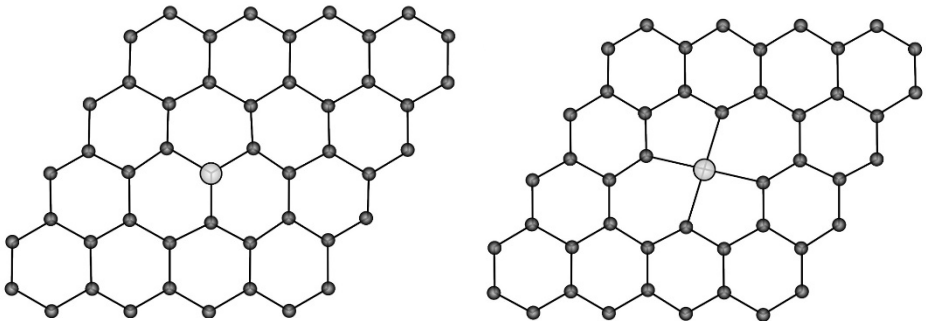

Figure 2.10: metal adatom bonding in graphene[50].

Line Defects

This type of defect is 1D, and is also known as extended lines defects. These types of defects can be created in CVD graphene grown in metal, and appear as grain boundaries with mismatched lattices. In grown graphene, the electronic properties can be dictated by the atomic structural boundaries and grain sizes. Figure 2.11 shows an example of a grain boundary of graphene grown on an Ni surface [52]. The boundary is formed by periodic alternations of pentagon pairs and octagons due to the mismatch between the two graphene areas.

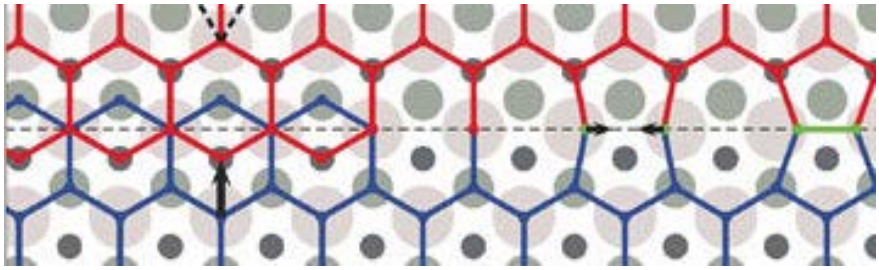

Figure 2.11: Line defect formed between two graphene areas grown on Ni [52].

2.2 Device fabrication

There are various approaches to the fabrication of graphene. The fabrication procedures include the mechanical exfoliation (ME) from bulk graphite, epitaxial growth graphene on an insulator (SiC) and chemical vapor deposition (CVD) over a metal surface (either Nickel (Ni) or Copper (Cu) [53]. In the section below, these fabrication methods are briefly described. More fabrication methods of graphene are described in Refs [54-56]. Although the ME fabrication method is simple, it cannot be used to produce a thin graphene layer. Instead, the chemical growth method is the most promising method for the production of thin graphene layers.

2.2.1.1 Chemical Vapor Deposition (CVD)

The CVD method [57-59] is used to deposit graphene on metal substrates such as Copper (Cu) [59, 60] and Nickel (Ni) [61-63] , among others. Cu is better suited to this technique in comparison to Ni because a single graphene layer can be grown on Cu with the help of CVD. However, multilayers are usually grown over Ni. Besides this factor, Cu is the most extensively used metal substrate owing to its low cost, zero carbon solubility, and its ability to generate graphene layers of high quality over a greater area [64]. In the CVD technique, Cu must be heated at a temperature up to 1000 ºC, which can be maintained in a furnace before the graphene is deposited on the top of Cu, as shown in Fig. 2.12. The domain size of the metal is enhanced as a result of the heating. In the furnace, Hydrogen (H_2) and methane (CH_4) are flushed over the substrate. CH_4 sets down on the surface of the substrate via chemical adsorption when it is blown over. At this stage, CH_4 reacts with the surface and is catalyzed by H_2, as shown in Fig. 2.13. The temperature of the furnace is then quickly lowered so that the accumulated carbon layer aggregates into bulk graphite. Upon crystallisation, this aggregate turns into an adjoining layer of graphene over the metal surface. Since a number of different materials are used for the execution of the CVD technique, the formation of the graphene layer is subjected to the addition of impurities. However, in this

technique, one can reduce the concentration of impurities. This results in the formation of wrinkled graphene layers because of the difference in thermal expansion between Cu and graphene. Annealing can be used to manage this problem; however, further studies should be carried out in order to isolate more efficient solutions. Unlike the Scotch-tape method, which results in the formation of micron-sized flakes, the CVD technique yields a contiguous layer of graphene over the metal surface. For this reason, graphene layers can be employed in solar cells.

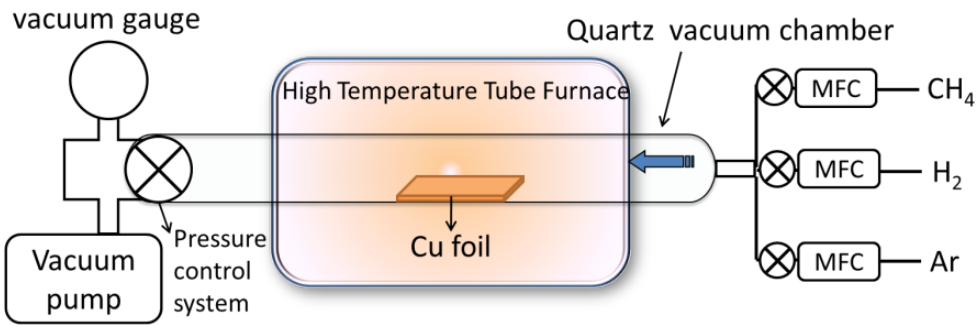

Figure 2.12: Illustration of CVD of graphene setup by using a Cu or Ni catalyst. The setup has a tube furnace for high-temperature heating, a quartz vacuum chamber for adjusting the growth conditions using vacuum and pressure control, and carbon and gases, which are used to provide mass flow controllers (MFC). Adopted from [64].

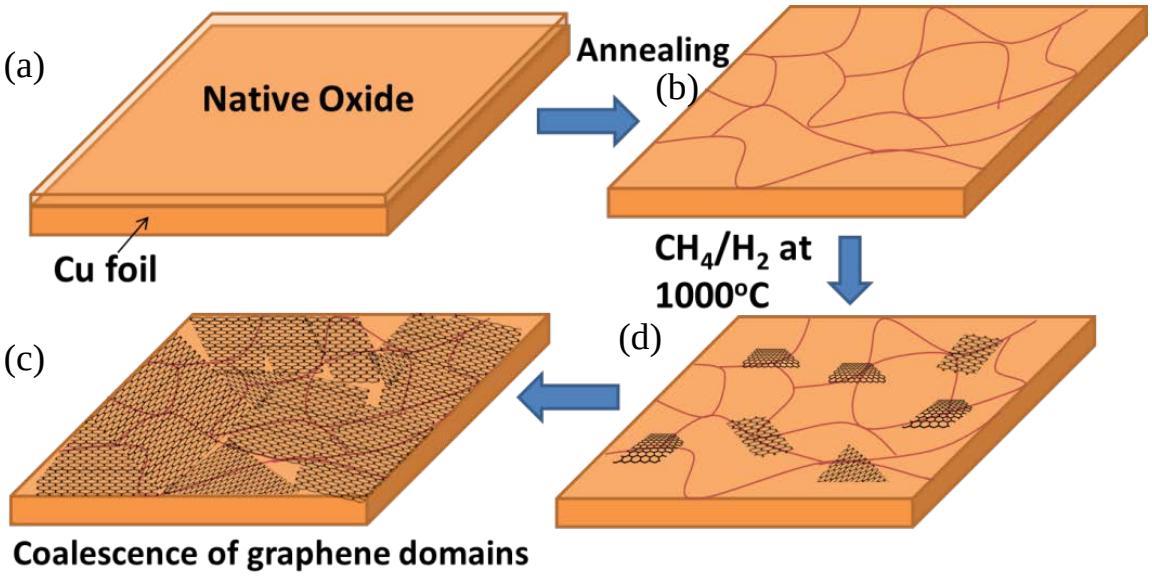

Figure 2.13: Graphene growth on a Cu substrate using the CVD method: (a) native oxide on Cu foil; (b) after the surface annealing at high temperature in a hydrogen environment; (c) production of graphene after exposing the Cu foil to CH_4/H_2 at 1000 °C; and (d) the graphene layers. Adopted from [64].

Graphene can be deposited onto a number of different metal substrates, as mentioned earlier. Besides Cu, graphene can be grown on Ni as well. Yet, prior to deposition of the graphene layer, Ni must be layered onto silicon. Moreover, Ni can only be used in the form of thin

films. This is because different metals have varying potentials for absorbing carbon. Ni tends to generate graphite owing to its greater capacity to absorb carbon as compared to Cu. It is important that Cu substrates with deposited graphene must not be taken out of the reactor at room temperature because Cu is highly susceptible to oxidation as compared with Ni [65].Moreover, carbon is adsorbed only at the surface of the substrate instead of being absorbed into the bulk of the substrate as the weak bonds that bind carbon atoms with the Cu can only develop with open sites of bonding at the lattice surface. Hence, it can be stated that the utilisation of Cu foils for the deposition of graphene not only simplifies the technique but also makes it more efficient.

Transfer Method of CVD

A beneficial aspect of utilizing CVD is that graphene layers grown over the surface of a metal can be transferred to several types of substrates. Measurement of optoelectronic characteristics requires transferring the graphene layer to the surface of the substrate once it has been grown over a metal [64]. After taking out the Cu foil with graphene over its surface from the furnace and allowing it to cool down, graphene is coated with polymethyl methacrylate (PMMA) or polymeric polydimethylsiloxane (PDMS) as a support. The next step involves the removal of Cu using the etchant ferric chloride ($FeCl_3$). The graphene left behind on the surface of the polymer can then be transferred to any substrate, as shown in Fig. 2.14. A solvent is then employed for dissolving the polymer. Silicon dioxide serves as the most extensively used substrate, and allows for the examination of graphene through optical microscopy. The conductive characteristics, electrical efficiency, uniformity, and purity of graphene can be measured when silicon dioxide is used as a substrate.

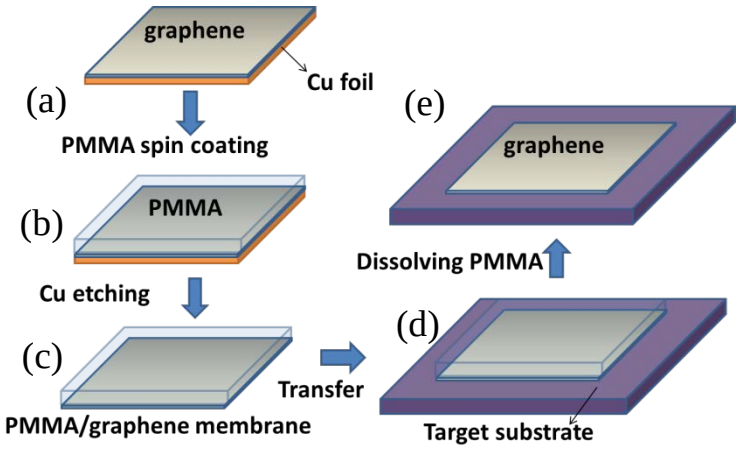

Figure 2.14: Illustration of general transfer process of CVD-fabricated graphene from the top of copper foil to the substrate. (a) Graphene layers on the top of Cu foil. (b) A thin polymeric layer (polymethylmethacrylate PMMA) spin-coated on top of the graphene layers. (c) The etching of Cu using FeCl3. (d) The PMMA dissolved using acetone or chloroform. (e) Graphene layers on the top of substrate. Adopted from Ref [64].

2.2.2 Graphene nano-devices application

Graphene is considered to be an ideal material for various electrical and mechanical applications because of its notable properties, such as a zero band gap, high mobility, breakdown current density, high saturation velocity, ultra-high stiffness, and low mass. In this section, we discuss some graphene nano-devices.

2.2.2.1 Electronic devices application

The high mobility, large critical current density, and high saturation velocity of graphene make it an interesting material for radio-frequency graphene transistor applications with the high-frequency operation. Liao et al. developed a self-aligned graphene transistor with nanowire gates and had a high cut-off frequency (up to 300 GHz) [66]. A physical dry transfer process was used to align the top gate of the CO_2Si-Al_2O_3 core-shell nanowire on top of the graphene, as shown in Fig. 2.15. Improving the speed of transistors requires high-quality graphene without defects, a dielectric integration strategy, and a self-aligned device layout. This is considered to be a promising for improving the transistor speed. In 2012, Cheng et al. reported a high-performance graphene transistor with a cut-off frequency up to 427 GHz by using lithographically patterned gate stacks on top of graphene as the self-aligned top gate, as shown in Fig. 2.16[67].

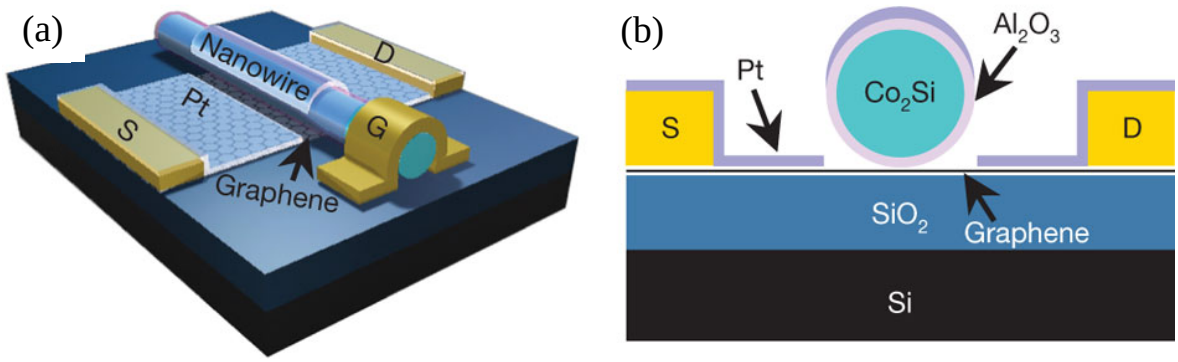

Figure 2.15: (a) Schematic of graphene transistors with a self-aligned nanowire gate device layout, source, and drain, gate, and Co2Si–Al2O3 core–shell nanowire top gate. (b) Cross section view of the self-aligned graphene transistor device [66].

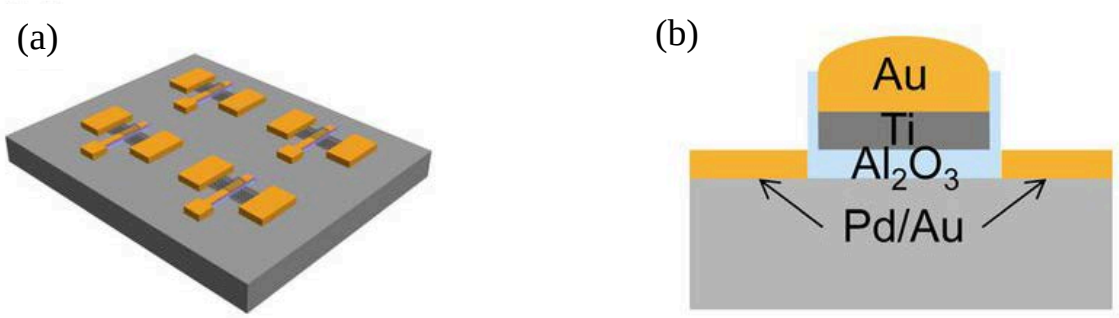

Figure 2.16: (a) Schematic of graphene transistors with a self-aligned transferred gate stack device layout, external source, drain, and top gate. (b) Cross section view of a graphene transistor device [67].

2.2.2.2 Graphene for NEMS application

The ultra-high stiffness and low mass of graphene makes it an ideal material for applications in nanoelectromechanical systems (NEMS). Chen et al. reported a single layer graphene NEMS resonator device, as shown in Fig.2.17, and achieved resonances in the megahertz range. The device design applied a gate voltage to a membrane model to determine the mass density and built-in strain of the graphene[68].

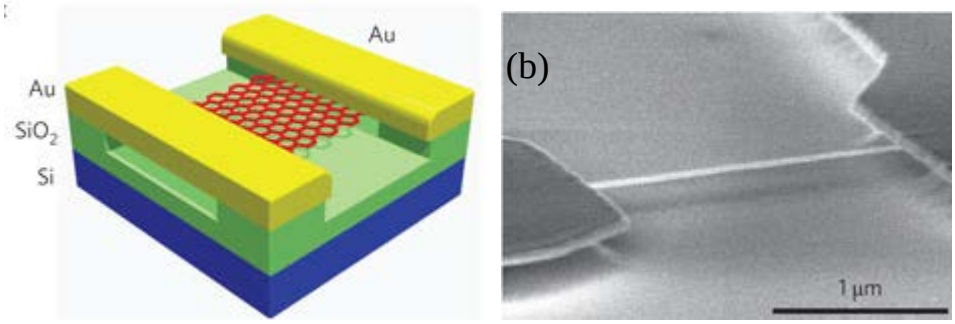

Figure 2.17: (a) Diagram of a suspended graphene nanoribbon, and (b) SEM image of suspended graphene [68].

Milaninia et al.[69] groups are reported the fabrication of graphene NEMS switch by depositing two layers of graphene with a 500 nm gap to separate the layers. A 3-μm wide strip of graphene was suspended over a 20 μm wide etched trench, and ~5 V was applied between the top and bottom layers to deflect and contact the bottom layer. Figure 2.18 shows a schematic of a graphene NEMS switch along with SEM images of a device fabricated by chemical vapor deposition (CVD). The fabricated switch failed after 4th cycles.

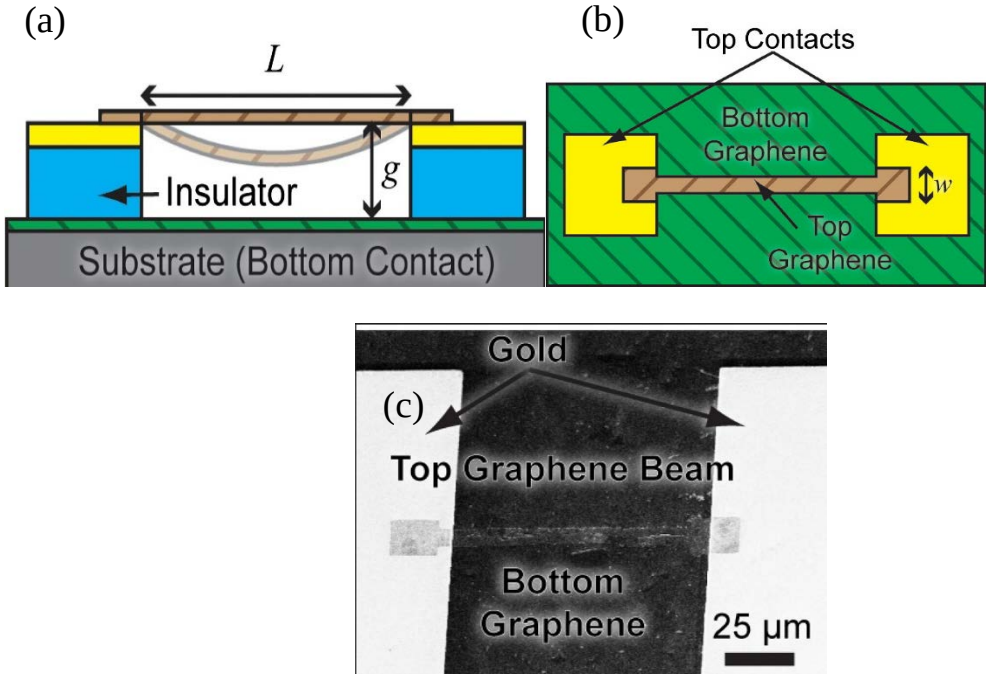

Figure 2.18: Diagram of CVD graphene NEMS switches: (a) cross section of a CVD graphene switch, (b) top view, and (c) SEM images of a suspended CVD graphene switch [69].

The suspended CVD graphene beam electro-mechanical switches fabricating method was developed by Kim et al. [70].Figure 2.19 shows a diagram and SEM image of the fabrication steps of a suspended CVD graphene Switch. The rectangular region of SiO_2 is etched with height air-gap of 0.15µm over a smaller 20µm wide trench to generate suspended graphene beam, and the device operated with a supply voltage of 1.85 V. The on/off characteristics of the graphene switch device and its response have been reported.

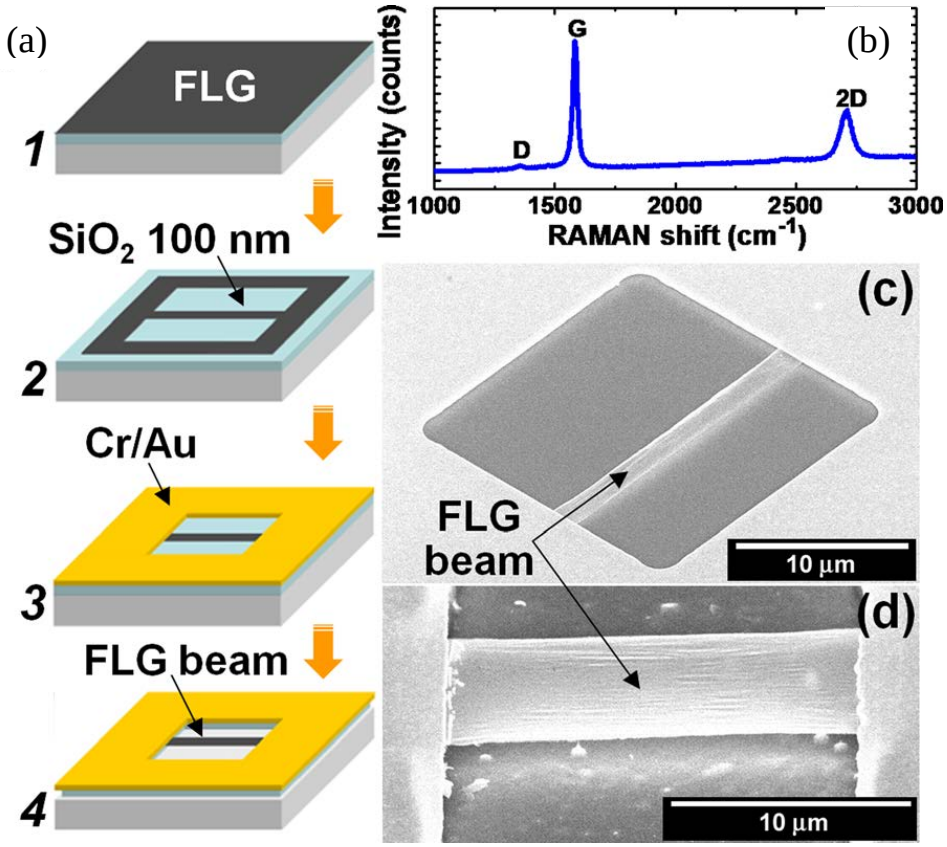

Figure 2.19: Diagram of the fabrication process of a suspended CVD graphene switch: (a) #1 shows thermal release tape used to transfer a single layer of graphene onto a 100-nm-SiO2/Si substrate, #2 is the photolithography and O2 plasma step for defining the graphene layer, #3 shows the lift-off and Cr/Au deposition for the electrode, #4 etching the SiO2 using HF, and the Si using potassium hydroxide(KOH) for making suspended graphene, (b) Raman spectroscopy of CVD graphene, (c) and (d) SEM images of the device [70].

2.2.3 Defect engineering on graphene

The formation of defects in graphene has been extensively investigated using transmission electron microscopy (TEM). For example, the transformation of point defects in graphene was studied using TEM by Kotakoski et al. [71], where the TEM showed complex amorphous structures with a rotated hexagon domain surrounded by other polygons, which were grown and rearranged from vacancies.

Various acceleration voltages have been used in different studies. For example, a 300 keV acceleration voltage was used to irradiate the suspended graphene, which damaged the graphene atoms from the lattices. An 80 keV voltage was used to image the sample without causing additional damage to the graphene lattice, but to allow for some bond rotation. To observe defect structures in graphene, 100 keV with dose $10^{24}cm^{-2}$ has been used for full re-bonding. Although many polygons defects and a few holes are formed in the graphene after this irradiation the authors state that graphene remains a coherent membrane. A voltage of 80 keV was used to displace the carbon atoms in the graphene lattice[72].

The single vacancies created on graphene using 300 keV occurred due to the knock-out uncoordinated of atoms from the lattice, as shown in Figures 2.20 (b-d). This irradiation energy was enough to form single and double vacancies [50]. Irradiation of 80 keV was not enough to sputtered any more atoms from the graphene lattice after 300 keV irradiation , but this level of irradiation did only change the arrangement of atom in lattice, i.e., 5-8-5, 555-777, 5555-6-7777, etc. [50], due to the energy perturbation (barrier ~5 eV). The bonds changed from one rotation to another, as shown in Figures 2.20(c-f). Bond rotations and reorientations occurred at 80 keV, even though this is lower the than threshold T_d, as shown in Figures 2.20(a, e, f).The defect in graphene lattice is positioned randomly along the zigzag line.

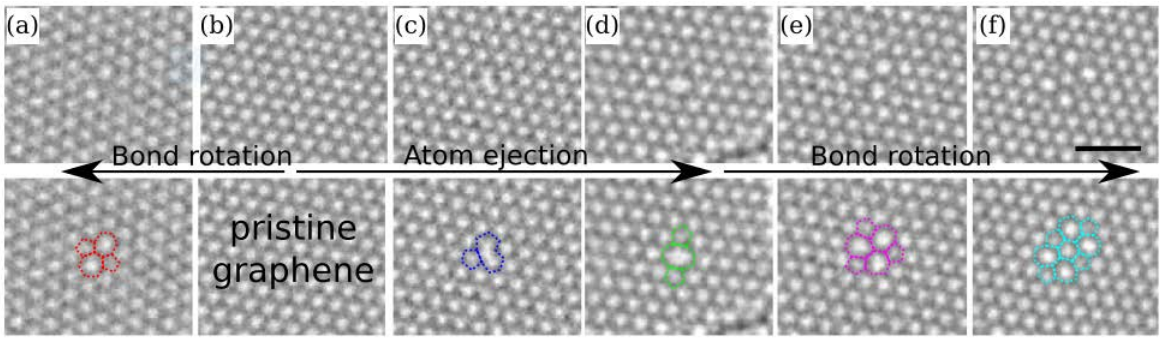

Figure 2.20: TEM imaging of graphene defects: (a) At a low beam energy, bond rotations occur to form Stone-Wales (SW) vacancies, (b) pristine graphene form, (c) atoms are expelled in single vacancies at high beam energies, (d) double vacancy, and (e,f) For more stable configurations, bond rotation drives the initial double vacancy (scalebar = 1 nm)[71].

This study shows under energetic particle irradiation graphene defects develop, and revealed a generally stable configuration of multi-vacancies, that is, rotated polygons bounded by polygons.

The nature of defects on graphene nanowires device induced by helium ion irradiation as shown in Figure 2.21, and the effects on the electrical transport properties and Fermi level was studied by Moktadir et al.[32] in 2015 using Raman Spectroscopy and X-ray

photoemission spectroscopy (XPS). The I_d-V_d of the pristine and irradiated graphene channels exhibited linear characteristics with the absence of a transport gap, as shown in Fig. 2.22(a). Figure 2.22(b) shows the dI_d/dV_d conductance for the highest defect concentration. Point defects were introduced into graphene, and as the defect concentration increased, the resistivity increased and the conductivity decreased. Moreover, the results of Raman spectroscopy shows the increase of D peak at (~1350 cm^{-1}), which is consistent with the increase in defect concentration; however, the D peak, which indicates disorders or defects in the unexposed graphene, is absent in Fig. 2.23.

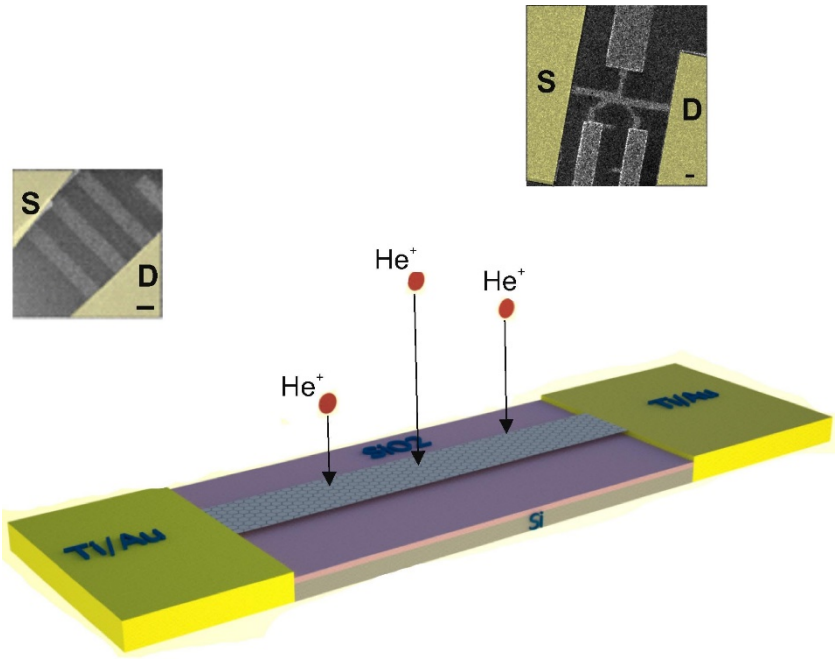

Figure 2.21: Illustration of graphene nanowires device channel, source, and drain contacts. Graphene channel irradiated with HIM.

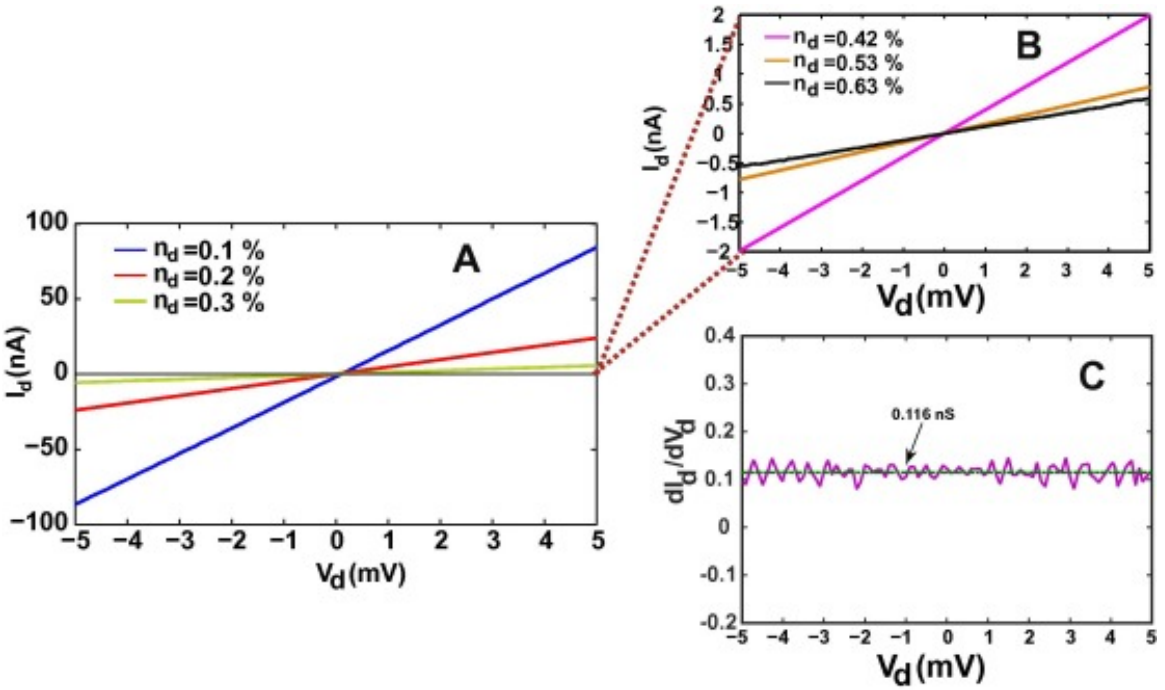

Figure 2.22: (a) I_d-V_d of the irradiated graphene channel with various values of defect concentration. (b) I_d-V_d at Id= 0. (c) dI_d/dV_d conductance for the highest defect concentration [32].

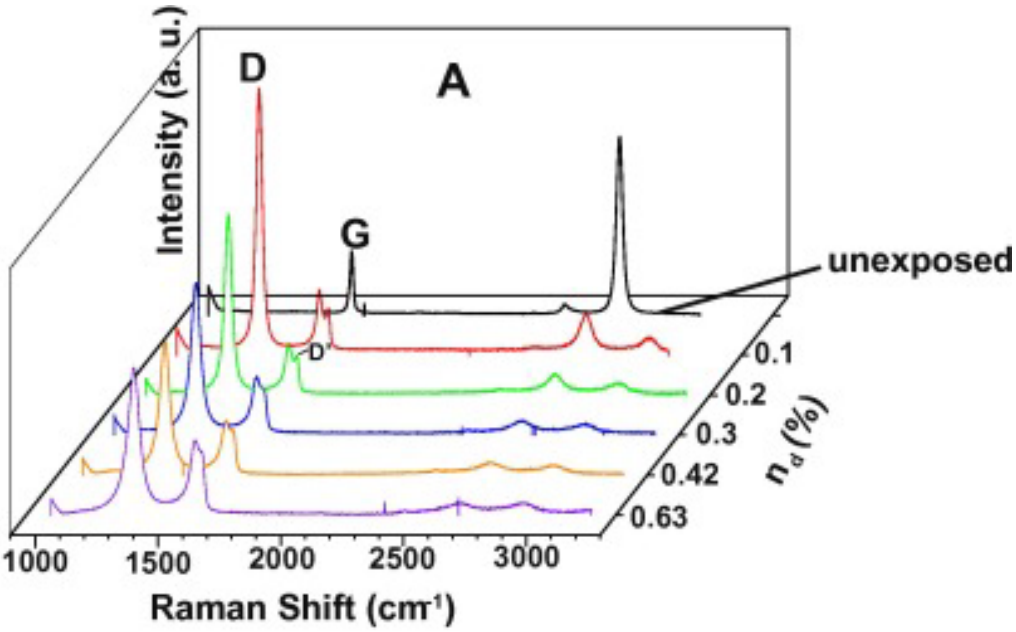

Figure 2.23: D and D' peaks of the Raman spectrum for various defect concentrations, which increase with increasing concentration [32].

For further understanding and quantitate the nature of the defects, the intensities of the $I_{(D)}$ /$I_{(D')}$ fitting data from several published reports are shown in Fig. 2.24. Therefore, the maximum intensities of the defects were observed for sp^3 $I_{(D)}$ /$I_{(D')}$ (~13), while for the vacancy defects decreased to ~7, and the minimum defects were the boundary at ~3.5 in graphite [73]. XPS can also be used to quantify the defects in graphene as shown in Fig.2.25.

This was used on an irradiated graphene sample to determine if any atomic defects are present near the carbon. XPS spectrum is only present the O_2, and Si scattered from the SiO_2 substrate, and no other elements were observed in the graphene

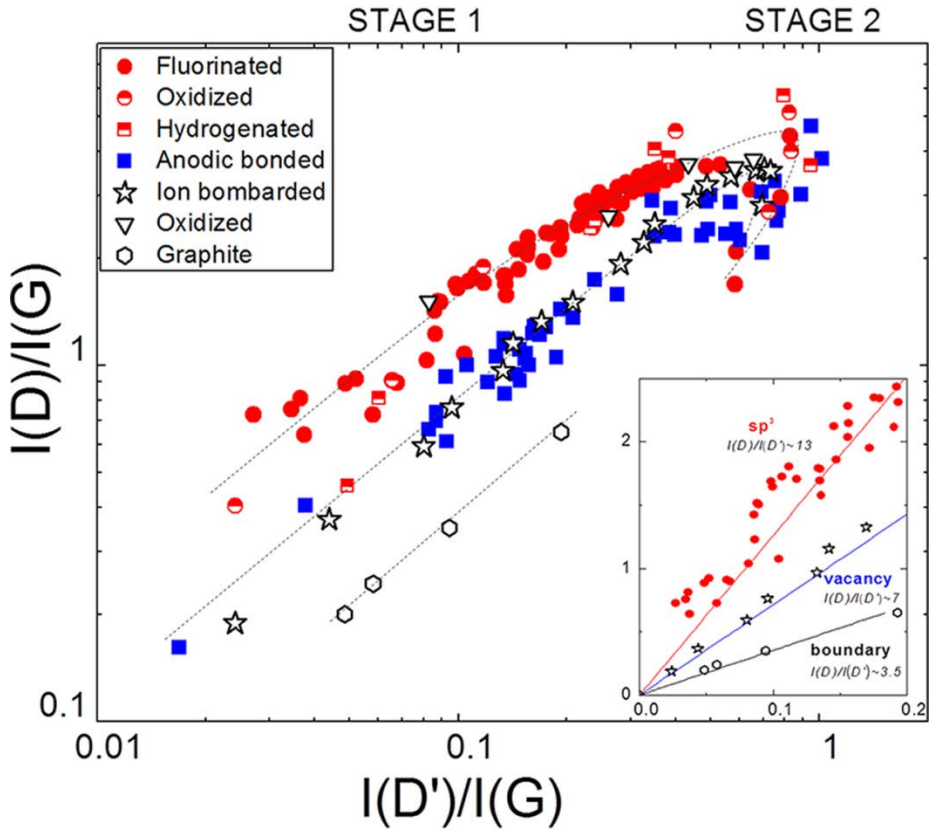

Figure 2.24: I (D) /I (G) versus ratio I (D') /I (G) of different data collected from the literature [74].

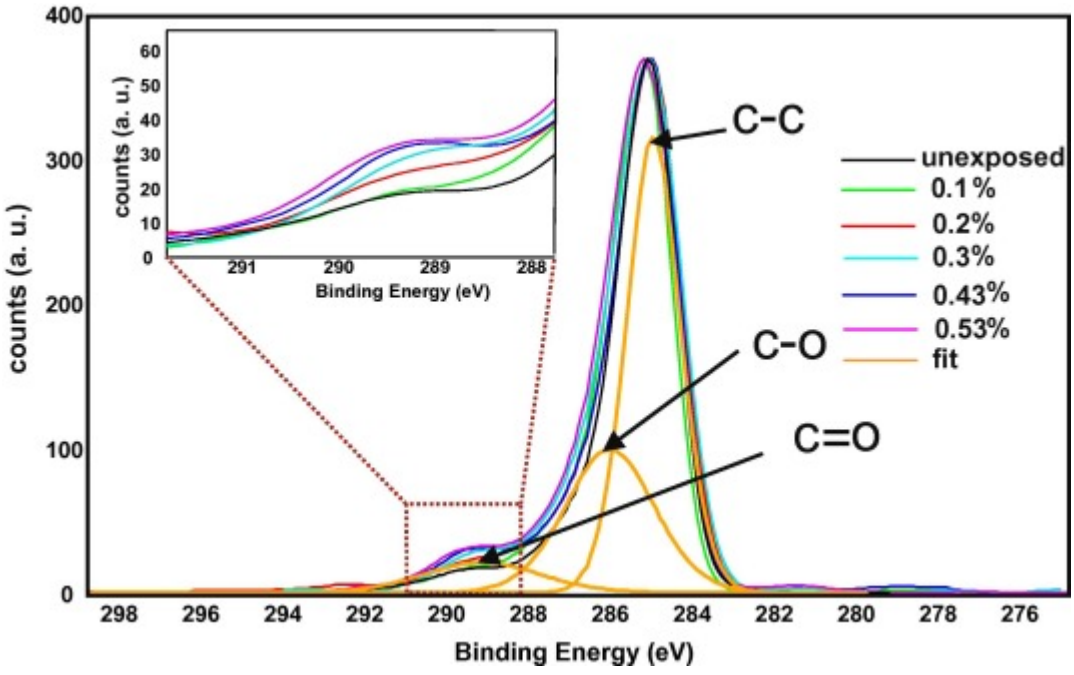

Figure 2.25:XPS spectrum for C1s level for various defect concentrations [32].

2.3 Nano imaging for graphene

To gain an understanding of the properties of graphene nanodevices along with an image of its structure, several nanoscale microscope imaging technologies can be used, such as electron microscopy (EM), scanning probe microscopy (SPM), which includes AFM, scanning tunnelling microscopy (STM), as well as spectroscopy, which includes Raman spectroscopy ,XPS, and TEM.

2.3.1 Raman Spectroscopy for graphene

The use of Raman spectroscopy to investigate graphene defects [75], strain, and graphene edges [76-78] has been covered extensively in the literature. The positions of the 2D and G peaks shift up to −27.8 and −14.2 cm^{-1}, respectively, per 1% of strain as determined by Raman measurements of graphene under strain [77]. The position of the G peak can be affected by both strain and doping. Figure 2.26 shows that the G peak can be split into two peaks under uniaxial strain, and split peaks correspond to two orthogonal modes ($E_{2g}^{\pm}$) parallel or perpendicular to the strain, and that the 2D peak shifts when significant levels of strain are applied on top of the flexible substrate [77, 78].

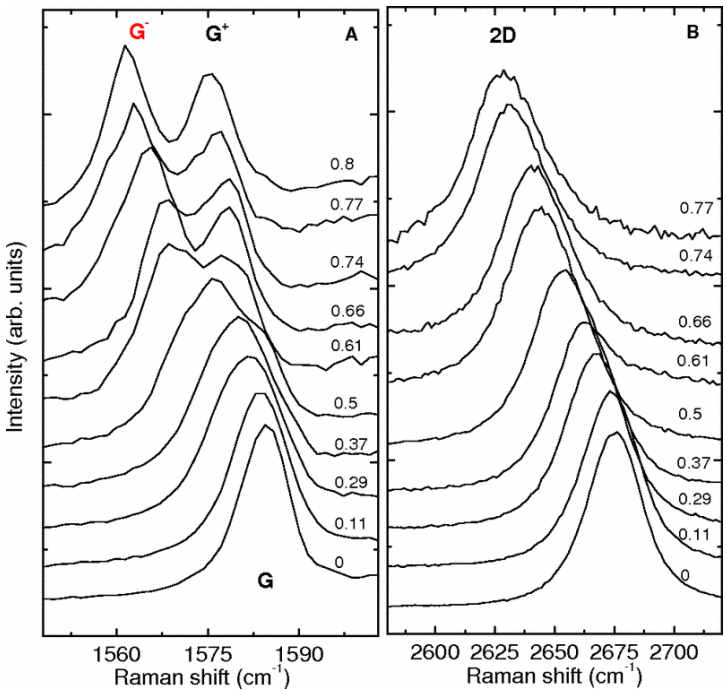

Figure 2.26: Raman spectra of G and 2D peaks under uniaxial strain; (a) G peak splits into two peaks, $G^{+}$and G^{-}; (b) the 2D peak shifts position only[78].

Hang et al. [79] reported defects on graphene with 30 keV helium ion beam (HIM) and proposed to reduce or remove the substrate swelling by a tilt of the beam. This study reported solutions involving backscattered ions and extricated substrate atoms that decreased the number of defects during the milling of graphene nanodevices.

The Raman spectroscopy images show the main pristine graphene peaks G and 2D around ~1580 cm^{-1} and ~2680 cm^{-1}, respectively. The 2D peak is the breathing mode of the graphene hexagonal ring, and the G peak is high optical phonon mode E_{2g}[80]. In terms of the defects in the graphene, other peaks appear around the D peak at ~1345 cm^{-1}, while 1600 cm^{-1} is the D' peak, where it reflects defects or disorder in the graphene. The Raman spectrum in Figure2.27 is clearly shown the G, D, and D' peaks, which are important because they provide information on the defect density [75, 81, 82] and defect types [83].Therefore, the I_D/I_G intensity ratio is important for measuring the defect density/length, which can be explained using a local activation model [81].The I_D/I_G ratio varies depending on the L_D between two defects, as described in the following equation:

$$\frac{I(D)}{I(G)} = C_A \frac{r_A^2 - r_s^2}{r_A^2 - 1r_s^2}\left[e^{\left(\frac{-\pi r_s^2}{L_D^2}\right)} - e^{\left(-\pi(r_A^2 - r_s^2/L_D^2)\right)}\right] + C_S\left(1 - e^{\left(-\frac{\pi r_s^2}{L_D^2}\right)}\right), \qquad (2.11)$$

Where r_s is the radii of the structurally disordered region (S-region), and r_A is the surrounding active region (A-region). These lengths are used to define the Raman active region [81].

An He^+ ion source was used to create patterning in a single layer of graphene. A high ion energy at 30 keV was used with a patterning resolution of 1 pixel/nm^2 and a dwell time of 3 μs. The Raman spectra for various irradiation doses for single layer graphene are shown in Figure 2.27. Even though the imaging dose is lower than that used for milling, it is still enough to create defects in or damage the graphene. The sputtering of substrate atoms is a key source of indirect damage to graphene, so tests on SiO_2 were carried out in order to control or reduce the substrate swelling during milling. From the AFM results, with dose varying from 0.4 x 10^{18} to 2.5 x10^{18}they observed that swelling removed for tilt angles equal to or greater than 40°,but the swelling height was observed at 0° tilt and increase with increasing the irradiation does. Therefore, they use an angle of 43° with irradiation of 6.24x10^{17} ions/cm^2 and a 30-nm wide line in the graphene. Figure 2.28(a) shows the AFM, and the profile of the milled cross area is an asymmetric V-shape where the carved line is deep in the centre and shallower near the edge. Figure 2.28(b) shows the Raman spectra point near the milling area fitted with three Lorentzians. Raman mapping of *I(G)* was used to define the boundaries of the graphene because it does not depend on edges, as *I(D)* does,

as shown in Fig. 2.28(c) [76]. Figure 2.28(d) shows the *I(G)* position where it crosses an edge to the graphene. The edge is shown because the *I(G)* position is weaker than that inside the graphene. The boundaries of the graphene were defined at ~400 nm, where the *I(G)* position begins to increase, as shown in Figure 2.28(c). There are two explanations for this. The first is that *I(G)* is constant across the graphene, but at 300 nm, it changes due to (1) the D' peak starting to appear beside the G peak, as shown in Fig. 2.28(b); and (2) the D band begins to broaden. Note that the point selected near the milling area may not be centred at the carved line, but it is still on edge. This is because it was manually aligned.

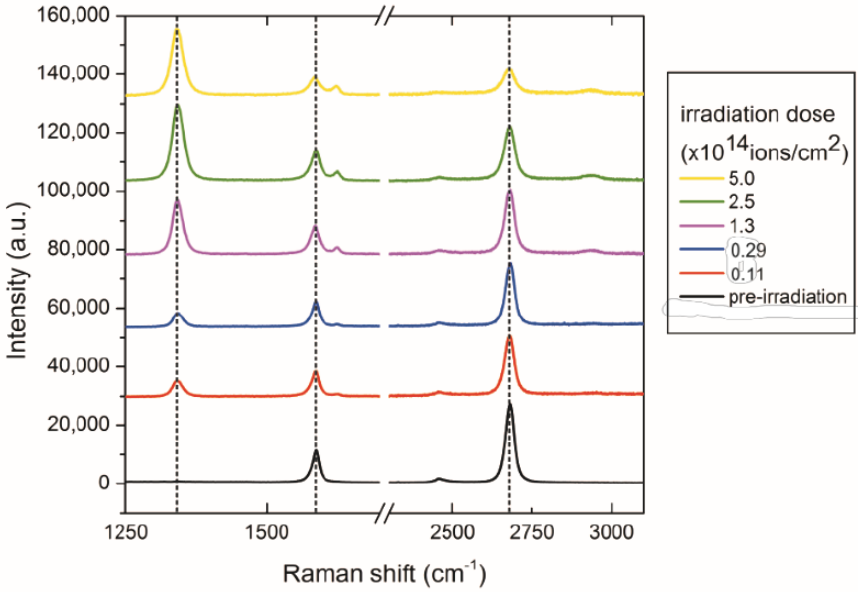

Figure 2.27: Single layer graphene Raman spectra before and after different doses of irradiation.

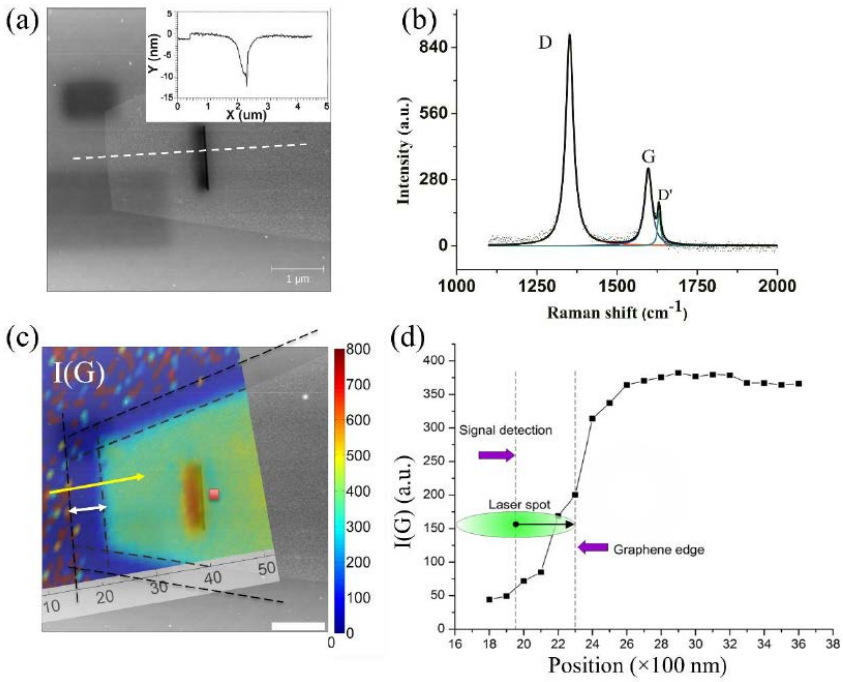

Figure 2.28: (a) AFM topography image of the graphene after HIM at 43º, 6.24 × 10^{17} ions/cm^2, and a 30-nm line. (b) The Raman spectra of the point near the milling area. (c) *I(G)* Raman mapping on top of the AFM image. (d) *I(G)* positioned across from the edge of the graphene.

Figure 2.29 shows L_D plotted using Eq. (2.11) and the following values: r_s = 1 nm, r_A = 3 nm, and $C_A = 160E_L^{-4}$ where $E_L = 2.33\ eV$ is the excitation energy of the laser. In Stage 1, $C_S = 0$, which is less than 10% for all defects types is used as value[83], and C_S~1 in Stage 2. The $L_{D(A)}$~1.5 nm, $L_{D(B)}$~8.5 nm, $L_{D(C)}$~4.0 nm or ~7.0 nm, $L_{D(D)}$~2.5 nm.

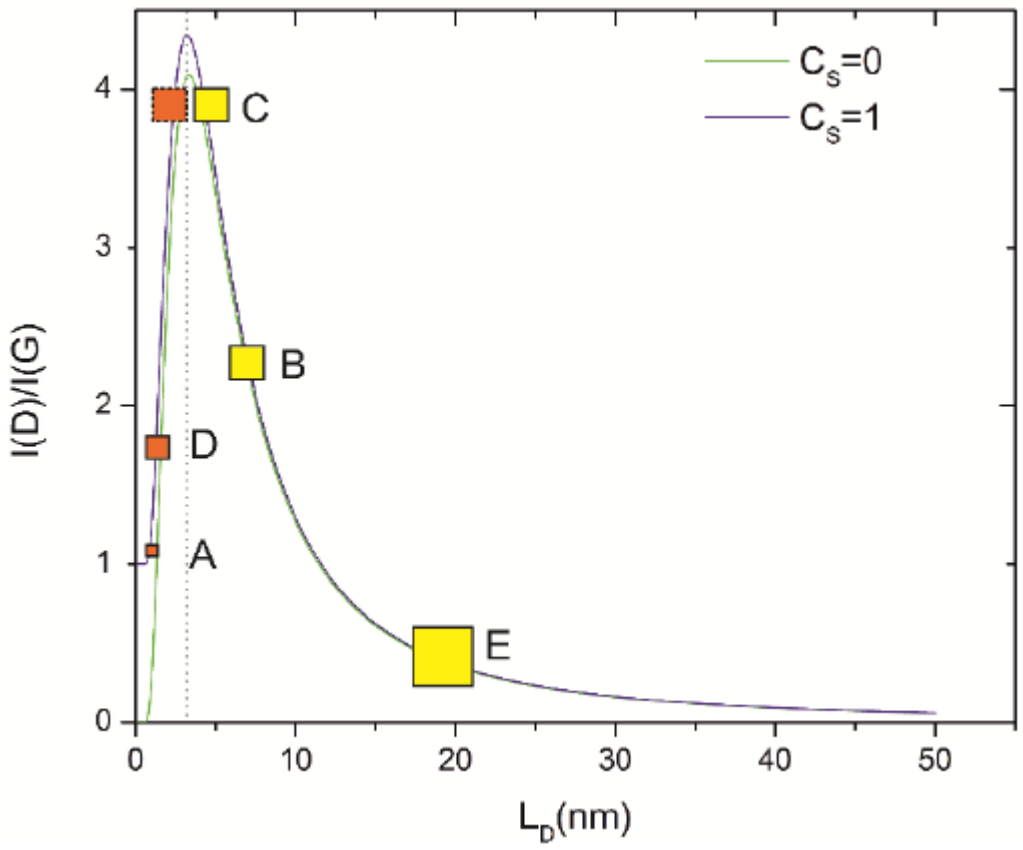

Figure 2.29: L_D plotted using Eq. (2.1). The green curve is presented for $C_S = 0$, and $C_S \sim 1$ is the violet curve. The yellow boxes represent Stage 1, and the orange boxes represented Stage 2.

2.3.2 Tip-Enhanced Raman spectroscopy (TERS) Application

2.3.2.1 Early Reports on TERS

Nie and Emory[84] reported an enhancement of 10^8–10^{14} for single-molecule detection of molecules absorbed on a silver substrate. Anderson reported that AFM tip coated with gold was used to provide the surface enhancement by removing the sulphur film layers at the nanometer scale and then provide surface enhanced Raman scattering (SERS) substrate for ultra-trace analysis[85]. Figure 2.30(b) shows the Raman spectrum when tip away from the sulfur film, and of the Raman spectrum with enhancement factor 10^4 was estimated when the tip in contact with sulfur film as shown in Figure2.30 (a). Furthermore, Sun and Shen reported a Raman mapping and enhancement of 10^4 for 1s on Si using an integrated near-field scanning optical microscope (NSOM) and Raman with the same objective lens [86]. The Raman spectrum obtained using this method is presented in Fig. 2.31.

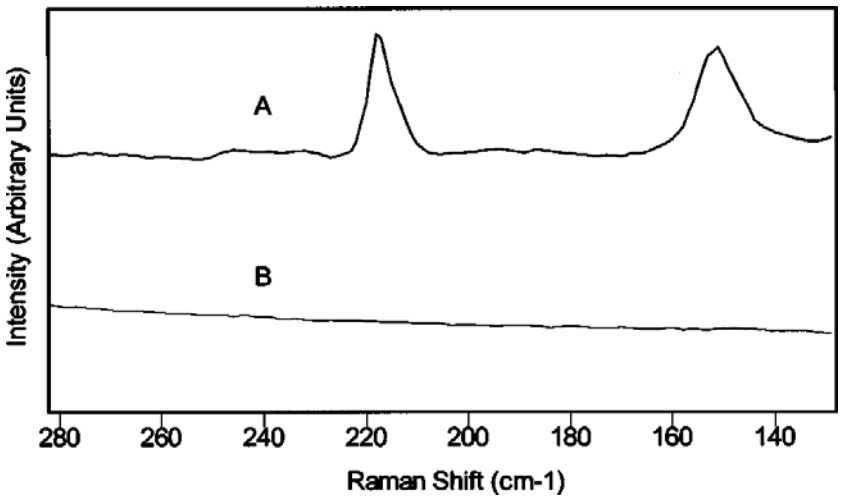

Figure 2.30: (a) Raman spectrum using an AFM tip contact on sulphur film; (b) Raman spectrum when the tip is not in contact. Adapted from [85].

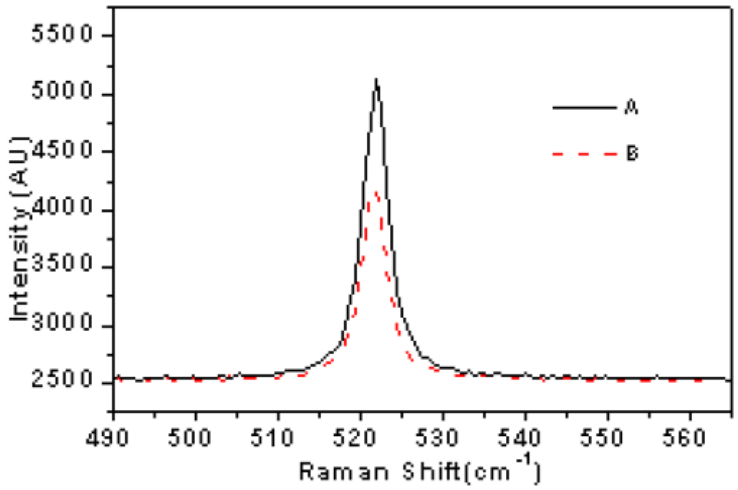

Figure 2.31: (a) Raman spectrum of Si when the tip is in contact with the sample; (b) Raman spectrum of Si when the tip is not in contact with the sample. Adapted from [86].

Hanafusa et al.[87], presented an integrated system of AFM-TERS measurements of strain and surface undulation on a strained silicon (s-Si) sample formed by sputter epitaxy. They compared their results with those obtained from s-Si formed using a gas-source molecular beam epitaxy (GS-MBE) method [87]. They found smooth surface and uniform strains in the s-Si sample that was formed by sputter epitaxy when compared with the s-Si sample formed by GS-MBE, as can be seen in Fig. 2.32.

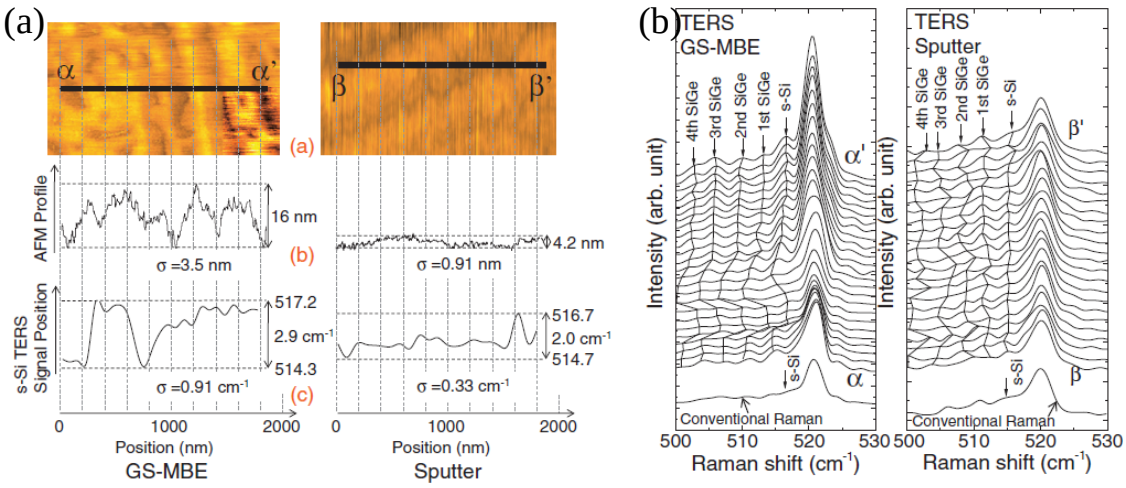

Figure 2.32: (a) AFM and TERS topography with profiles; (b) TERS spectrum with conventional Raman single [87].

2.3.2.2 TERS for graphene

TERS is a promising technique that can be used to investigate graphene with high spatial resolutions and high enhancement. The results of some TERS experiments on graphene have been reported in the literature [88-91]. Stadler et al.[88], used top illumination configuration of TERS with STM. In the aforementioned study, images of graphene defects and C-H stretching were investigated with a high resolution (<12 nm) and with strong enhancements of up to 80, as shown in Fig. 2.33[88]. Single-layer graphene was used for this study, and was produced by the Scotch-tape method on gold and with the CVD method on copper.

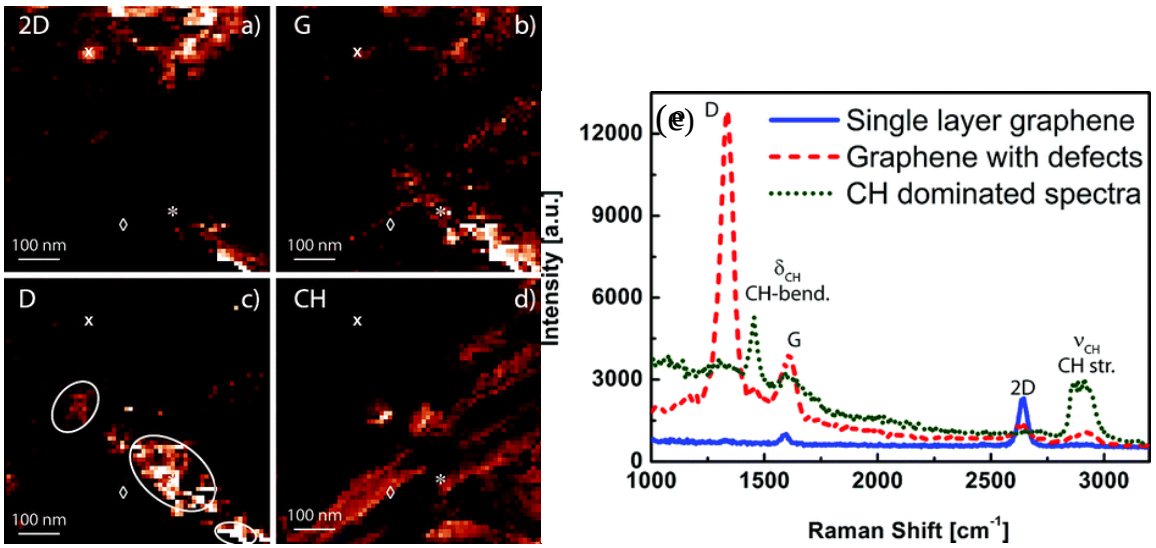

Figure 2.33: Raman image of graphene on Cu. (a) 2D peak image at 2634 cm^{-1}; (b) G peak image at about 1580 cm^{-1}; (c) D peak image at 1350 cm^{-1}; (d) CH image around 2800–3000 cm^{-1}; (e) TERS of graphene on Cu. The blue line is the Raman spectrum of SLG; the red line is spectra of the D peak of defect is 1350 cm^{-1}; and the green line is the CH banding (1450 cm^{-1}) and stretching modes (2800–3000 cm^{-1})[88].

In 2013, Rickman and Dunstan reported defects on multi-layer graphene flakes using TERS [90]. In that experiment, back-illumination TERS with AFM was used. As a result, they found that the D defect peak was enhanced in both samples, and other defects were detected and enhanced, as shown in Fig. 2.34and 2.35. In 2014, Vantasin et al. used TERS to study steps with 2 nm high of epitaxial graphene grown on 4H-SiC (0001) as shown in Figure 2.36(a)[91]. TERS and Raman far-field spectra for five points across step of 2D peak are shown in Figure 2.36(b). Raman spectra do not show double layer graphene characteristic at (~1375 cm^{-1}). They found the structure of step comes from substrate structure, and it does not come from the multi-layers graphene. As a result, the 2D peak position does not change in Raman far-field and TERS spectra due to the step structure as well as on both sides of graphene step no strain is present.

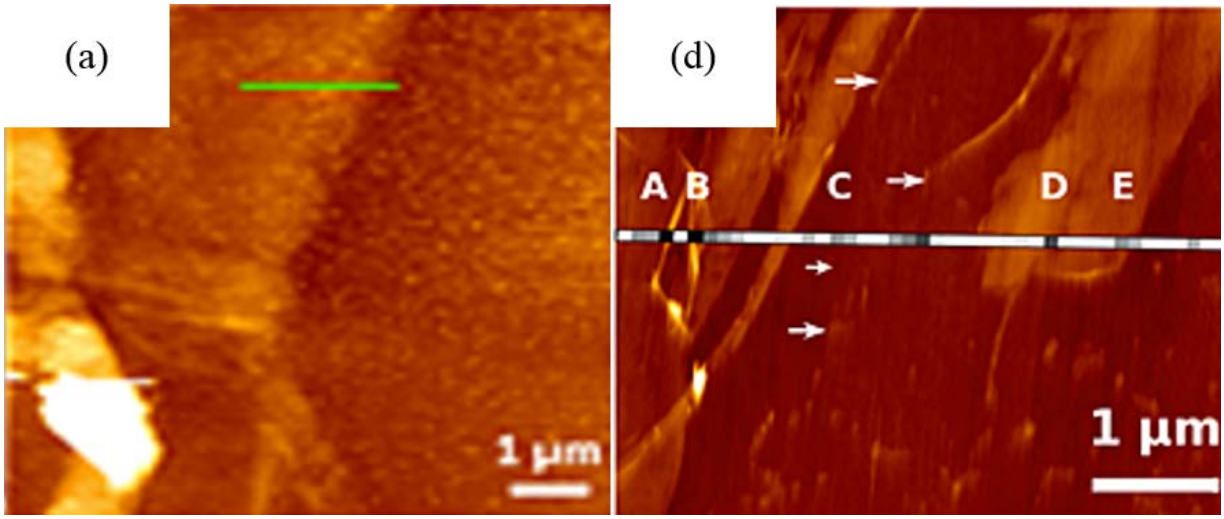

Figure 2.34: (a) Ultrathin graphite area measured using TERS. The green line is the TERS area. (b) TERS spectra: the blue line is the tip in contact, whereas for the black line the tip is not in contact. The spectra from the 1 to 5 G peaks only are present, and the D peak begins to show from 6 to 10[90].

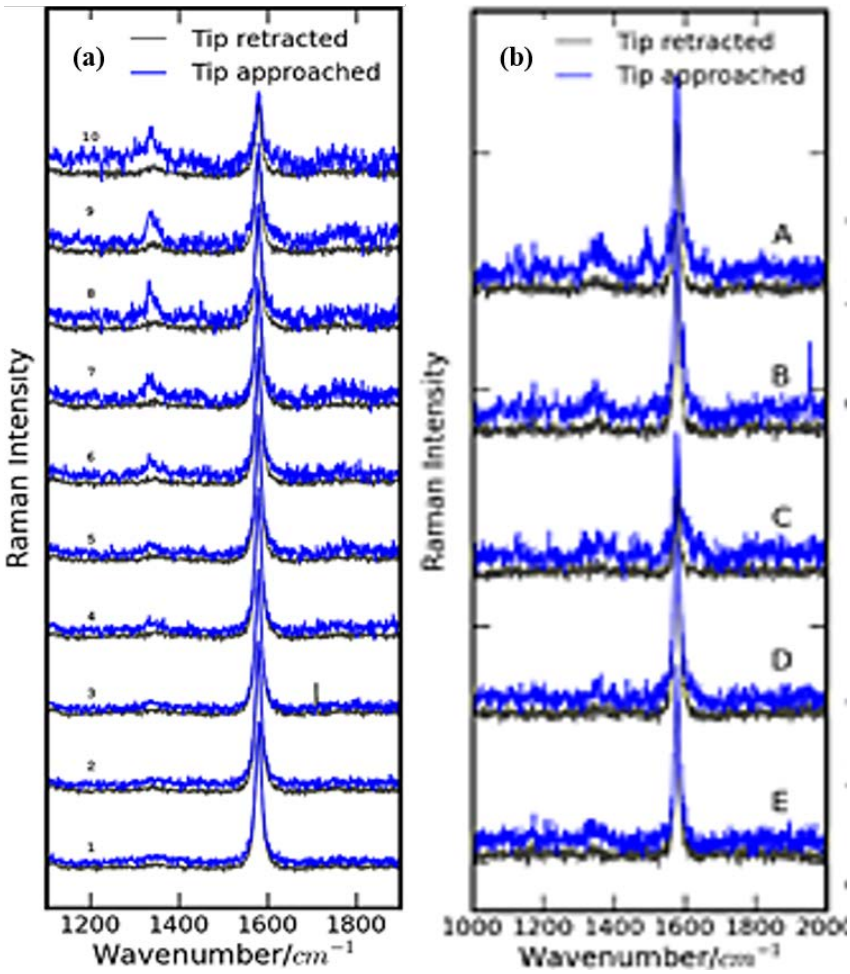

Figure 2.35: (a) AFM topography multilayer graphene area with the difference D band intensity through the line map. b) TERS spectra of the line across the AFM image presents the enhancement of G and D [90].

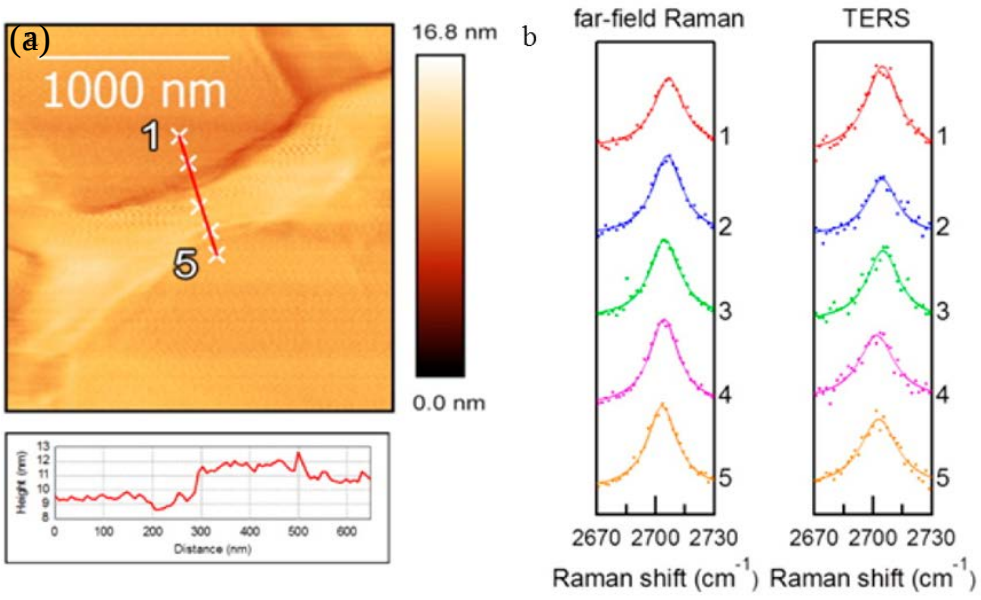

Figure 2.36: Step structure measurement using TERS. (a) AFM image with the height profile of the step, and (b) the 2D Raman spectra far-field and TERS spectra near-field for five points [91].

2.4 Motivation of this work

Graphene is a promising material for various applications. It is particularly relevant for high frequency and thin film transistors, NEMs switch, and resonators for mass sensing. The development of these devices among the other applications requires the investigation of the defect, edge, stress and strain characteristics of graphene. Several methods were used to measure and characterise graphene properties, such as SEM, TEM, and AFM. However, these technologies failed to provide the chemical information of graphene. Raman spectroscopy is one of the most important methods which has been heavily used to study the graphene properties including the effects of strain, edge formation [76],disorder, doping, and different types of defects [92, 93].However, Raman cannot be used to study the graphene properties in nanoscale due to limitation of the spatial resolution of Raman in microscale. Tip-enhanced Raman Spectroscopy (TERS) has emerged as a new characterisation technology that can be used to investigate critical properties that needs high spatial resolutions at the nanoscale range. TERS has been applied to study properties of several types of graphene, such as Scotch-tape-exfoliated graphene on glass[90, 94-100], on Au[88], CVD-grown graphene on glass[100],epitaxial-grown graphene on SiC [101].However, there are only a few studies characterising graphene nanodevices using TERS. In particular, to the best of my knowledge, helium-ion irradiated graphene has not been studied yet via TERS.

.

Chapter 3: **Tip-Enhanced Raman Spectroscopy**

3.1 Introduction

Raman spectroscopy is one characterisation technology which is used to study the chemical and structural information of materials. However, conventional micro Raman spectroscopy has a laser diffraction limit that prevents from observing nanoscale structure with nanometre spatial resolution. Wessel proposed TERS as a promising technique for the characterisation of various kinds of samples at the nanoscale in 1985 [102, 103]. Wessel's idea was to combine SPM technique (e.g. STM) with surface-enhanced Raman spectroscopy (confocal Raman spectroscopy), as shown in Fig. 3.1. In (SERS), the electromagnetic field (EM) enhancement and Raman signals are produced from a roughly coated metal substrate, but Wessel's original idea was to use a sharp metal-coated tip in contact with sample in order to enhance the structure. This is due to at the apex of the coated tip the surface plasmons obtained. The tip scans over the sample and obtains the topography of the sample at nano-metre resolutions. The first application that used this technology appeared ten years after Wessel's proposal[104].

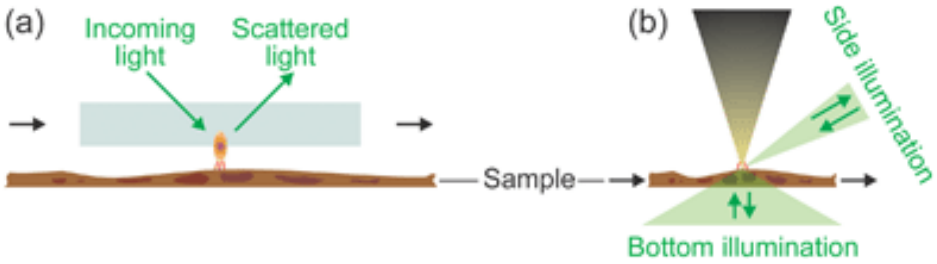

Figure 3.1:The basic concept of Wessel's TERS idea [104].

TERS characterisation uses a tip that can provide enhancement of electromagnetic (EM) field via the near-field effect. In principle, high spatial resolution Raman mapping down to 10–12 nm is possible with TERS [105, 106]. One of the most promising features of TERS is its ability to investigate the influence of strain on the sample. The laser in visible range is used for TERS characterisation, and the power range of the laser could vary from microwatts to milliwatts. In comparison with SERS which requires a level of sample surface roughness, TERS does not require a particular surface. In TERS different feedback devices – e.g., AFM, STM, and shear force microscope (SFE) is controlled to keep the distance between the tip and sample. TERS has been used for various materials, such as semiconductor materials[86, 107], nanomaterials [19, 108]and the others[109].

In this chapter, basic principle of TERS measurements including signal enhancement mechanism will be introduced. Introduction of MV4000 system that has been used in this study. Then how the measurement system has been optimised will be described. For optimisation a single-layer CVD-fabricated graphene sample was used. Conventional micro Raman spectroscopy was conducted with532nm (2.33eV) laser excitation. In order to measure the structure in nanoscale, the AFM-TERS (Nanonics MV4000) integrated system was used. At the initial stage of this project, optimal measurement conditions have been explored by adjusting laser excitation power and exposure time in order to obtain the best conditions for TERS signal enhancement. This procedure will be detailed in this chapter. Finally, the role of the tip position with respect to the position of the laser spot will be addressed in order to achieve higher signal enhancement.

3.2 Raman spectroscopy

The classical derivation of light scattering from molecules is presented in Ref. [110]. The basic process of one vibration is presented in Fig. 3.2, which depicts two energy states. The first energy state is the lowest vibrational level, where most of the molecules are present at room temperature. The second energy state is the highest in the virtual level, which is created from the interaction of electrons with the laser and the present polarization. The Rayleigh (i.e. elastic) scattering of Raman is observed as the molecule returns back to its normal (vibrational) state. At this stage, the emitted photon will have a wavelength equal to the incident photon. However, when the molecules return back to their normal (vibrational) state, the energy emitted photon $h\nu_o - h\nu_m$is lower than that of the incident photon $h\nu_o$, and carries a longer wavelength. This is known as Stokes scattering Raman. The anti-Stoke of Raman are obtained at higher energies and shorter wavelengths $h\nu_o + h\nu_m$ since the molecules are in the phonon state, which is a virtual state, before the molecules return back to their normal (vibrational) states.

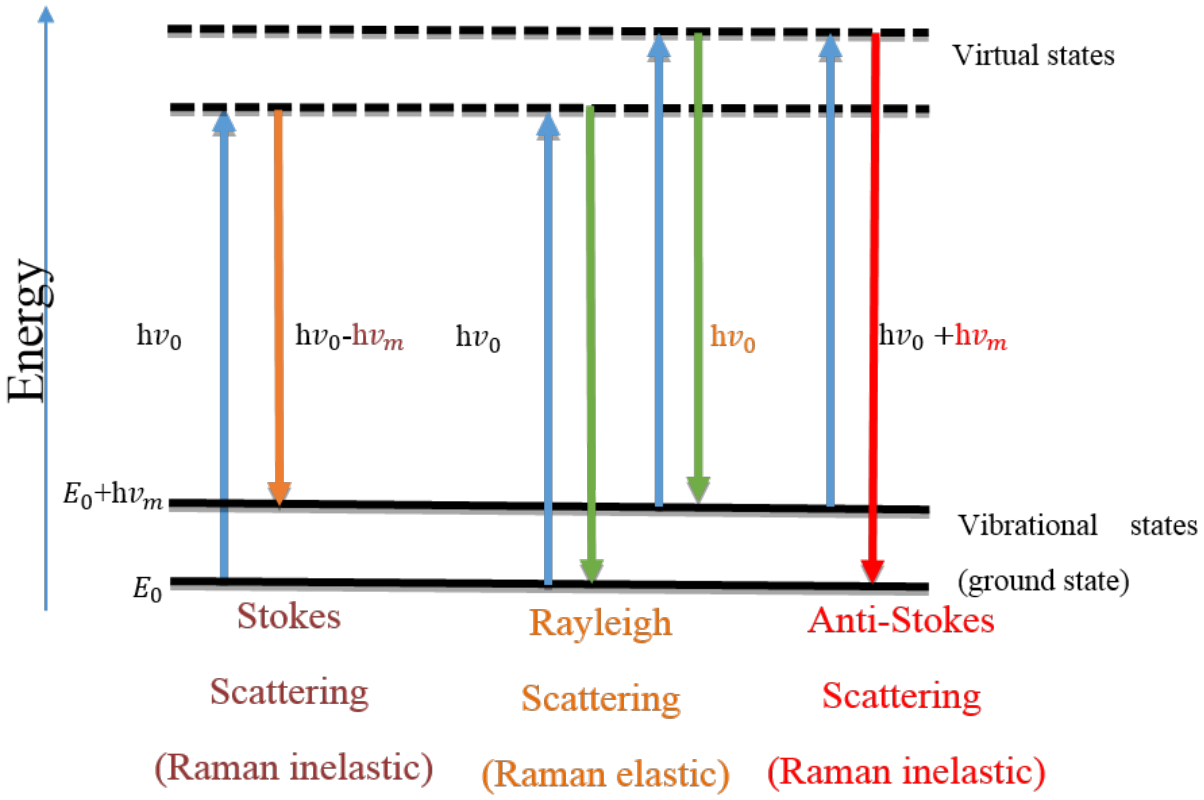

Figure 3.2: Diagram of the energy level of Raman scattering showing Rayleigh, Stokes, and anti-Stokes scattering.

The light source used in Raman spectroscopy is a laser. Figure 3.3 shows that the laser is polarized by an electromagnetic wave that is traveling in the *z*-direction, and consists of electric (E, *x*-direction) and magnetic components (H, *y*-direction).

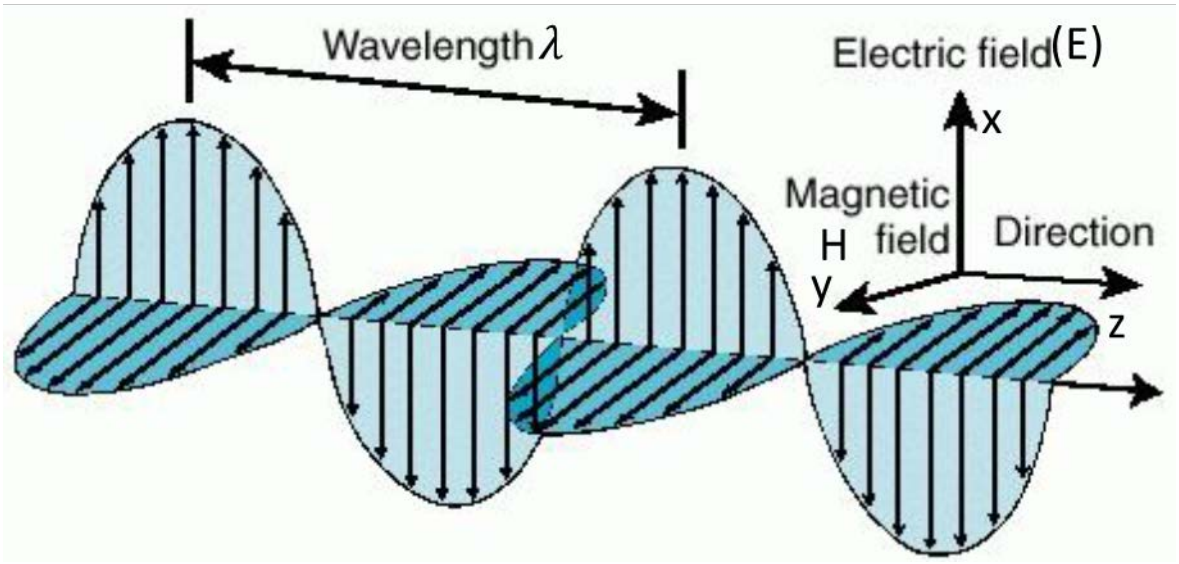

Figure 3.3: Diagram of electromagnetic radiation [111].

Classical Raman scattering can be expressed with the following equation:

$$E = E_0 \cos(2\pi h v_0 t), \tag{3.1}$$

Where E is the electric field strength of the electromagnetic wave with time *t*, E_0 is the vibrational state, and hv_0 is the energy per photon. A dipole moment μ that represents the molecule irradiation by this laser is as follows:

$$\mu = \alpha E = \alpha E_0 \cos(2\pi h v_0 t), \tag{3.2}$$

Where α is the polarizability of the molecule. This also varies with time as:

$$\alpha = \alpha_0 + \alpha_m \cos(2\pi h v_m t), \tag{3.3}$$

Where α_0 is the polarizability of the equilibrium of the molecule, which changes with the vibration of the molecule, and hv_m is the energy per photon of the molecule.

The dipole that results from Eqs. (3.22) and (3.3) can be written as:

$$\mu = [\alpha_0 + \alpha_m \cos(2\pi h v_m t)] \times E_0 \cos(2\pi h v_0 t)]. \tag{3.4}$$

This equation can be grouped into three terms as follows:

$$\mu = \alpha_0 \times E_0 \cos(2\pi h v_0 t) + 0.5\alpha_m \times E_0 \cos(2\pi (h v_0 + h v_m) t) + 0.5\alpha_m \times E_0 \cos(2\pi (h v_0 - h v_m) t). \tag{3.5}$$

From these equations, the oscillating dipole moment of the photons is shown at different frequencies. The first component represents Rayleigh scattering, while the second and third components of the equation represent anti-Stokes and Stokes scattering, respectively. Note that Raman scattering cannot be obtained when the molecular vibration is independent of the polarizability (i.e., $\alpha_m = 0$) and vibrational frequency ($hv_m = 0$).

Each vibrational or rotational mode corresponds to a relative frequency shift that is independent of the wavelength of the laser source. The collection of different frequencies or Raman shifts undergone by the molecule is known as the Raman spectrum. This provides an individual fingerprint that characterises each molecule, and allows for its identification and structural analysis.

3.3 Principle

As can be seen in Fig. 3.4, TERS aims to overcome the aforementioned limitation of Raman spectroscopy by increasing the spatial resolution through using a sharp metallised AFM tip that focused on the sample in the centre of Raman visible laser being incident on the tip apex, which is the main component in TERS. The electromagnetic (EM) field enhancement is obtained at tip-apex because of a combination of two factors, Localised Surface Plasmon (LSP) resonance and lightning rod effect[112] . The Raman scattering signal from the materials under the tip is enhanced due to the EM field enhanced. By scanning the sample under this condition, Raman intensity map can be obtained with a high spatial resolution overcoming the diffraction limit of the Raman spectroscopy.

With the tip, both the far-field and near-field light be collected. The tip's diameter is 10- 100 nanometers that are associated with the spatial resolutions of the topographic image of the sample's surface and Raman mapping. The separation between the tip and sample is about 10 nm. Several kinds of TERS tips could be used for characterisation such as metallic tips (e.g. silver or gold)[19]as well as dielectric tips that are coated by metal[18, 113].

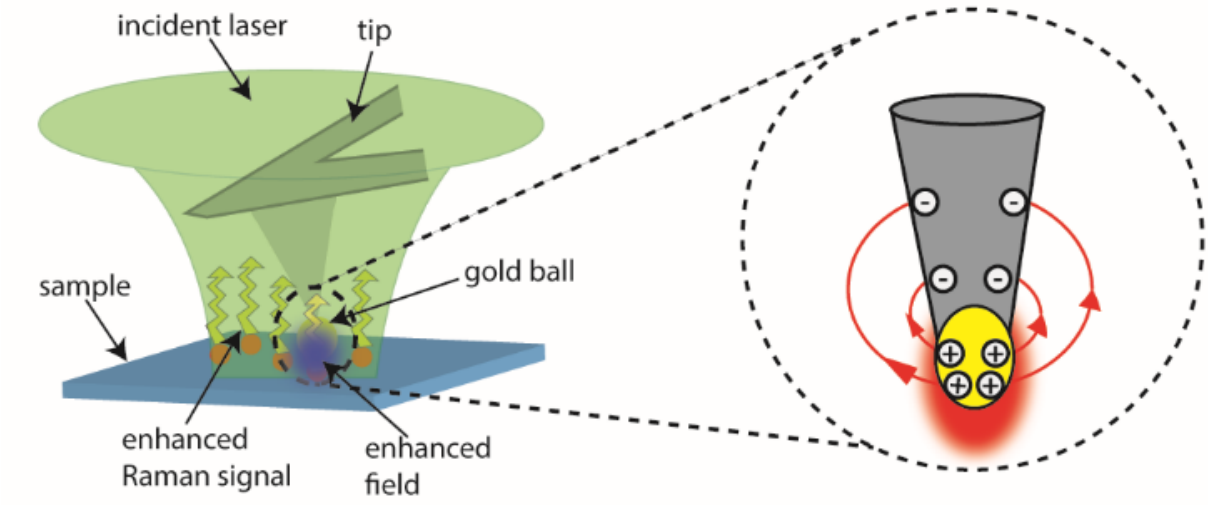

Figure 3.4: Illustration of TERS concept: a combination of SPM technology with Raman spectroscopy.

3.3.1 Enhancement Mechanism of TERS

In TERS, the Raman signal enhancement is obtained from the interaction between the tip and chemical molecules or material surfaces [112]. The tip receives and emits the scattering light from the sample, and this increases the sample molecule’s or sample surface’s response to Raman scattering. In TERS, high resolution is generated by transferring the non-propagating

evanescent waves to propagating waves that operate close to the tip end [114].At certain frequencies, the electric field close to the tip is supposed to be axially symmetric for these theoretical studies[73, 102]. The Raman dipole in the sample is generated by the separation of the Raman excitation field and the local surface plasmon field, which is generated from the metal tip exposed to the laser. The Raman intensity of the electric field generated by the tip inside the laser spot is calculated by taking the average of the square modulus of the local field intensity. The near-field distance for 0D, 1D, and 2D samples can be obtained using the following equations:

$$d_{0D} = \left(\Delta + r_{tip}\right)^{-12} \quad (3.6)$$

$$d_{1D} = \left(\Delta + r_{tip}\right)^{-10} \quad (3.7)$$

$$d_{2D} = \left(\Delta + r_{tip}\right)^{-8} \quad (3.8)$$

Where Δ is the tip-sample separation and r_{tip} is the radius of the tip. These equations have been used to evaluate the enhancement of the Raman signal in TERS[19, 115] .

3.3.2 Calculation of Tip-Enhanced Raman Spectroscopy (TERS) contrast and Enhancement Factor

The ratio of the strength of the electromagnetic field at the tip (E_{tip}) to the strength of the electromagnetic field at the sample in absence of a tip in contact (E_0)[115]is termed as the enhancement factor g of the electromagnetic field, as shown in Eq. (3.9).

$$g = \frac{E_{tip}}{E_0} \quad (3.9)$$

The square of the strength of the electromagnetic field determines the intensity of light.$g^2_{\lambda_{laser}}$is the enhancement factor of the excitation light at the laser wavelength λ_{laser}. TERS signals depend not only on the wavelength of Raman-scattered light (λ_{Raman}) but also on the wavelength of excitation light (λ_{laser}).Equation (4.5) expresses the enhancement factor of the TERS signals (EF_{TERS}).

$$EF_{TERS} = g^2_{\lambda_{laser}} . g^2_{\lambda_{Raman}} \approx g^4 \quad (3.10)$$

The enhancement factor of the electromagnetic field depends on the wavelength, chiefly after the plasmon resonance spectrum of the tip. It can be assumed that $\lambda_{laser} \approx \lambda_{Raman}$ provided that the Raman shifts are very small. In this situation, the TERS enhancement factor can be valued at g^4. It is worth mentioning that one needs to consider the difference between

the field enhancements at λ_{Raman} and at λ_{laser} for accurate measurements of the enhancement factor, such as for comparison with numerical simulation data[116]. Calculation of the two factors is required for determination of the TERS enhancement factors on the basis of experimental data[117]. First, the difference between the far-field and near-field signals is computed using the non-enhanced and enhanced Raman signal intensities. Then, a geometry factor is calculated assuming that the size of the sources of near-field and far-field are different – i.e., a dissimilar number of molecules are involved in the two signals. Contrast is defined in two different ways in the available literature; these are:

$$C = \frac{S_{tip}}{S_0} \qquad (3.11)$$

$$C = \frac{S_{near\ field}}{S_{far\ field}} = \frac{S_{tip} - S_0}{S_0} = \frac{S_{tip}}{S_0} - 1 \qquad (3.12)$$

In the above equations, S_0 refers to the background signal in the absence of the tip. Since Eq. (3.11) provides a direct measure of the quality of the image that can be acquired through the TERS technique, this definition is practically more relevant[18, 117]. When the enhancement is comparatively weak, the signal S_{tip} computed in the presence of the tip is superimposed on a comparatively larger non-enhanced background S_0 in the absence of a tip at very small distances from the sample. The resolution of the image formed is adversely affected by the strong background signal since the background signal S_0 is produced in the entire volume or area of the sample. On the other hand, Eq. (3.12) provides a more accurate expression of contrast if the enhancement factors are computed and compared to the SERS measurements or numerical simulations (employed in [19, 107, 108].). As per this definition, the contrast refers to the ratio of the far-field ($S_{farfield}$) to the near-field ($S_{nearfield}$) signal intensities.

It is clear that these definitions differ only by a value of 1. In other words, these definitions differ (3.11) and (3.12) significantly only when there is a weak enhancement. One can compute contrast only when non-enhanced and enhanced signals are computed at the same site on a uniform sample. When the far-field signal cannot be computed – for instance, in the case of monolayers of weakly scattering molecules – the upper limit for the intensity of the signal is determined on the basis of the degree of noise. The degree of noise is taken as an exceedingly rough estimate, which is largely dependent on the technique of determination – such as the standard deviation vs. peak-to-peak difference of the noise. The difference in source volume of the near- and far-field signals should be considered when determining the enhancement factor[18, 108]. The geometry factor can be estimated using the source areas in the case of opaque samples or thin films. As the far-field signal is produced in the whole

laser focus,$A_{far\ field} = r_{laser}^2$. The radius of the laser focus is usually employed to determine the far-field source area. On the other hand, it is more difficulty to determine the area where the near-field signal is generated; however, it is usually estimated withπr_{tip}^2, where r_{tip} is the tip radius that can be resolute using SEM. Nevertheless, some researchers indicate that, at least in certain cases, the enhancing region is smaller than the tip apex [19].Diameters of both areas can be determined accurately by calculating the lateral resolution of both TERS and confocal Raman images [18, 108]. However, Eq. (3.13) and (3.14) can be used to determine the TERS enhancement factor:

$$EF_{TERS} = C\,\frac{A_{far\ field}}{A_{\ near\ field}} \quad (3.13)$$

$$EF_{TERS} = \frac{S_{tip}}{S_0} * \frac{A_{far\ field}}{A_{\ near\ field}} \quad (3.14)$$

Far-field signals are produced in a volume when samples are bulky and have significant optical penetration depth. Hence, it is important to determine the ratio between near- and far-field volumes. The degree of enhanced field around the tip directed towards the *z*-axis and the optical penetration depth or the height of focus (the lower value is taken in both of these cases) needs to be determined. In general, determination of the conversion factor between EF_{TERS} and contrast usually makes use of several approximations; hence, reviewing different investigations and making a comparison between different studies and between theory and experiment proves to be difficult. Comparison becomes easy when the enhancement factors are presented together with an elaboration of the procedure used for the computation and the estimation of the figures. The researchers of this study propose to employ contrast factors in order to compare different studies because contrast factors can be determined experimentally and serve to be practically relevant as they provide direct information related to the quality of the TERS image[104].

An alternative strategy has been suggested by Pettinger et al. [20, 118]for determining the enhancement factor. This strategy makes use of experimentally determined figures. These researchers investigated the temporal behaviour of the TERS signals of molecules. They determined an exponential decay of the form $e^{(-t/\tau)}$ due to bleaching. The enhancement factor of the excitation light $g_{\lambda_{laser}}^2$ is expressed as the ratio of the time constants τ of tip and confocal-enhanced bleaching, assuming that there is not any difference in the lifetime because of two photon-processes or heating. This method cannot be used to calculate the enhancement of the Raman scattered light; however, assuming that the two enhancements

are almost the same, the TERS enhancement factor can be estimated by$g^4_{\lambda_{laser}}$. A detailed explanation of the different techniques for the determination of enhancement factors together with their comparative analysis is provided in Ref[119].

3.4 Introduction of TERS measurement instruments

A Nanonics Multiview MV4000 integrated with a Renishaw inVia Raman spectrometer, shown in Figure 3.5 (a), was used for TERS measurements. A schematic setup of TERS is shown in Fig. 3.5 (b). The top- illumination configuration is used in this system, where laser is exposed to sample from the top with an objective lens (50x magnification, NA=0.45). The Raman signals are collected by the same objective lens. The wavelength λ of 532 nm of Nd-doped Y-Al-garnet laser was used for TERS excitation. Quartz tuning fork with a commercial probe tip was used (Nanonics Imaging Ltd.) for feedback on AFM topography image and near-filed excitation. The top of the tip used in this study was coated with Au on and the size of this Au nanoparticle is about 200 nm in diameter. The laser power used in this measurement was 5mW. The laser spot with size 1.44μm and tip position are made aligned manually by using the tip controlling system. The tip height (z) was controlled by the tuning fork feedback, and the samples in–plan (x, y) position on the stage was controlled by the piezo stage driver as shown in Fig.3.6. In taking a TERS spectrum at a certain position two spectra with tip approached (tip in contact) and tip retracted (tip not contact) are taken. The distance between the tip and sample is ~10 μm when the tip is retracted. The spectra taken with the tip approached contains both near-field and far- field signals, whereas the spectra with the tip retracted has only the far-field contribution.

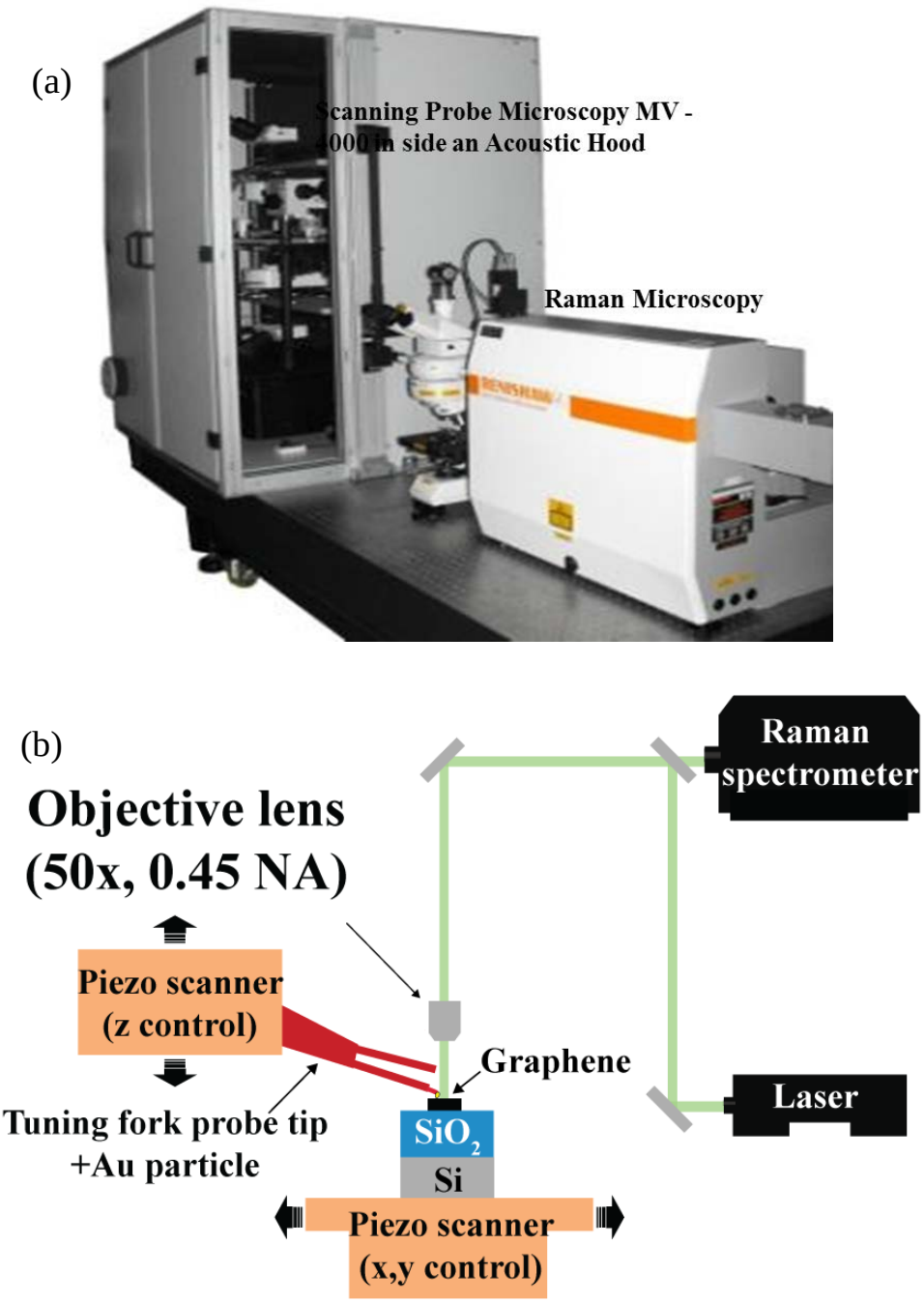

Figure 3.5: (a) Nanonics Multiview MV4000 combined with a Renishaw inVia Raman spectrometer. (b) A schematic of the TERS measurement setup with top-illumination.

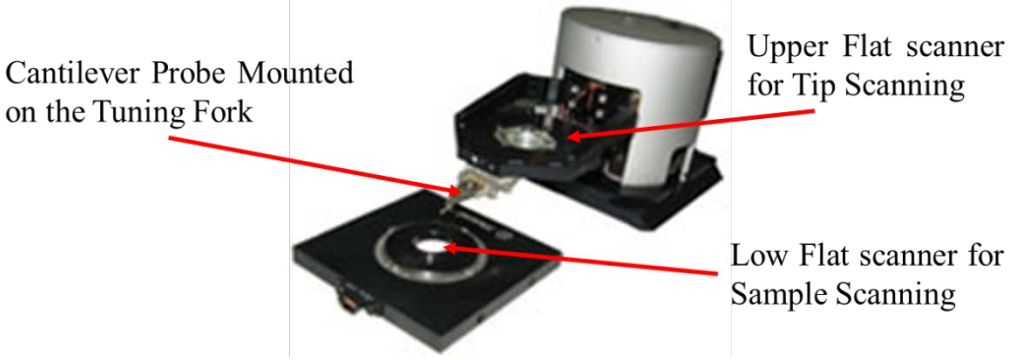

Figure 3.6: MV-4000 SPM setup head.

3.5 Process for optimisation of the system

3.5.1 Micro-Raman Measurement

1cm×1cm commercial graphene samples were produced based on a CVD graphene grown on copper being transferred to Si/SiO_2 were purchased from Graphene Supermarket[120].The surface of a sample is imaged using optical microscopy, as shown in Fig. 3.7(a).

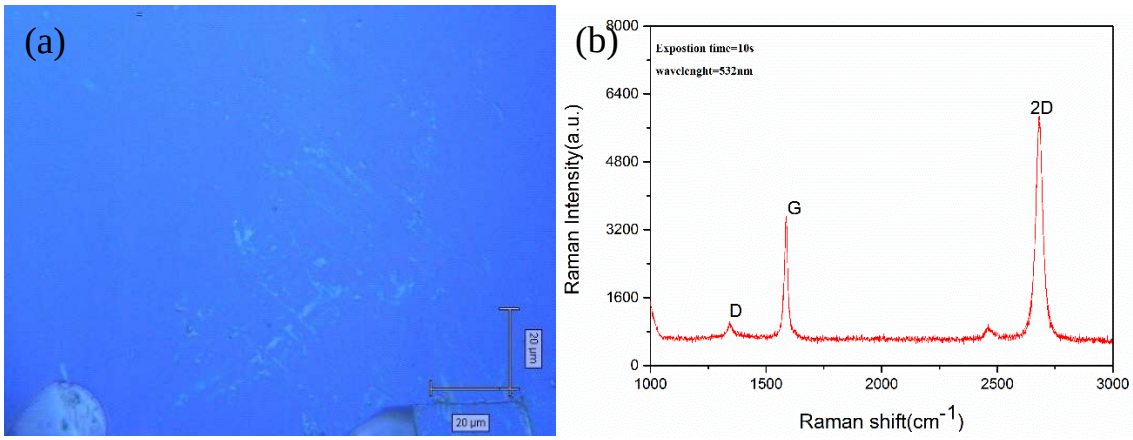

Figure 3.7:(a) Optical image of single-layer graphene; (b) Raman spectrum of single-layer graphene showing the main features of graphene – D, G, and 2D bands – with a laser excitation of 2.33 eV.

The most significant features of the Raman spectrum for graphene are presented in Fig. 3.7(b). The 2D or G' peak is around 2681 cm^{-1}; this peak indicates a second-order process[121]. The 2D peak is very sensitive to lattice perturbations, which affect the mechanical and electronic properties of graphene. Furthermore, the shape, width, and position of the 2D peak are directly related to the number of layers in the sample; its position, however, depends on the amplitude of the laser excitation[122]. Moreover, the 2D peak comprises a sharp peak, which indicates the single-layer graphene, as Fig. 3.7(b)

demonstrates. The optical image in Fig. 3.7(a) and the corresponding spectrum of graphene from 1000 to 3200 cm^{-1} with four peaks are shown in Fig. 3.7(b) indicate the presence of single-layer graphene, which is used for micro-Raman. The G peak appears at 1586 cm^{-1}, and this peak is E_2g (iTO and LO) with a tangential shear mode that is common to graphene and carbon atoms exhibiting sp^2 hybridization. The G peak is especially important because it is sensitive to strain and defects in graphene layers. This peak is a first-order Raman scattering of graphene. The second peak is the 2D or G' peak appearing at 2681cm^{-1}, and this is the second-order two-phonon of the D peak. This peak is another important peak for single-layer graphene, and the 2D peak does not require defects to be present in the spectrum [122, 123].The intensity ratio of the 2D peak and the G peak I_{2D}/I_G is used to identify the number of graphene layers; and the value extracted from this data is 1.69, and for single-layer graphene the 2D peak is twice the G peak. The full width at half maximum (FWHM) using Gauss fitting for the 2D peak is about 37 cm^{-1}[123].The third peak is the D peak (disorder-induced), which is around 1345 cm^{-1}. However, the D peak depends on the disorder; it does not depend on the number of layers (in contrast to the 2D peak), and it is the result of the A_{1g} mode. The relation between the intensity of the D and G peaks I_D/I_G is used to identify the number of defect in the graphene layer, and it is about 0.84 in this case.

3.5.2 TERS measurement optimisation procedure

In advance to the actual measurements of nanodevice-related structures, the AFM-Raman and TERS instruments, Nanonics MV4000 has been tested and optimised by using a commercial graphene sample. In this section, the test and optimisation procedures are described by considering key parameters in TERS.A standard single-layer graphene sample on a SiO_2/Si substrate is used for testing. As a starting point without tip, a Raman spectrum of the single-layer graphene with an incident laser power of ~0.5 mW and an integration time of ~10 s is presented in Fig. 3.8. The basic graphene peaks, G and 2D are presented but this laser power cannot be used because the intensity of the peaks is small comparing with micro Raman. In this experiment the integrated AFM-Raman system is usedd with long optical path ~ 348 cm Figure 3.8 (a),and this due to the layeout .The introdues laser to system is required addinal mirrors in order to reflect the laser in compare with miroRaman and these mirrors is produce additional lost of laser power .due to the laser.As a result, the laser power should be double in compare with miroRaman because the apply laser and Raman single pass throghout the long optical path and as a result the laser power intensityof get lower.

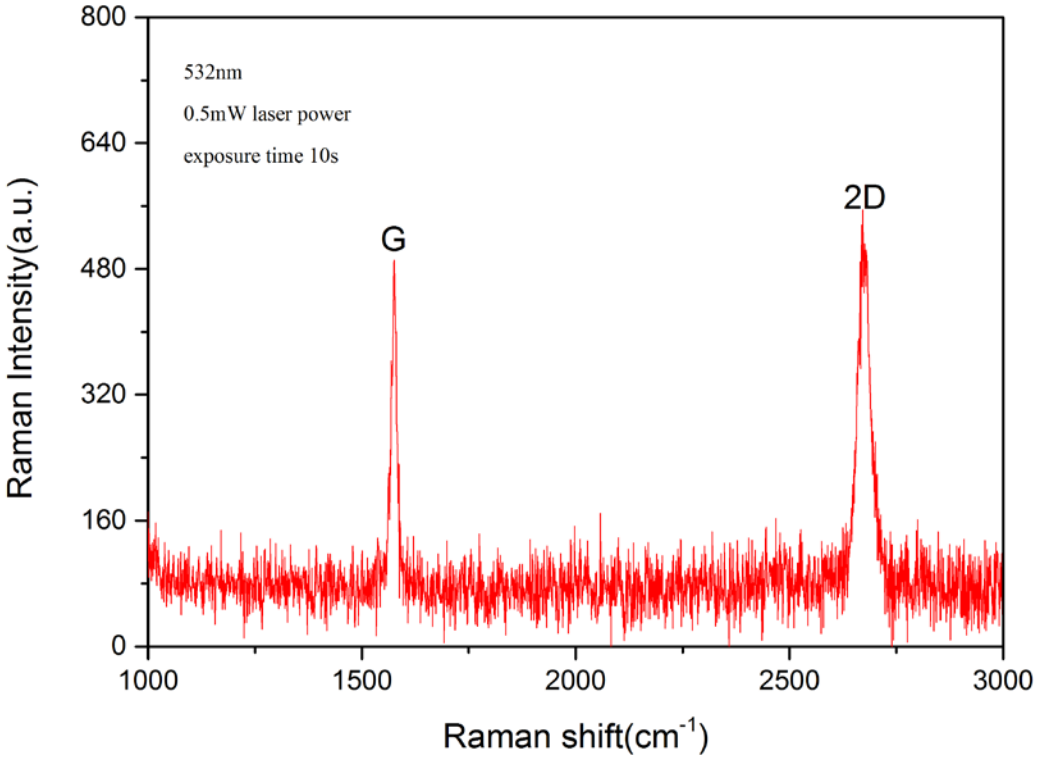

Figure 3.8: Raman spectrum of single-layer graphene using the AFM-TERS integrated system with a laser power of 0.5 mW. This shows the main features of graphene: G and 2D bands with laser excitation.

It is expected that the Raman signal intensity increases with increasing the laser power. Therefore, the incident laser power was increased to ~2-5 mW using the same objective lens and an integration time of ~10 s. As shown in Fig. 3.9(b) and (c), the Raman intensities of the individual peaks are increased. When the peak intensity is plotted as a function of the laser power as shown in Fig. 3.9(d), the intensity increases linearly to the power, indicating no nonlinear behaviour in this laser power range. As a result, the laser power of ~5 mW is decided to be used for further measurements. Raman spectra has been taken using this power in Mv4000 system and this laser power this measurement dos not damage the graphene .according to our estimation the power we can apply to sample in MV4000 is about ½ of power apply in micro Raman. That mean if we apply the power up to 5mw should not damage the sample.

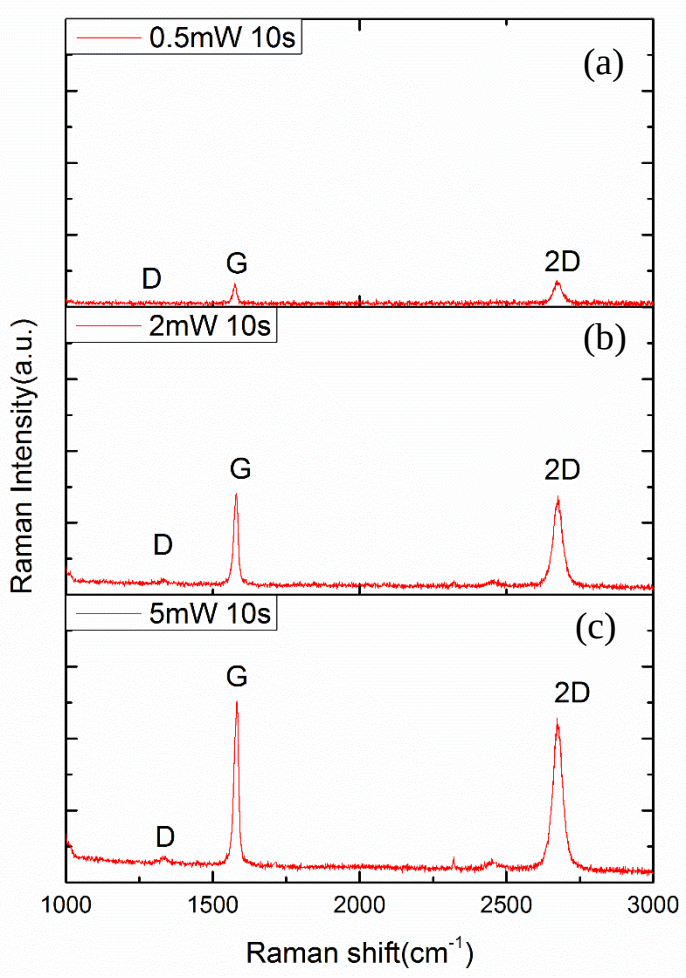

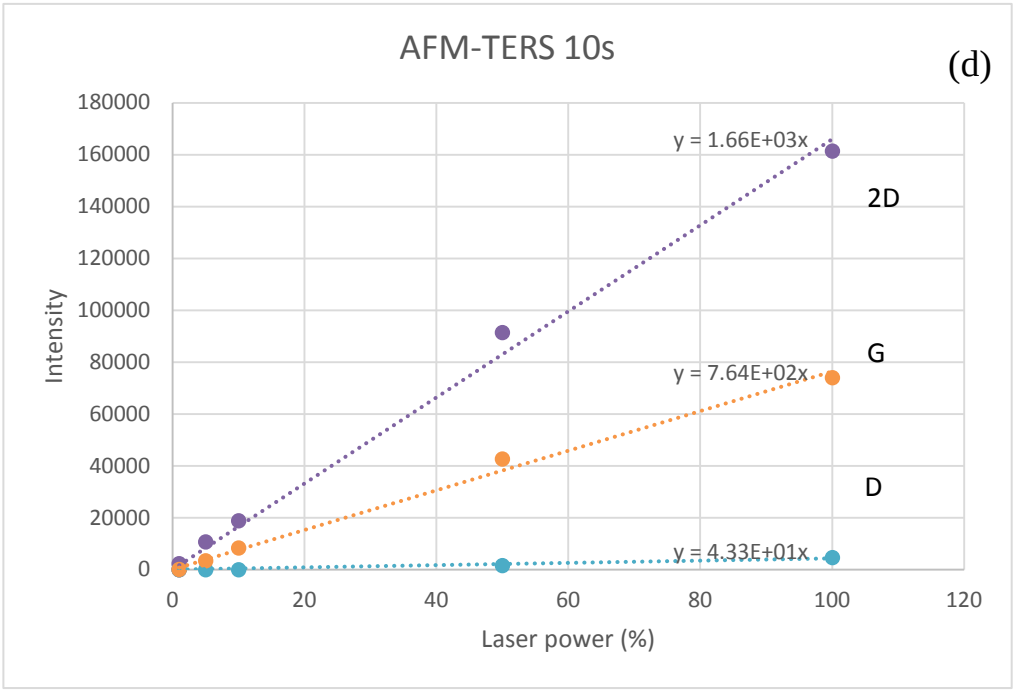

Figure 3.9: Raman spectra of single-layer graphene using the AFM-TERS integrated system with different laser powers. (a) Raman spectrum with 0.5 mW laser power; (b) Raman spectrum with 2 mW laser power; (c) Raman spectrum with 5 mW laser power; (d) 2D, G, and D peaks with different laser powers. Raman intensity increases with higher laser powers.

Although the Raman intensity of graphene improved with increased laser powers, the laser intensity on MV4000 system is small in comparison with laser intensity under micro-Raman. This is due to the Raman signal travelling a long way from AFM-TERS integrated system and then being collected by the same objective lens in order to be detected by CCD in micro-Raman, as illustrated in Fig. 3.10. Therefore, a long integration time is required for collecting high-quality Raman spectra [86]. Accordingly, the integration time is increased up to 30 s with ~5 mW of power in order improve the Raman intensity Fig.3.11(a) and 3.11(b) present the contrast of the same laser power with different integration times; this shows that the Raman intensity improves with longer integration times.

Figure 3.10: Illustration of the AFM-TERS system used in this experiment. The red arrow shows the laser's path from the Renishaw Raman spectroscopy to the system and back to Renishaw Raman spectroscopy.

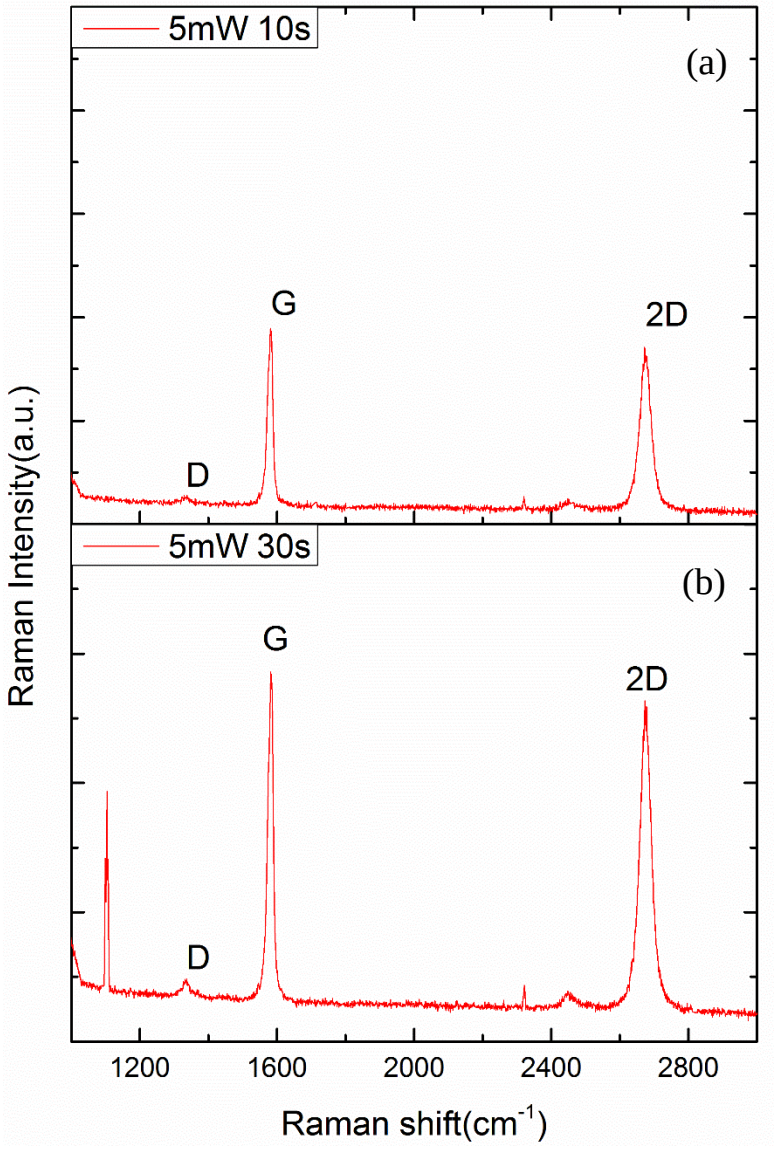

Figure 3.11: Raman spectra of single-layer graphene using the AFM-TERS integrated system with different exposure times. (a) Raman spectrum with 5 mW of laser power and an exposure time of 10 s. (b) Raman spectrum with 5 mW of laser power and an exposure time of 30 s.

By considering the laser power and exposure time the MV4000 system is ready to be used for TERS measurement. Before start TERS scan we have to confirm the TERS enhancement by take TERS spectra at specific point on graphene. For the case of TERS enhancement measurements shown in Fig.3.12 (a), small but some enhancement has been observed. However, even with only the slight change of the tip position, the enhancement signal decreases as shown in Fig.3.12 (b). Therefore, the next and most important test is about positioning the tip with respect to the position of the laser spot. The decrease of enhancement is found to be due to misalignment between the tip position and laser spot as shown in an optical image in Fig.3.13. The enhancement cannot be obtained when the tip position is far away from the laser spot as schematically depicted in Fig.3.14 (a). The small enhancement with high background noise could be observed when the tip is positioned on the centre of the laser spot as shown in Fig.3.14

(b), suggesting the shadow of the tip affects the signal enchantment. Therefore, after many attempts, it has been found that the tip position should be carefully controlled to be located at a specific position on graphene and under laser spot as shown in Fig.3.14(c) in order to reproducible[115].

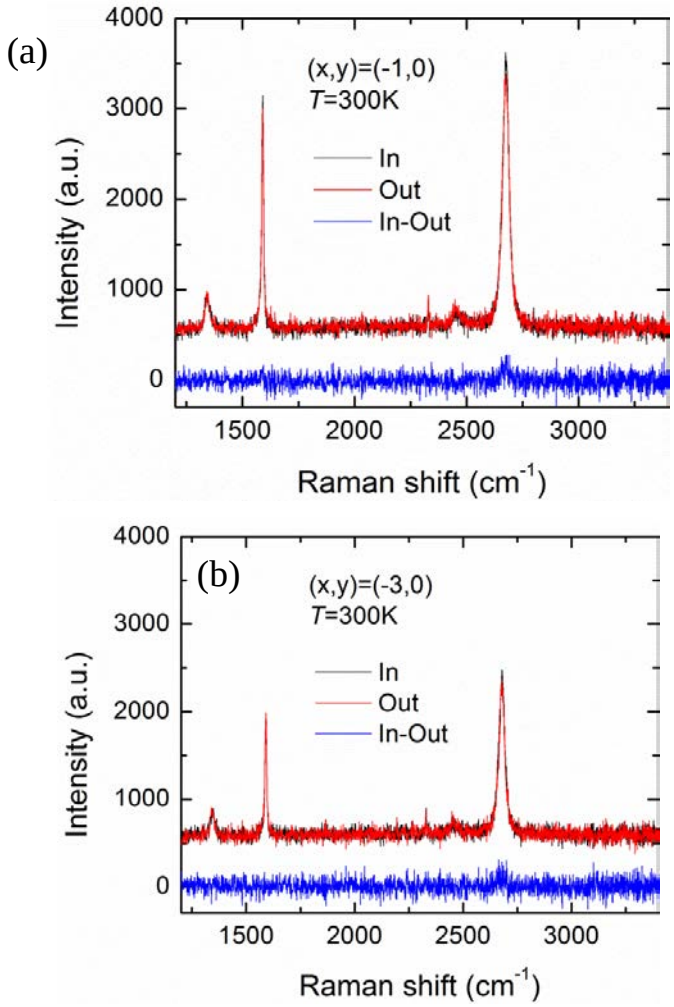

Figure 3.12: MV-4000 system enhancement optimisation the red spectra is presented tip out, the black spectra is presented the tip in, and blue spectra are presented the difference of (tip in-tip out) ;(a) the small enhancement achieve when tip on the laser. (b) No enhancement achieve tip far away from laser spot.

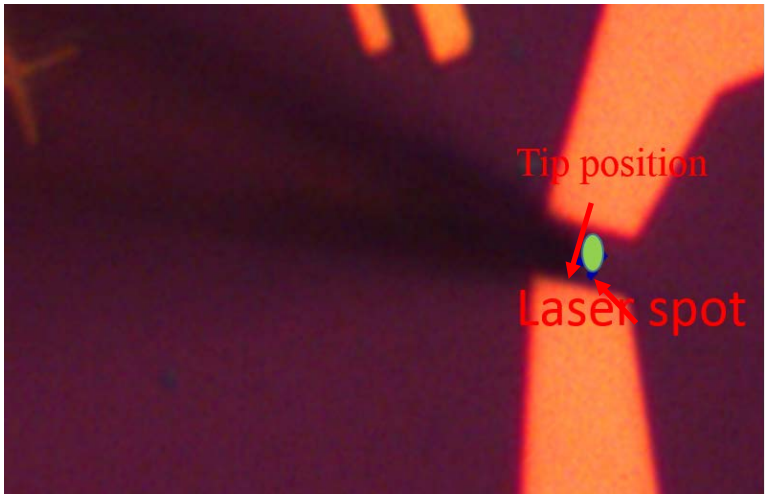

Figure 3.13: The optical image of the green spot is representing laser and tip position in the laser spot.

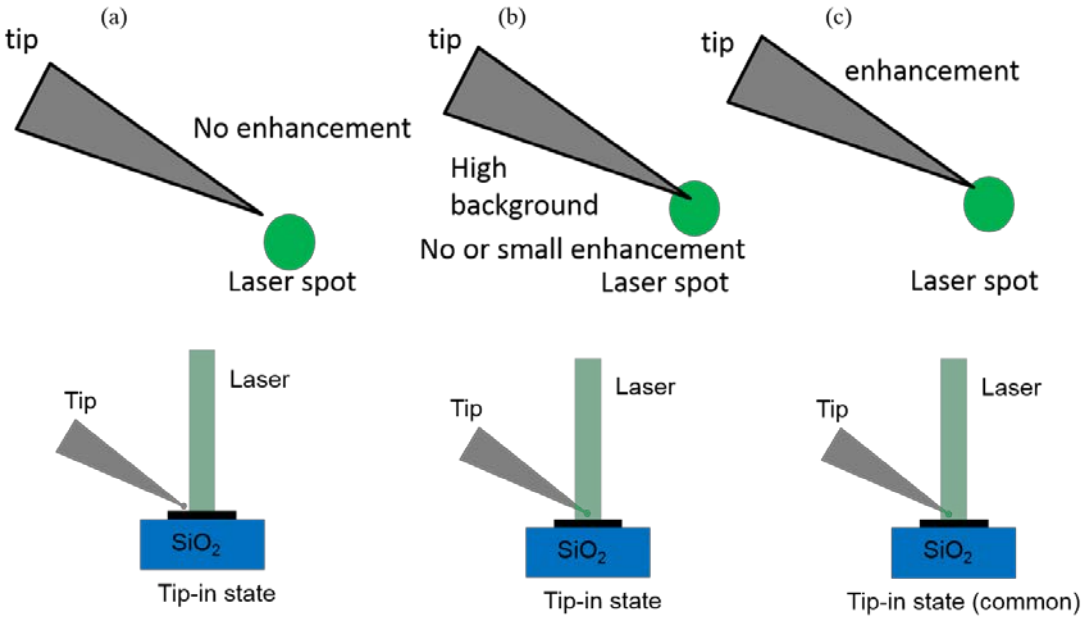

Figure 3.14: Tip state position –laser spot ;(a)the tip far away from laser spot no enchantment .(b)the tip position in centre of the laser spot small enchantment .(c) Tip position on the edge of laser spot for high enchantment and spatial resolution.

After careful optimisation of the laser power, integration time, and tip positioning procedure, eventually, the system has been well stabilised to obtain a good reproducible level of the signal enhancement. Figure 3.15(a) shows the spectra with the tip contacted, with the tip retracted, and the subtracted TERS. Clear TERS signal enhancement has been confirmed for the data of CVD graphene sample. Figure 3.15 (b) shows the spectra with the tip contacted, with the tip retracted, and the subtracted TERS. Clear TERS signal enhancement

has been confirmed for the data of a helium-ion-irradiated sample. Details about the irradiated samples will be discussed late in Chapter 6.

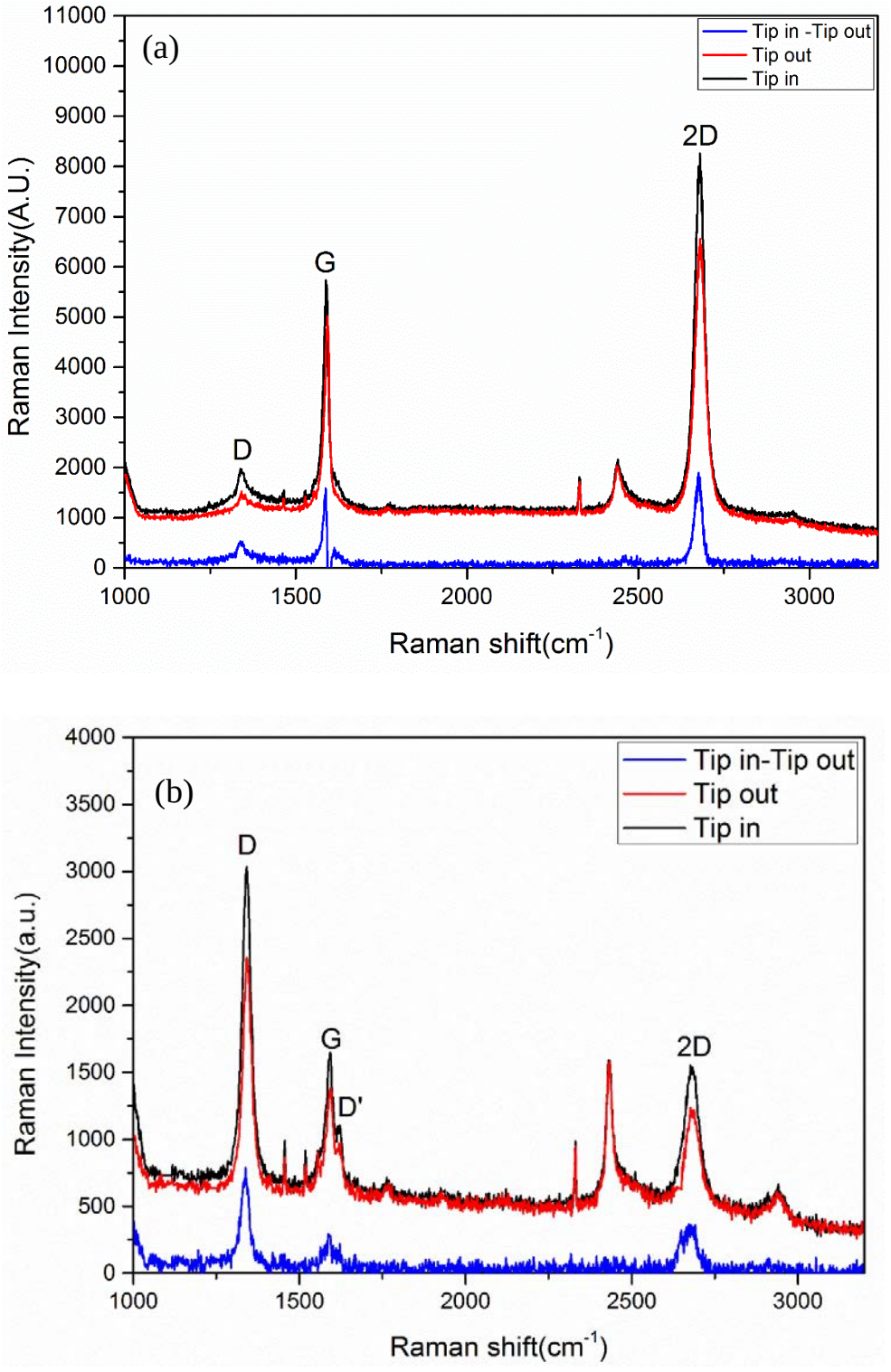

Figure 3.15: (a) TERS spectra with enhancement, the tip in the black spectra, the red spectra is a tip in, and the blue is difference (tip in- tip out) of CVD graphene sample. (b) TERS spectra with enhancement, the tip of the black spectra, the red spectra is a tip in, and the blue is difference (tip in- tip out) of a helium-ion-irradiated sample.

3.6 Conclusions

In this chapter, the main instrument used in this study, Tip-enhanced Raman Spectroscopy (TERS) has been detailed. After explaining the basic principles of TERS, the details of the tool used in this study, Nanonics MV4000 are described. As the TERS is a relatively new technique, test measurements have been conducted by using standard monolayer graphene samples. Testing and parameter optimisation procedures has been detailed. After many attempts, eventually the stable measurement environment have been achieved for further nanodevice investigate.

Chapter 4: **TERS for Suspended Graphene on SiNWs Array**

4.1 Introduction

Nanoscale suspended graphene could be one of the key components for graphene nanoelectromechanical (NEM) devices to be applied for low power NEM switches and highly sensitive NEM sensors. In addition to developing fabrication methods of graphene NEM structures, to establish appropriate nanoscale characterisation methods of their structural properties is very important for further advancement of graphene device applications. In this chapter, Tip-enhanced Raman Spectroscopy (TERS) described in the previous chapter is applied for characterising suspended graphene. First, topographic images of suspended graphene on silicon nanowire (SiNW) array are obtained using atomic force microscopy (AFM). The AFM images are used to identify whether graphene is suspended between the gaps of the SiNW array. TERS measurement results of suspended graphene on SiNWs using a tip with Au nanoparticle sizes of 500 nm will be presented.

4.2 Experimental

4.2.1 Sample Preparation

Figure 4.1 shows a schematic fabrication process of suspended graphene on Si array structure, and the main purpose of this process is to create an integrated metal-oxide-semiconductor field effect transistor MOS devices. Whereas, silicon in this process is used as dope and the graphene is used as the channel materials. Nanowire structure was fabricated on Si with a small gap between nanowire in order to avoid the capillary force by considering 200nm wide and 200nm gap separating between each nanowire. This structure was fabricated as follows. An n-type silicon wafer was used and cleaned using RCA1 and RCA2 a standard cleaning method. Wet oxidation was used at 1000^{o}C for 57 min to grow 295 nm of SiO_2. In order to deposit 60 nm of amorphous Si on top of the SiO_2, the plasma enhanced chemical vapour deposition (PECVD) method was used with a deposition rate of 0.26 nm/sec using 50sccm or Silane (SiH_4) and Hydrogen gas at chamber pressure of 350mT and temperature of 250^{o}C. The wafer was diced into 30 mm × 40 mm samples. In order to

produce etching chip alignment marks with a dimension of 1μm width and 100 μm length using I-line photolithography, the AZ9260 photoresist was spun over, followed by soft bake for 120s at 110ºC.This alignment mark is used to define the position of SiNWs on chips. After the photolithography, the sample was developed in AZ726 for 4 min. Reactive Ion Etching (RIE) was used to dry etch the amorphous Si layer with the gas flow rate of 36 sccm for O_2, and 36 sccm for SF_6, with the RF power of 100 W, and with the pressure of 50 mTorr. An acetone bath was used to remove AZ9260 from the sample. This was followed by the RCA1 and RCA2 cleaning for 10 min at 45 ºC, and 60 by dipping in 20:1 Buffered Hydrogen Fluoride (BHF) for 2 min. *Hydrogen silsesquioxane* (HSQ) negative resist was spin-coated over the sample, and then the sample was soft baked for about 4 min at 80 ºC. This resist is used because it has high resolution electron sensitive and capable of producing a narrow feature of materials and define edge of SiNWs. The e-beam lithography was used for patterning the Si NW array. After e-beam exposure, the sample was developed and hard baked for 4.5 min at 250 ºC. Then, dry-etched using RIE with 36 sccm O_2, 36 sccm SF_6, 100 W of RF power, and 50 mTorr pressure was used to form the nanowires from amorphous Si. The HSQ is then stripped using 20:1 BHF. In order to produce the metal pad contact using photolithography, the negative resist AZ2070 was spin-coated over the sample, followed by a soft bake for 120 s at 110 ºC. The photomask was then used in photolithography, and then sample was baked with the exposure for 60 s at 110 ºC. The negative resist was developed using AZ726 for 3 min. E-beam evaporation was used to deposit a 500-nm-thick Al metal pad contact. Lastly, *N-Methyl-2-pyrrolidone* (NMP) was used to lift off overnight.

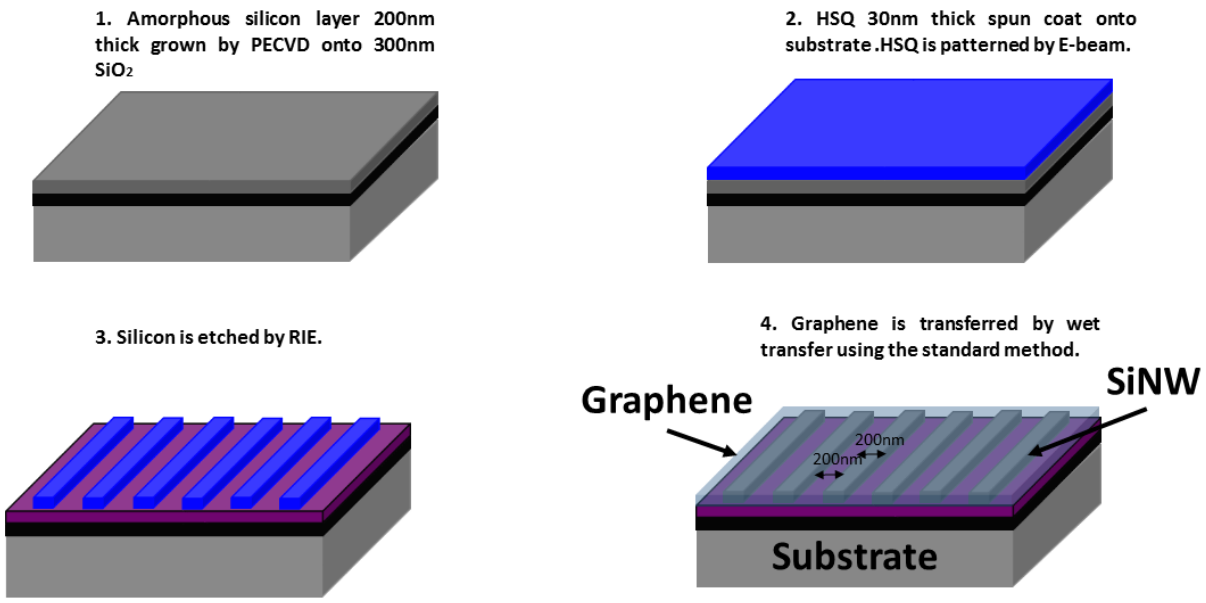

Figure 4.1: Schematic of the fabrication process flow of suspended graphene sample on amorphous SiNW.

After that CVD-grown graphene and transferred on top of the Si NW array "transfer-last" process was obtained by my colleagues Kevin Huang from Optoelectronics Research Centre and Jamie Dean Reynolds from Nano-group as follows as Figure 4.2 is shown. Gently foil of graphene copper was placed on the glass wafer, and then the second glass wafer is pressed down on the foil to smooth the graphene and remove any wrinkles with avoiding any extra pressure into copper. The Kapton tape is used to fold the corners down. Then using the spinner to spin mixer of 5% Polyvinyl butyral (PVB) and Ethanol on to graphene on copper with 500rmp spread and then 2000 rmp thin for ~500 nm thick for 2 min at 75°C. The unwanted layer of graphene which is grown on the backside of copper is etched using RIE recipe of 20W 100mT 80sccm Ar 20sccm O_2.The large graphene /copper is cut into the sample size, and then etch copper foil from copper/graphene/PVB load in 0.5M Ammonium Persulphate surface for ~ 4 hours. With a lot of attention, graphene/PVB is picked up replace into the tray and rinse in DI water and keep floating all the time in order to avoid the graphene stick into the tray edges. This process should be repeated many times until confirm the water is clean from any chemical and leave the graphene/PVB for 2 minutes. To remove any metal residue left on the graphene, graphene/PVB is transferred into 30% of HCL for 1 minute. Then, replace the acid with DI water, and graphene/PVB is left in DI water for 5 minutes. Dip substrate (SiNW array) in water underneath at an angle and handle graphene/PVB from the folded piece into substrate and sticks the tap down in order to stop graphene from moving. Graphene/substrate left from the water with an angle in order to speed the drying process and leave it to dry for 5-10 minutes no more this in order to avoid the reflowing of PVB

resist. Hotplate is used with temperature 65°C for 3-5 minutes in order to remove the water and reflow PVB thus decrease the wrinkles and cracks on the graphene. Leave it to cool down for 5 minutes. Finally, remove the PVB from graphene by dipped in Ethanol for an hour.

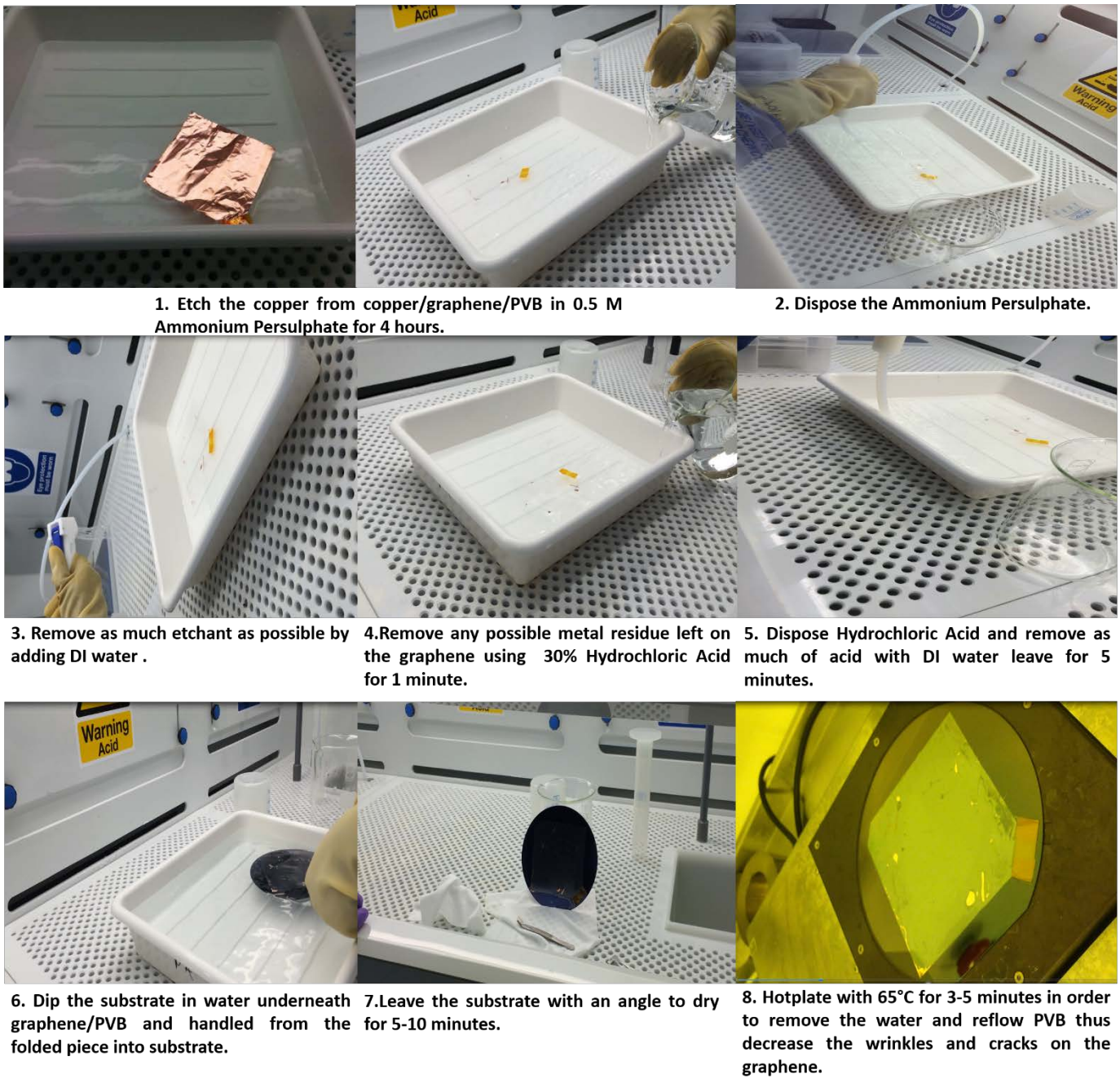

Figure 4.2: Graphene transfer process.

4.3 Micro-Raman Measurements

Suspended graphene sample of 30 mm × 40 mm was diced into a 1cm ×1cm SiNW array, and micro Raman spectroscopy characterised this. An optical image of the sample is shown

in Fig.4.3. (a). Fig.4.3.(b) shows Raman spectra of a suspended graphene on SiNW array with the Raman shift range from 100 to 3000 $cm^{-1}$where main features from graphene are included. The 2D peak or G' peak appears around 2675 cm^{-1} and this peak is a second order process of graphene including two iTO phonons near the K point[121]. The 2D peak is useful to identify the number of layers by its shape, width, and position and its position depends on the laser excitation [124]. The G peak appears at 1583 cm^{-1}which is originated from E_{2g} (iTO and LO) with a tangential shear mode that is common to graphene forms where carbon atoms exhibits sp^2 hybridization. The intensity ratio of the 2D peak to the G peak I_{2D}/I_G is used to identify the number of graphene layers, and it is ~1.7 extracted from this data. For single layer graphene, the intensity of the 2D peak is four times as that of the G peak. In graphite 2D peak components two $2D_1$and $2D_2$, and the height of this peak is ¼ and ½ to height of G peak[125]. The full-width half maxima (FWHM) estimated by using curve fitting of the 2D peak is about 40 cm^{-1}. The third peak is the disorder-induced D peak which is around 1334 cm^{-1} and this peak is a first order of the 2D peak. However, the D peak depends on the disorder and does not depend on the number of layers in contrast to the 2D peak and this peak is due to the A_{1g} mode. The ratio of the D peak to the G peak intensity I_D/I_G is used to identify the nature and amount of defect in the graphene layer, and it is about 0.84 extracted from this data. From intensity ratio I_{2D}/I_G and I_D/I_G which suggest that graphene on SiNWs is defective.

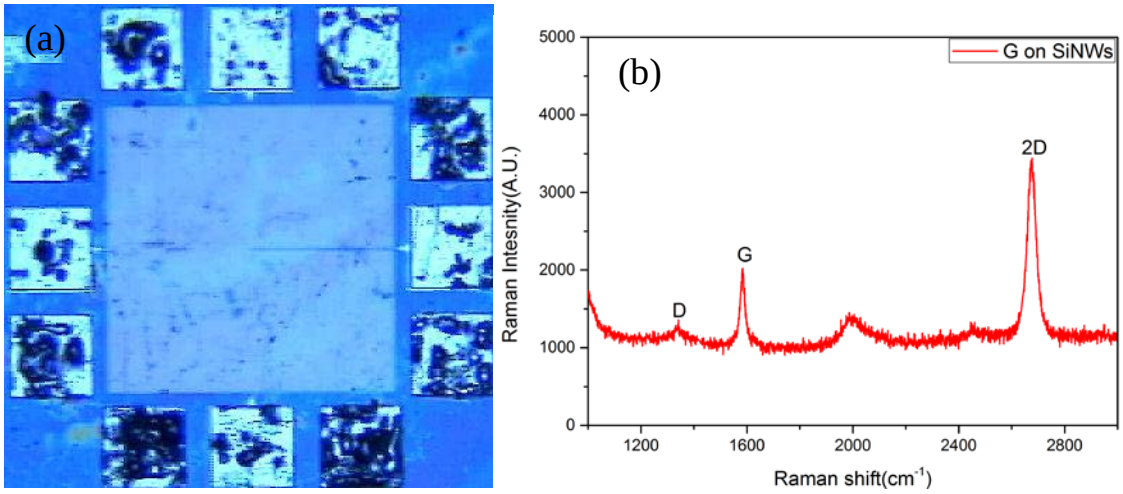

Figure 4.3:(a) Optical image of suspended graphene on SiNW substrate; (b) Raman spectra of suspended graphene on SiNW substrate showing the main feature of graphene 2D, G,and D bands with laser excitation 2.33eV.

4.4 AFM image of graphene on SiNWs array structure

The Multimode Nanoscope AFM instrument from Veeco is used in this study for AFM measurement. The tapping mode with the intermittent contact is used. This mode is used in AFM scanning to avoid damaging the tip and samples during measurements [126]. The radius of the sharp silicon tip is around 10 nm with force constant of 10-130N/m and the resonance frequency range of between 204 and 497 kHz. The measurement is conducted at room temperature. The AFM is used to obtain a topographic image of the suspended graphene on SiNW array and to compare later with the result of the AFM-TERS measurement instrument. Figure 4.4presents an AFM topography image of the graphene on SiNW array with the scan area size of 20×20 μm^2. Some area is covered by the residue of the soft materials (PMMA) which were used to transfer graphene onto the SiNW array, while the figure clearly shows the periodic structure originated from the SiNW array underneath the graphene.

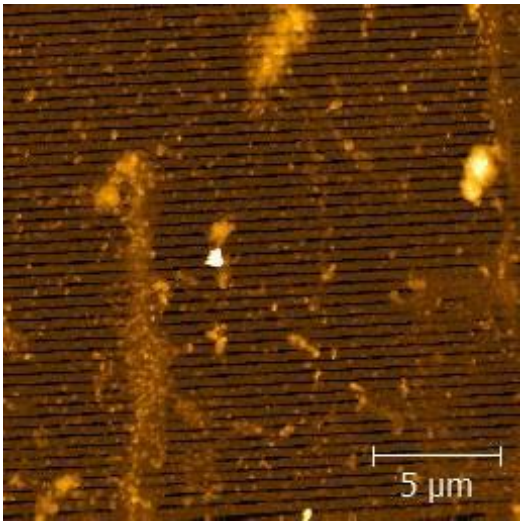

Figure 4.4: AFM height topographic image of suspended graphene on SiNW with the scan area size of 20×20 μm^2.

However, AFM topographic image of SiNW array without graphene results with the scan area size of 12×12 μm^2 are shown in Fig. 4.5 (a).Where from this topography is showing clearly the structure and gaps between SiNW arrays before transfer graphene on top. Figure 4.5. (b) Present the height profile line across the SiNWs array, and we found that the step height between the top of SiNWs and depth of the gap ~200nm which suggest that the gap is clear from the materials.

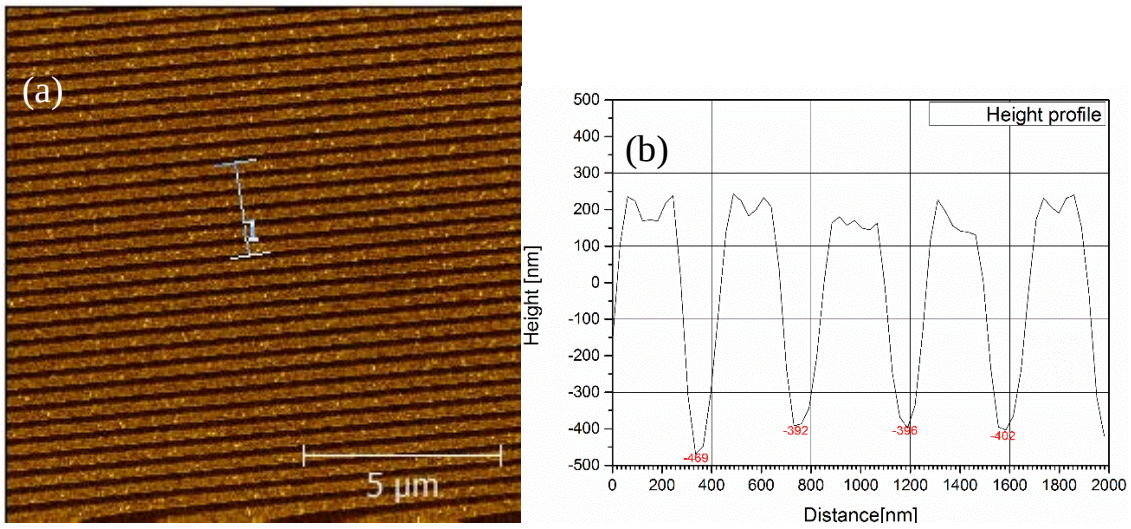

Figure 4.5: a) AFM topographic image of SiNW with the scan area size of 12×12 µm^2.(b) is corresponding height profiles of the line in (a).

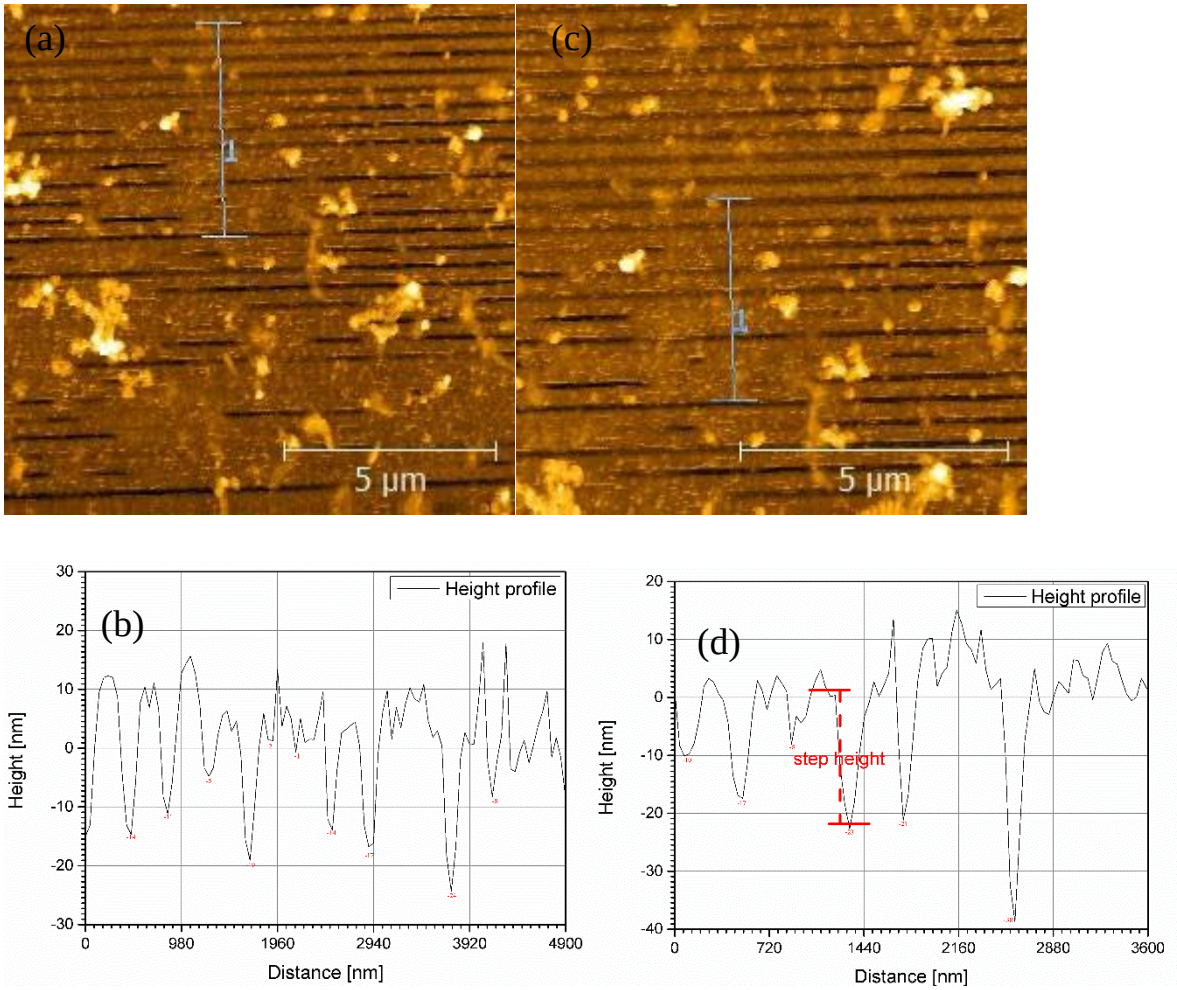

Figure 4.6: a) and c) AFM topographic image of suspended graphene on SiNWs with the scan area of 9×9 µm^2. This area is mostly covered by graphene over SiNWs, and the graphene has some defects. b) and d) are corresponding height profiles of the line in (a), and (c).

Furthermore, the results of the AFM topographic image of suspended graphene on the SiNW array with the scan area size of 9×9 μm^2 are shown in Fig. 4.6. First, we clearly notice that graphene is suspended on the gaps between the Si NWs. Also, in this figure, some gaps in between nanowires are seen, and these gaps are due to either graphene being bending or no graphene being in this area. Figure 4.6. (b) and (d) present the height profile along the lines shown in Fig. 4.6. (a) and (c), respectively. From these profiles, we have found that the step height on the gap is in the range of 10-28 nm, suggesting that there is suspended graphene or bending on the gap. The step height as shown in Fig.4.6 (d) between two steps are the highest point which corresponds for graphene on top of the SiNWs and the lower point which corresponds of height of graphene on top of gap.

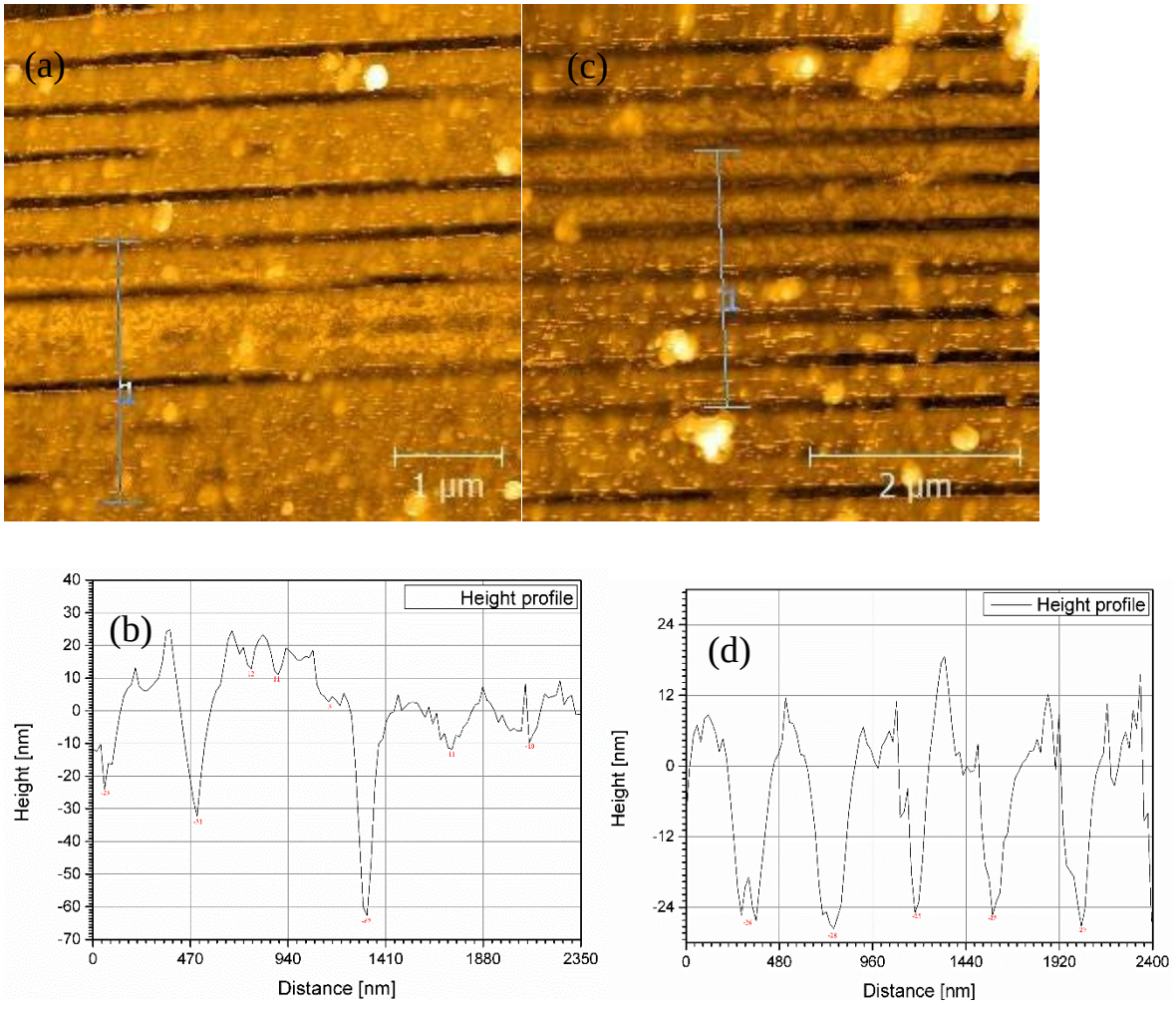

Figure 4.7: a) and c) AFM topographic images of the suspended graphene on SiNW with the scan are of 5×5μm^2 and mostly this area is covered by graphene over SiNWs. b) and d) are corresponding height profile of the lines in (a)and (b).

To investigate more in detail, AFM topography images with the scan area size of 5×5 μm^2 of this sample is presented in Fig. 4.7(a) and (c). The area covered by the suspended graphene

over the gaps between the SiNWs is again clearly identified. On the other hand, some gaps in between the SiNWs array can be noticed. This can be due to graphene being bending or defective. Figure 4.7(b) and (d) present the height profile along the lines in Fig. 4.7(a) and (c), respectively, and from this profile, the area which is not covered by graphene or the softened area shows a larger step height ~60 nm than the result from the area covered by suspended graphene, typically about 2-15 nm. The above AFM images has been taken in different area on graphene in order to investigate the coverage of graphene. In the following AFM-Raman and TERS study, we will consider these areas in order to investigate effects of suspension of the graphene such as strain and defect formation. The graphene was transfer into SiNWs using last transfer process which wet process .when dry up the water tended to stack to surface of structure in between the channel as shown in Figure4.8 (a). Then, the water start to dry up from channel as shown in Figure 4.8 (b) .As a result, the capillary force acted on the suspended graphene due to drying process ,and the suspended graphene start to bending in between the SiNWs gaps or break in order to produce defect as Figure 4.8(c) shows .

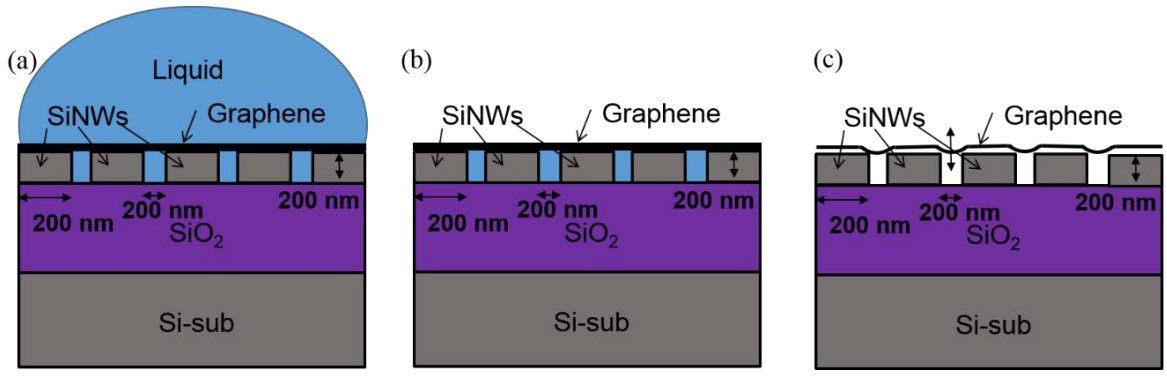

Figure 4.8: Diagram show suspended graphene on SiNWs a)the water remain on top of the surface of the structure.(b) the dry up water from the channel of SiNWs.(c)the graphene bending after the water dry up.

4.5 TERS

A Nanonics Multiview MV4000 integrated with a Renishaw inVia Raman spectrometer was used for TERS measurements. A schematic setup of TERS is shown in Fig.4.9 (a). A top-illumination configuration is used in this system, and this means the laser is exposed to a sample from the top with an objective lens (50x magnification, NA=0.45).The same objective lens collects the Raman scattered light. The wavelength λ of 532 nm of the Nd-doped Y-Al-garnet laser was used for excitation. A commercial probe tip with a Quartz

tuning fork (Nanonics Imaging Ltd.) was used for this experiment. The tip was coated with Au nanoparticle on top and the size of this nanoparticle is about 500 nm diameter. The laser power used in this measurement was 5 mW. The laser spot and tip position was aligned manually. The tip height (z) was controlled by the tuning fork feedback and the sample on the stage in–plan (x, y) position was controlled by the piezo stage driver. Taking a TERS spectrum at a certain position two spectra with tip approached (tip in contact) and tip retracted (tip not contact) are taken. The distance between the tip and sample is ~10 μm when the tip is retracted. The spectra taken with the tip approached including both near-field and far-field signals, whereas the spectra with the tip retracted have only the far-field contribution. The near-field effect obtained by subtracting the tip-retracted spectrum from the tip-approached one. Figure 4.9 (b) exhibits tip-approached and retracted spectra for same point at specific position on the suspended monolayer graphene. The enhancement of each peak has been confirmed in the subtracted spectrum shown in Fig.4.9 (b). For the Raman spectra, important peaks are at 520, 1348, 1582, and 2689 cm^{-1}, corresponding for the Si substrate and, defect-induced D peak, graphene G peak, and 2D peak from the honeycomb carbon lattice in graphene. From the TERS result, the Si peak, G peak and D peak intensity has been enhancement, but the 2D peak intensity is quite weak or small, suggesting that the enhancement depends on individual peaks [101].Also, as presented in section 4.4 2D intensity is small because graphene is defective .As result ,it is not strange to have small enhancement of 2D peak.

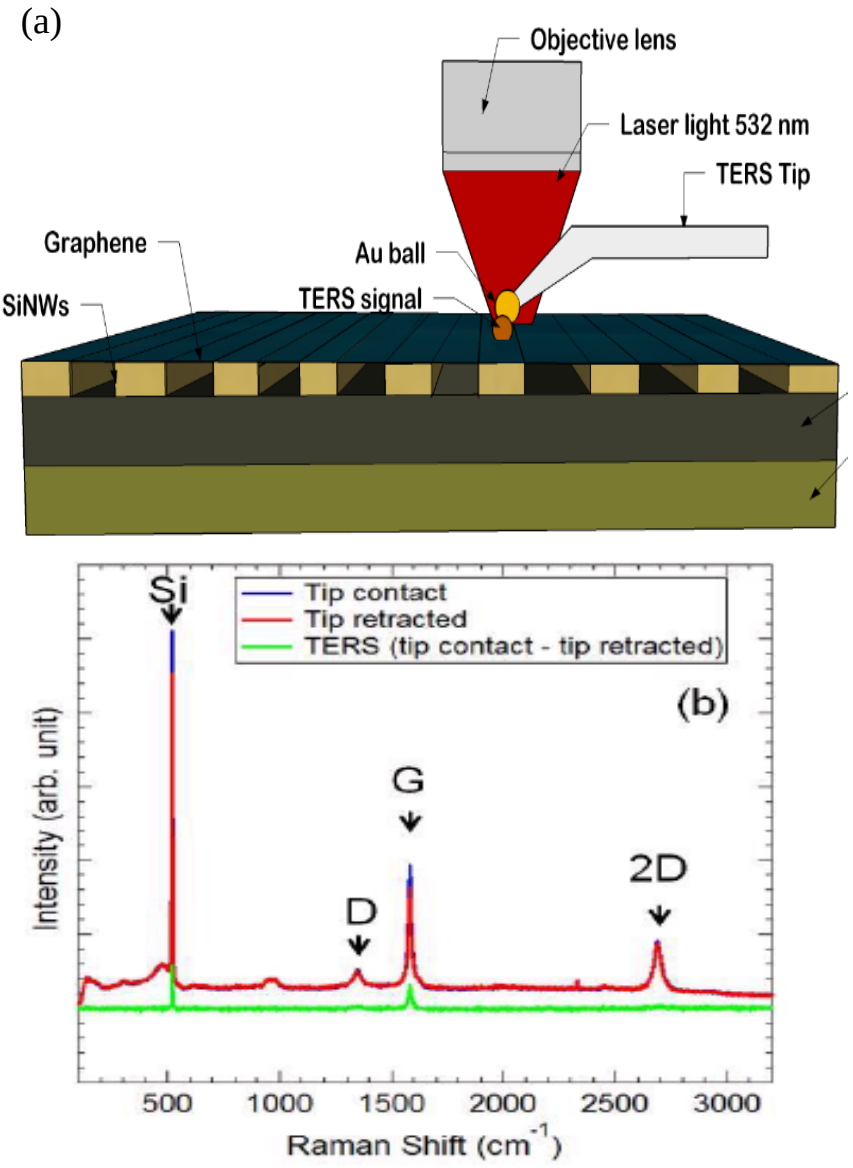

Figure 4.9: (a) A schematic diagram of a suspended graphene sample and the TERS measurement. (b) Raman spectra of specific position point on suspended graphene taken in TERS measurements.

4.6 Results and discussion

A HIM image and AFM image of the sample for same region are presented in Fig. 4.10(a) and 4.10(b). These images clearly show that the graphene on the gap between the nanowires is suspended. In Fig.4.10(c), an AFM profile along the line in Fig. 4.10(b), and the step height between the graphene on the wire and on the gap is about 23-28 nm.

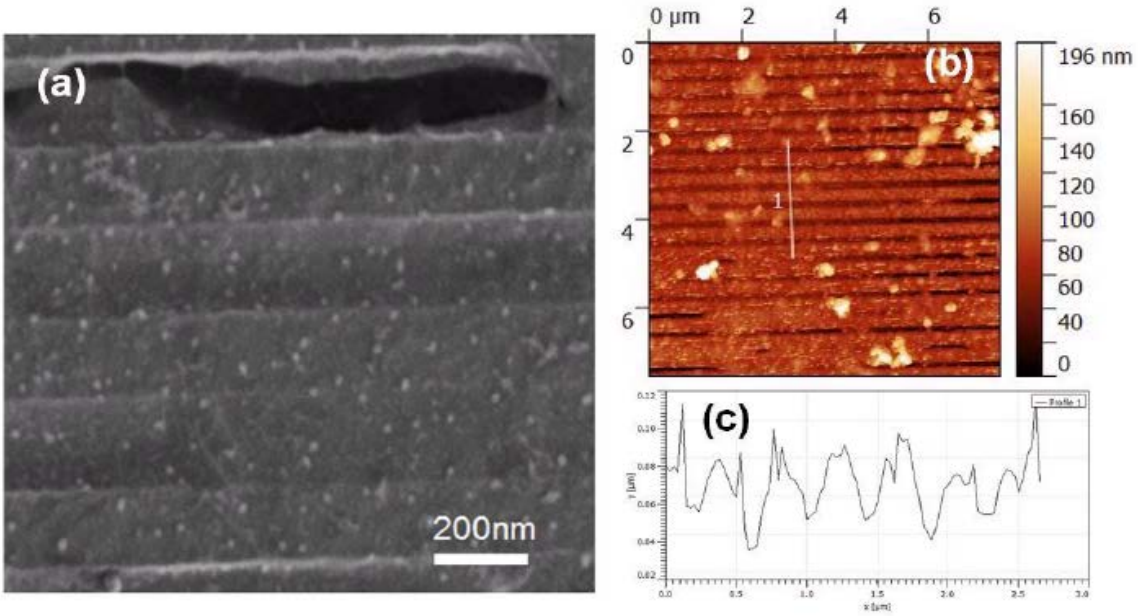

Figure 4.10: a) A He ion microscopy (HIM) image and (b) AFM topography image of the suspended graphene structure. (c) A height profile along the line shown in the AFM topography image in (b). TERS spectra were taken in along the line.

In Fig. 4.11(a), an AFM image of the suspended graphene taken by using the TERS tip of AFM-TERS integrated system is shown with the scan area size of $5 \times 5\ \mu m^2$. A set of Raman spectra with the tip contacted and with the tip retracted and spatial resolution of 1.44µm, and TERS spectra are shown in Fig.4.11(b) and 4.11(c), respectively. The spectra were taken along the white line in the AFM image in Fig.4.11 (a) from the point A to B by every 50 nm step. The difference ((tip-approach) – (tip-retract)) of the TERS spectra has been observed particularly for the D peak around 1348 cm^{-1}.On the other hand, the Raman spectra without the tip contacted do not show any significant changes from the point A to point B as shown in Fig.4.11(b). This is due to the spatial resolution which is 1.44µm.

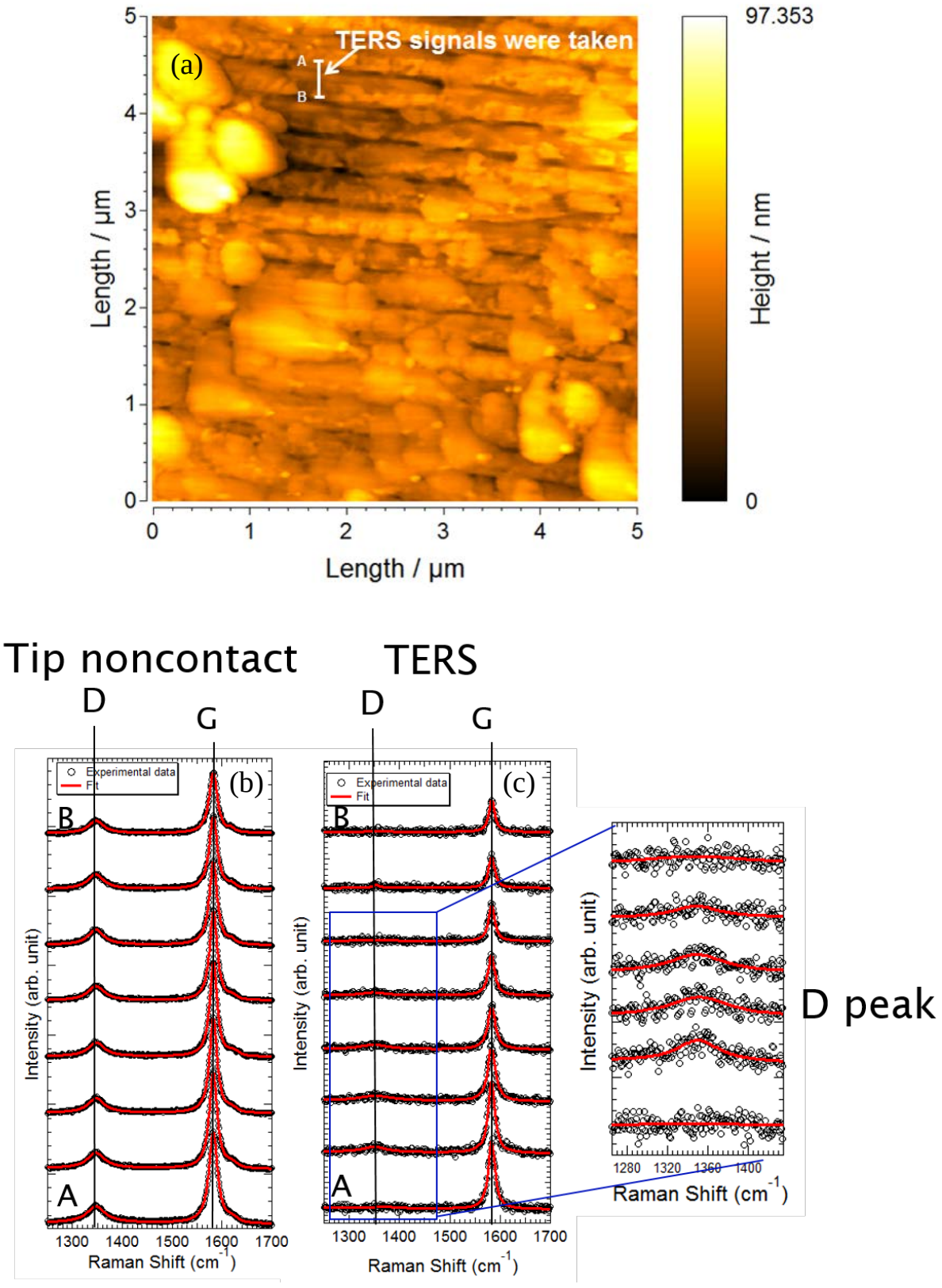

Figure 4.11: (a) AFM topography image with the scan area size of 5×5 μm^2 for the suspended graphene on SiNWs using AFM-TERS integrated system. (b) Raman signals without tip. (c) TERS spectra.

The spectra with the tip retracted and TERS results in Fig.4.11. (b) and (c) are analysed. Figure 4.12 and 4.13 (a) show the peak position of the D and G peaks along the scan line.

The spectra of the tip retracted do not show any remarkable changes of the position of D and G peaks are 1347±2 cm^{-1} and 1582±1 cm^{-1}, while in the TERS spectra, the D peak appear and disappear at 250 nm with respect to the position on the graphene and position of the D and G peaks is shifted. These results might becaused by the chemical and mechanical interaction between graphene and the SiNWs beneath. Figure 4.13(b) shows the ratio between the intensity of the D peak (I_D) and that of the G peak (I_G) for the points 1 to 8. The intensity ratio I_D/I_G is used for estimating the quality of graphene [75]. Figure 4.13(b) does not show any changes the spectra take with tip retracted for the points 1 to 8, while a change is observed in I_D/I_G of the TERS spectra. The changes are localised in the middle of the scanned trace of the points 2 to 5. This result shows that the D peak increases at certain points which might correspond to the edge of the SiNWs. The aforementioned observations support the hypothesis that the defects are perhaps prompted at the edge of the SiNWs as a result of the interaction between graphene and the SiNWs after the transfer process.

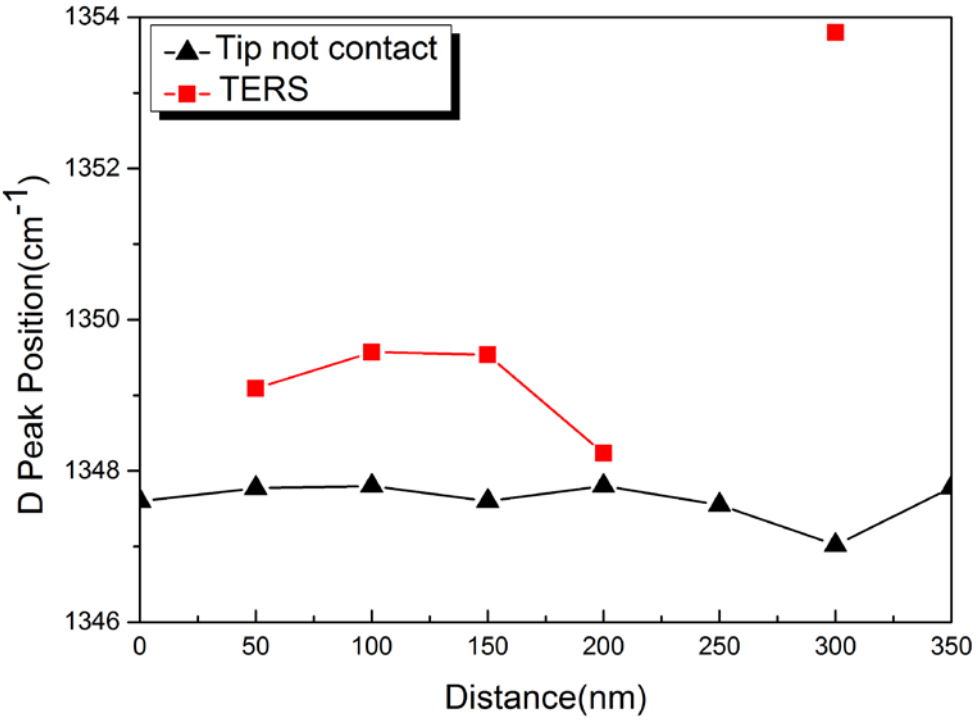

Figure 4.12: D peak position of TERS spectra and tip not contact.

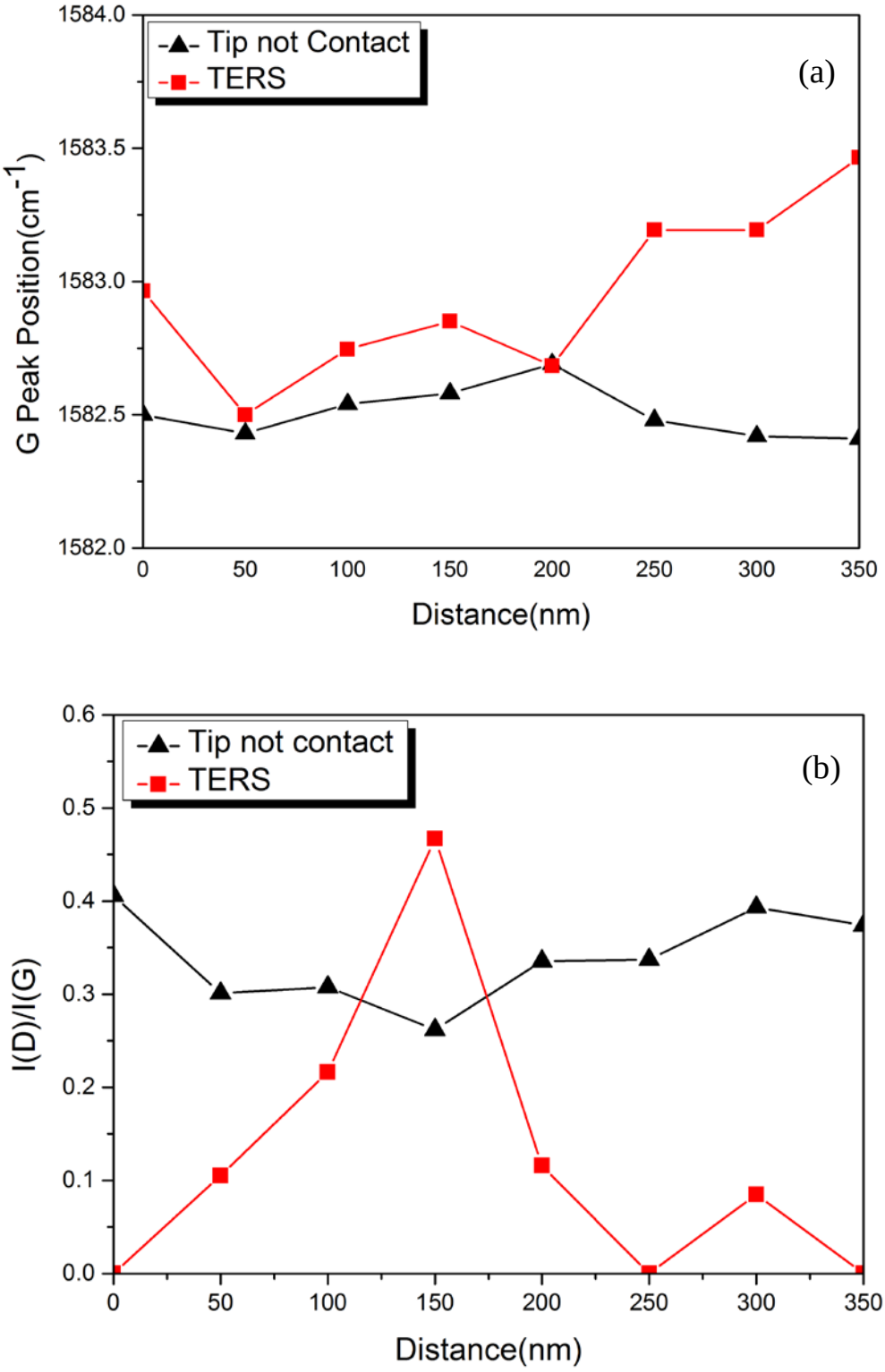

Figure 4.13:(a) G peak position, and(b) I_D /I_G intensity ratio of each spectrum are extracted from the spectra with tip retracted and TERS spectra shown in Figure 4.11 (b) and (c) and plotted as a function of the points where the spectra were taken.

4.7 Conclusions

The suspended graphene structure has been fabricated by using the “transfer-last” process and characterised by using AFM and TERS. The detailed analysis of the AFM topography images of the suspended graphene on the SiNW array suggests that the graphene is suspended on the gap between the Si NWs. This was followed by the AFM-Raman and TERS measurements where clear signal enhancement after approaching the tip has been obtained. Finally, the TERS measurement of the suspended graphene on the SiNW array has been carefully conducted using the Au coated tip with 500 nm in order to investigate what has happened to graphene after the transfer. While the Raman spectra taken without the tip have not shown any significant shifts and changes, the TERS spectra exhibited a shift of the D peak and G peak positions at the point where the graphene might be located at the edge of the SiNW underneath. When the intensity ratio I_D/I_G was examined, possible evidence of defects localisation has been observed. As the spatial period of this localisation is about 200 nm which is consistent with the period of the Si nanowire array arrangement, the results suggest that the defects or strain are induced to the suspended part of graphene after the transfer of graphene. These results further confirm that 100 nm spatial resolution is achievable with TERS measurements which can contribute to further advancement of fabrication of graphene-based nanoelectromechanical devices.

Chapter 5: **TERS for irradiated Graphene**

5.1 Introduction

In particular for micro- and nanoscale devices applications, how to control defects in graphene and how to observe the effects of defects are one of the most important issues to understand the mechanism behind device operation and to gain more flexibility in designing device structures [12, 127].While oxygen plasma, ion bombardment and focused ion beam (FIB) have been employed to introduce defect [12, 127, 128], helium ion irradiation or Helium Ion Microscope (HIM) is an attractive method because of excellent spatial resolution and position controllability. The effects of He ion irradiation on graphene have been investigated via Raman spectroscopy[79] and transport properties[32].

However, to study the edge and boundary between the irradiated and non-irradiated regions, advanced tools with higher spatial resolution would be useful. In this work, we have applied Tip-Enhanced Raman Spectroscopy (TERS) to He-ion-irradiated graphene for the first time to study effects of irradiation in details, in particular focusing on the boundary of the irradiated regions.

In this chapter, the fabrication process for graphene nanoribbon (GNR) devices is described in detail. The details of He ion irradiation on graphene devices are presented. Then we show the results of investigation of induced defects by using micro Raman and Tip-enhanced Raman spectroscopy across the graphene edges and across the boundary between ion-irradiated and non-irradiated regions.

5.2 He-ion irradiation

Helium-Ion Microscopy (HIM) was introduced by Carl Zeiss in 2007 for nanotechnology, as shown in Fig. 5.1(a) [23-26, 129, 130]. The HIM image is generated from the secondary electron (SE) emission by a focused beam of helium ions scanning across a surface. The HIM incorporates a bright illumination source, which offers exceptional spatial resolution versus electronic microscopes [131, 132]. Figure 5.1(b) shows the HIM structure. The sharp needle (tip) in the HIM source region is held in high vacuum and cryogenic temperatures, and an extremely intense electric field is produced at its apex. With this equipment, field strengths of 5 V/Å can be reached with modest voltages in the range of 5–30 keV [133]. Any neutral gas atoms near the vicinity of the tip are ionised at a field strength of 3 V/Å, and the ionization assumes the shape of a disk shape. The resulting positive helium ions are then immediately accelerated away from the needle. The ALIS Company produces the ion source, which is an atomically sharp pyramidal shaped tungsten tip. Figure 5.1(c) shows the trimer (i.e., 3 He^+ atoms) and the emission pattern of the ion source. This geometry has the advantage that field ionization takes place predominantly at the topmost few atoms due to the electric field being concentrated at the apex of the pyramid [23, 129, 130, 133, 134]. The emission from a single atom is selected using an aperture under typical operating conditions. The beam current is 1–5 pA, although the HIM beam current can range from 1 fA to 100 pA.

The HIM is atomically sharp, and is combined with the larger momentum (and the smaller de Broglie wavelength) of helium ions compared to that of electrons. The HIM is able to scan a sample surface in sub-nanometre scale [26-28]. In the first ~100 nm of entering the substrate, the He ions produce far fewer collision cascades, which causes only a small amount of beam divergence. The SEs are excited and lose energy in the process (i.e., due to electron collisions). As high energy helium ions enter the substrate, they scatter in-elastically. The HIM mass is much larger (7000 times larger) than the electron mass and, in the substrate, they maintain their initial path quasi-perfectly. Eventually, as they decelerate and lose their kinetic energies (measured in eV per angstrom), nuclear collisions (i.e. elastic scattering without SE generation) become the dominating ion interaction method. This results in scattering at increasingly large angles and broadening of the beam interaction volume deep into the substrate [135]. Whereas, the electrons in the vicinity of the e-beam only collide elastically with target atoms due to their small mass, and scatter far easier than helium ions (i.e. much larger interaction volume). High resolution imaging and a small interaction volume lower than 1 nm was achieved by this HIM, but new versions can reach resolutions below 0.35 nm [26-28].

Figure 5.2 shows a comparison of a Si substrate at an acceleration voltage of 30 keV for the He-ion and electron beam, and the beam interaction volume for a Ga-ion beam. This show that the interaction volume of the Ga-ion beam when it enters the substrate is never truly localised, but broadens compared to the He-ion beam, which is far more localised. In comparison to the He-ion and Ga-ion beams, the electrons enter and scatter far more easily due to their small mass and so their interaction radius is much larger. The He-ion beam interaction radius becomes even smaller and its penetration depth increases at higher acceleration voltages [135], but 30-40 keV is the maximum acceleration voltage of recent versions of the tool.

Helium ion microscopy has been introduced as high resolution imaging technology primarily due to its unique contrast mechanisms and imaging capabilities. Moreover, helium ion microscopy has ability to pattern (milling and lithography) and sputter, as does a conventional Ga-ion beam, and this due to the intense focused beam of He-ions created from this tool. This technology is now starting to be used as a patterning tool for fabricating state-of-the-art nano-devices [29-31].

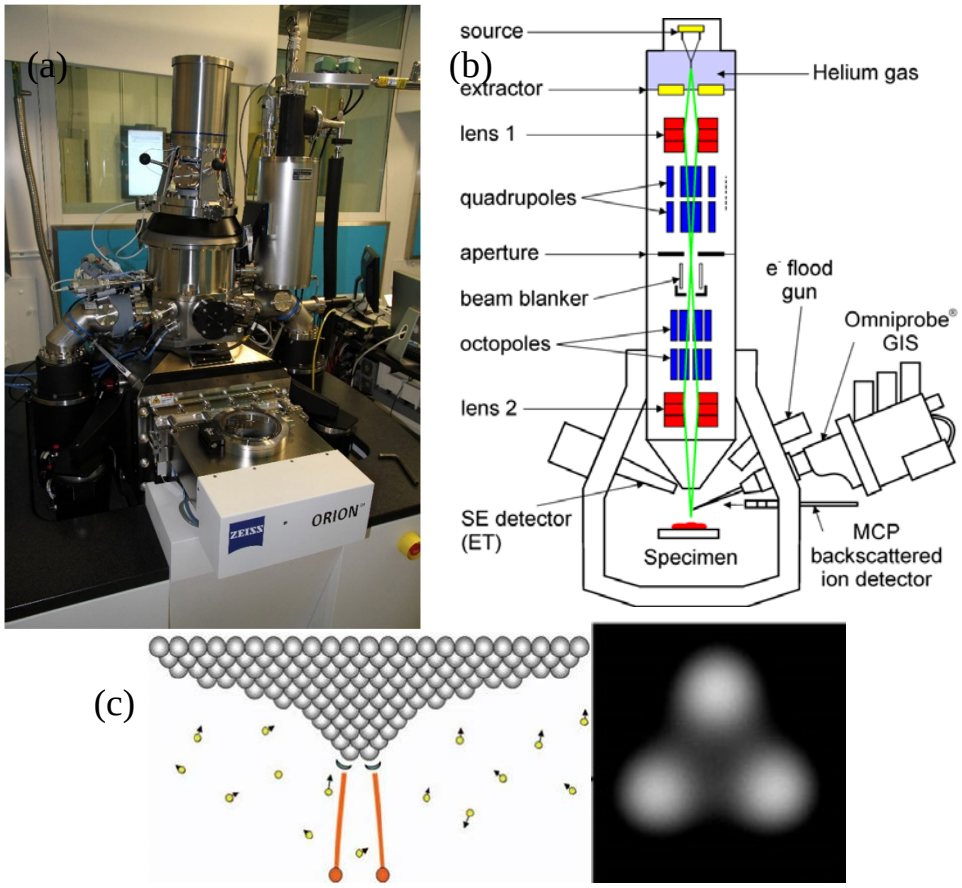

Figure 5.1: (a) Zeiss Orion™ Plus HIM at the University of Southampton. (b) HIM column diagram. (c) HIM atomic structure is showing three atoms of the timer on a tungsten tip.

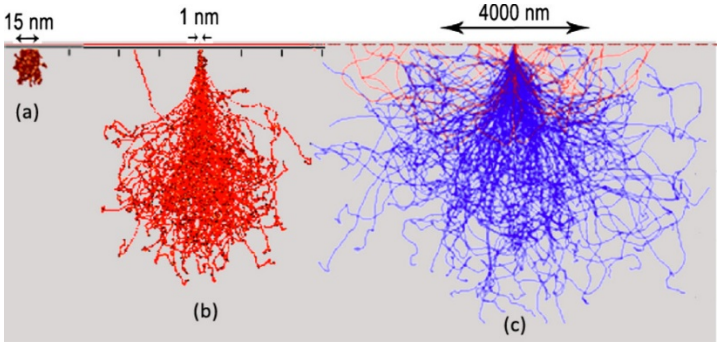

Figure 5.2: Diagram comparing various beam volume interactions on Si substrate: (a) the interaction volume of a Ge-ion beam, (b) He-ion beam interaction, and (c) e-beam with an acceleration voltage of 30 keV.

5.3 Experimental

5.3.1 Sample Preparation

1 cm × 1 cm standard commercial samples of monolayer CVD graphene on p-type doped Si/SiO_2were purchased from Graphene Supermarket[120]. The SiO_2 thickness is 285 nm, and the wafer thickness is 525 μm[120].

An optical image and Raman spectrum of a monolayer CVD graphene are shown in Fig.5.3 (a) and (b), respectively. From Raman peak fitting, the number of graphene layer was identified. Characteristic features of the Raman spectrum for graphene are seen in Fig. 5.3(b). The 2D or G' peak is around 2680 cm^{-1}[121]. If the 2D peak comprises a sharp peak, this indicates the single-layer graphene, while multi-peaks indicate the presence of more than one layer. The optical image in Fig. 5.3(a) and the corresponding spectrum taken by Micro Raman spectroscopy in Fig. 5.3 (b) indicate the presence of CVD graphene cover most of substrate with some defect. The Raman spectrum of graphene has four peaks within the Raman shift range of from 1000 to 3200 cm^{-1} as shown in Fig. 5.3(b). The G peak appears at 1586 cm^{-1}, and this peak is caused by the doubly-degenerated E_{2g} (iTO and LO) with a tangential shear mode that is common to all graphene forms where carbon atoms exhibits sp^2 hybridization. The G peak is especially important because it is sensitive to strain effects in graphene layers. This peak comes from a first-order Raman scattering in graphene. The other important peak for single-layer graphene is the 2D peak mentioned above. The 2D peak does not require the existence of defects to be present in the spectrum [123, 124]. The intensity ratio of the 2D peak and the G peak I_{2D}/I_G is used to identify the number of graphene layers ~2; the intensity ratio from this is data ~1.69, and this due to defect is for single-layer graphene, but in, the 2D peak is twice the G peak. The full width at half maximum (FWHM) using Lorentzian function fitting for the 2D peak is about 30± 0.4 cm^{-1}[124].The peak around 1348 cm^{-1} is called D peak which is a first-order 2D peak. The D peak depends on the disorder, edge geometry, and defect density and does not depend on the number of layers in contrast to the 2D peak. This peak is the result of the A1g mode. The ratio of the intensity of the D peak to that of the G peak I_D/I_G is used to identify the number of a defect in the graphene layer, and it is about 0.85 in this case in Fig. 5.3 (b).

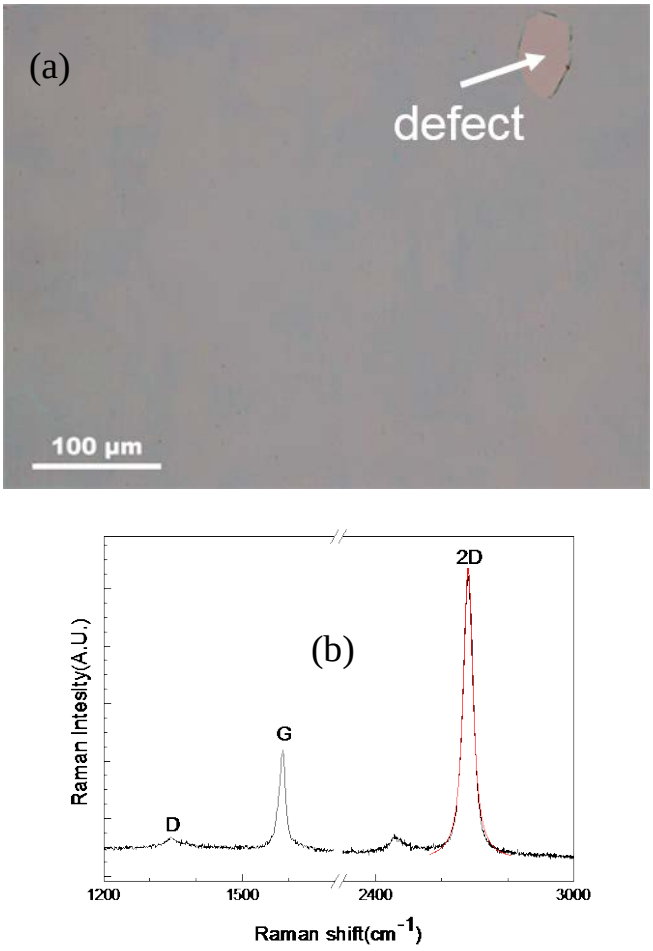

Figure 5.3: (a) The optical image of CVD monolayer graphene used in this study. (b) A Raman spectrum of a single-layer graphene showing the main features of graphene – D, G, and 2D bands. The black line is experimental data, and the red line on 2D is the Lorentzian fitting curve.

The fabrication process of GNR is summarised in Fig. 5.4 (a). For the GNR fabrication, two e-beam lithography steps were used. For the first e-beam lithography, a resist bi-layer of Methyl Methacrylate (MMA 8.5 EL 9)/Poly Methyl Methacrylate (PMMA 495K) was spin-coated. The MMA resist (spin-coated at 1500 rpm) was baked for 70 seconds at 150 °C, and the PMMA resist (spin-coated at 5000 rpm) was baked for 70 seconds at 180 °C. The thickness of 425 nm for MMA resist layer and 125 nm for PMMA resist layer were measured using ellipsometry. The bilayer resist were used in order to create an undercut profile after e-beam exposure. The MMA resist layer at the bottom has higher sensitivity to the e-beam so the undercut is created. The existence of the MMA resist layer has improved the lift-off process, resulting in clear edge definition of the patterns shown in Fig. 5.4(b) and (c). A state-of-the-art JEOL 9300FS e-beam lithography system was used to expose with a dose of 300 $\mu C/cm^2$, and the e-beam scan was operated at an acceleration voltage of 100 keV.

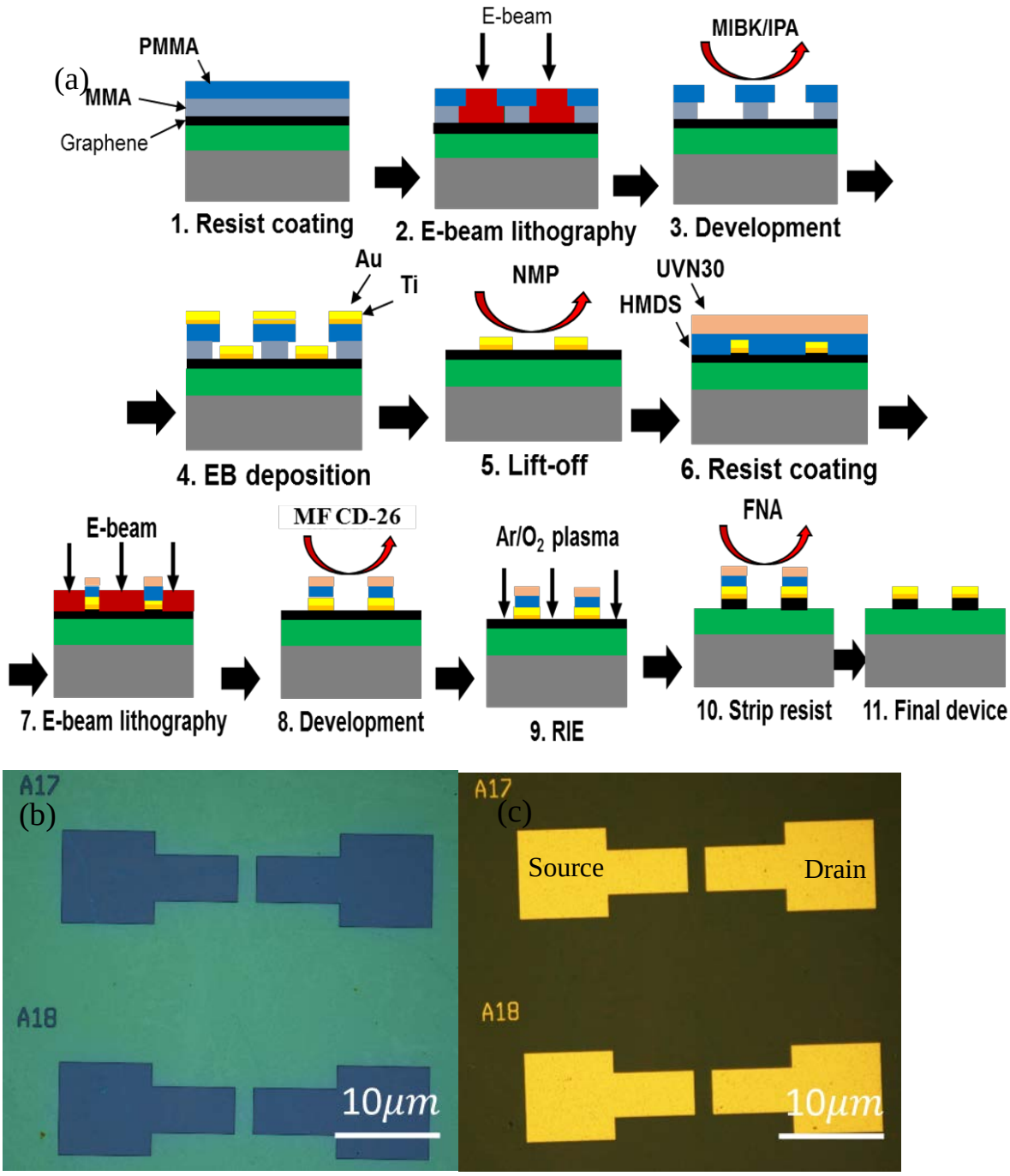

Figure 5.4: (a) Schematic illustration of fabrication process flow for GNR. (b) Optical microscopy image after MMA/PMMA development. (c) Optical microscopy image after lift-off.

After that, the exposed chip was developed in a mixture of 1:1 of *Methyl isobutyl ketone* (MIBK) and 2-Proposal (IPA) for 90 seconds, rinsed in IPA for 30 seconds and then dried. After the e-beam lithography, the chip was metallised by using e-beam evaporation of Ti/Au (10nm/100nm) at a base pressure of 3×10^{-7}mbarand a deposition rate of 0.5 Å/second, with the e-beam operating at 10 keV in a Leybold LAB700 evaporator. Then the sample was dipped in *N-Methyl-2-Pyrrolidone* (NMP) at room temperature and left overnight for lift-off. Pipetted method was used for lift-off and then the chip was rinsed in DI water and IPA.

The second e-beam lithography patterning was used for defining the GNR channel with the dimensions of 20 μm in length and 2 μm in width as shown in Fig. 5.4(a.7-11). The soft-bake in the oven at 210 ^{o}C for 1 min was used for the chip before spin-coating the resist in order to dehydrate and remove any water molecules in the chip. After that the chip was placed into *hexamethyldisilazane* (HMDS) vapour for 3 min at room temperature to coat it as primer in order to improve the adhesion and stability of the resist. UVN30 DUV negative resist was spun on the chip at 6000 rmp and baked at 110 ^{o}C for 1 min. The e-beam lithography system was used for patterning with a dose of 120 μC/cm^2 and at an acceleration voltage of 100 keV. The post-bake was used in order to stabilise the UVN30 resist after exposure. MEGAPOSIT (MF CD-26) was used to develop for 1min followed by rinsing in DI water for 1min, and then dried. A Plasma Lab System 80 Plus reactive-ion-etch (RIE) plasma etch tool was used to transfer the lithography pattern onto the graphene by etching the unwanted area of graphene. Before we started etching graphene, the RIE chamber was cleaned with an O_2 plasma run with a 200 sccm O_2 gas flow and an RF power of 200 W for 10 minutes. This was used in order to reduce the contaminants/polymers from the walls of the chamber and re-deposition on the graphene sample during etching. In developing RIE recipes, the range of 10-30W of RF power was used and was varied in 5 W steps. The etching time was varied between 5-30 seconds for the plasma gas flow in the chamber for etching. According to literature, the Ar/O_2 gas flow is required for the graphene etching [136-138]. Also, according to other group's works, the pure O_2 gas flow can be used to etch the graphene [139, 140]. In our experiment, an Ar/O_2 gas flow was used, but the ratio of these gases was changed depending on the DC bias voltage at a given RF power. The gas flow found in the literature was varied for example 1:1 [141], 2:1 [142], 9:1 [143]. We tested different Ar/O_2 gas flow ratios from 1:1-9:1. After that, we found that for graphene etching, a 4:1 (Ar/O_2) ratio is an optimal condition for the most stable DC bias voltage values at a varied RF power. At the end, the graphene was etched at the RF power of 20W for 30 seconds etching time with the 4:1 Ar/O_2 gas flow ratio with a vacuum pressure of ~100 mTorr. According to literature, in order to strip the UVN30 resist, various methods can be used such as chemical stripping bath of MICROPOST® REMOVER 1165 [144] or Fuming-Nitric Acid (FNA), or oxygen plasma. However, for stripping the UVN30 resist from graphene, the oxygen plasma cannot be used because the oxygen starts to etch the graphene. Therefore, Fuming-Nitric Acid (FNA) dipping was used to remove the UVN30 resist for 3 minutes in two baths, followed by rinsing in deionised (DI) water.

The GNR sample was irradiated using a Zeiss ORION scanning helium ion microscope (HIM) with an acceleration voltage of 30 KV. In order to obtain good HIM image brightness and contrast, the beam current was kept at 1pA.and 55 pixel/nm^{2}spacingwas used, and 3 µs dwell time was used for each pixel for various irradiation dosages, 1.4x10^{13}, 2.34x10^{13}, 4.16x10^{13}, 1.6x10^{14}, 2.36x10^{14}, 5x10^{14}, and 1-6x10^{15} ions/cm^2. Fig. 5.5 shows the HIM image of GNR channel, where the (right-hand-side) half of the channel was irradiated.

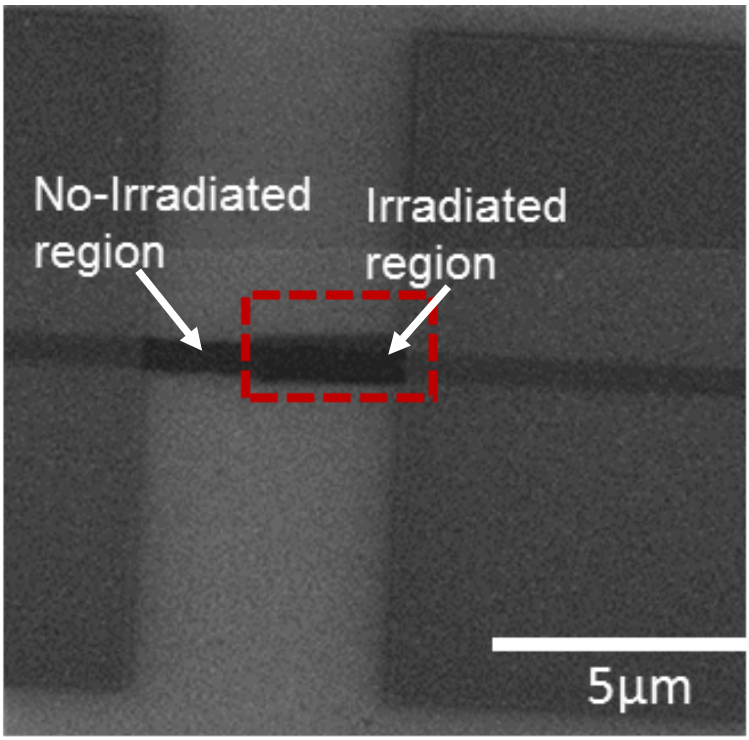

Figure 5.5: Helium Ion Microscope (HIM) image of GNR channel after irradiation.

A semiconductor device analyser (Agilent B1500A) was used for electrical measurements to measure two-point resistance of GNR devices in an atmospheric environment at room temperature as shown in Figuer5.6. We measured the change of the drain current by applying the back-gate voltage through the p-doped Si substrate under the constant source-drain bias voltage V_{ds} = 10 mV. This is known as the back-gate modulation characteristics.

A Nanonics Multiview MV4000 integrated with a Renishaw inVia Raman spectrometer was used for TERS measurements. A schematic setup of TERS is described in section 3.4 and it is shown in Fig.3.5 (b).

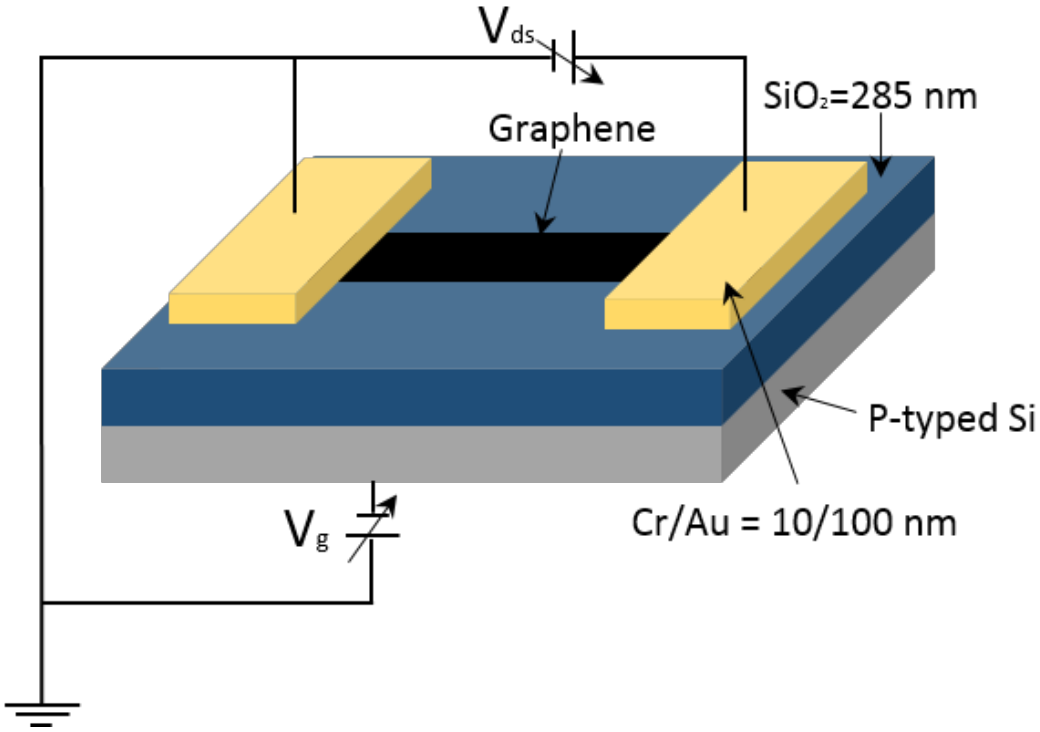

Figure 5.6: The electrical measurement setup for graphene device.

5.4 Results

5.4.1 Electrical measurements

Generally, helium ion irradiation on GNR can change its properties. Therefore, electrical characteristics of GNRs device were measured before and after the irradiation in order to investigate how the nature of devices is changed due to helium ion irradiation. The electrical drain current (I_d) vs back-gate voltage (V_{bg}) characteristics of the GNR channel before and after He ions irradiation with the dose level of S = 5 x 10^{14} ions/cm^2 is shown in Fig. 5.7. The results show that the GNR channel has p-type nature, i.e. hole doping before and after He-ion irradiation. The conductivity of GNR is reduced after He-ion irradiation, and this is due to the fact that the defect induced and hole carrier density increases in the graphene[145]. The electrical drain current (I_d) vs back-gate voltage (V_{bg}) characteristics of the GNR channel with different He-ion dose levels are shown in Fig. 5.8 (a) and (b).

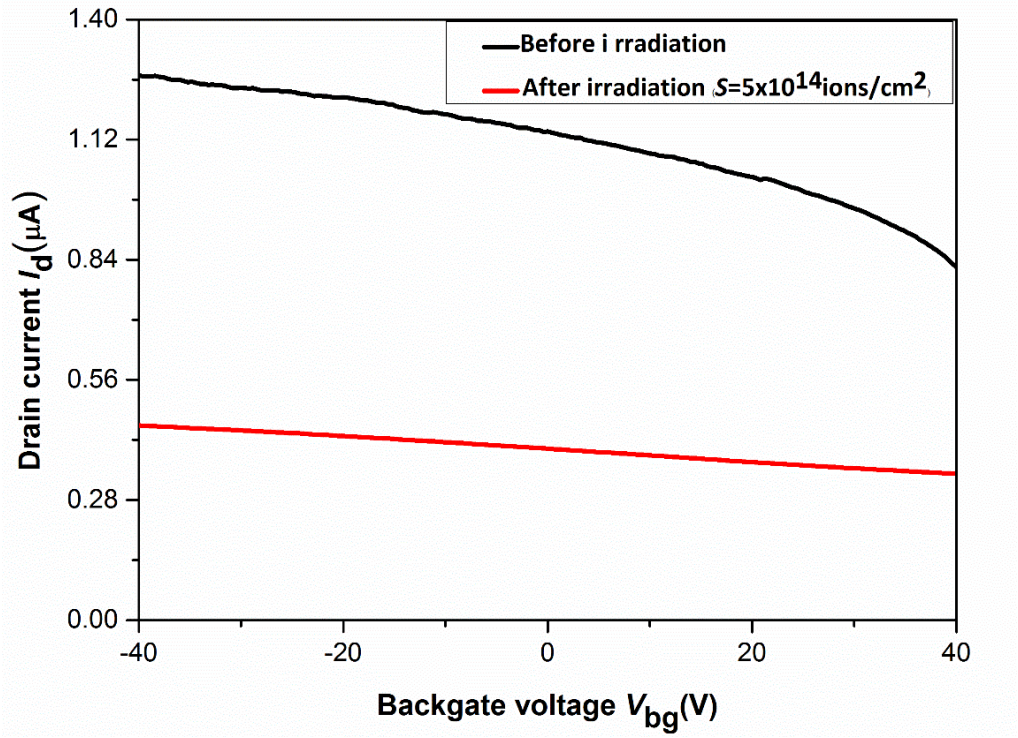

Figure 5.7: Electrical characteristics of GNR channel before irradiation and after He-ions irradiation with (S=5x10^{14} ions/cm^2).

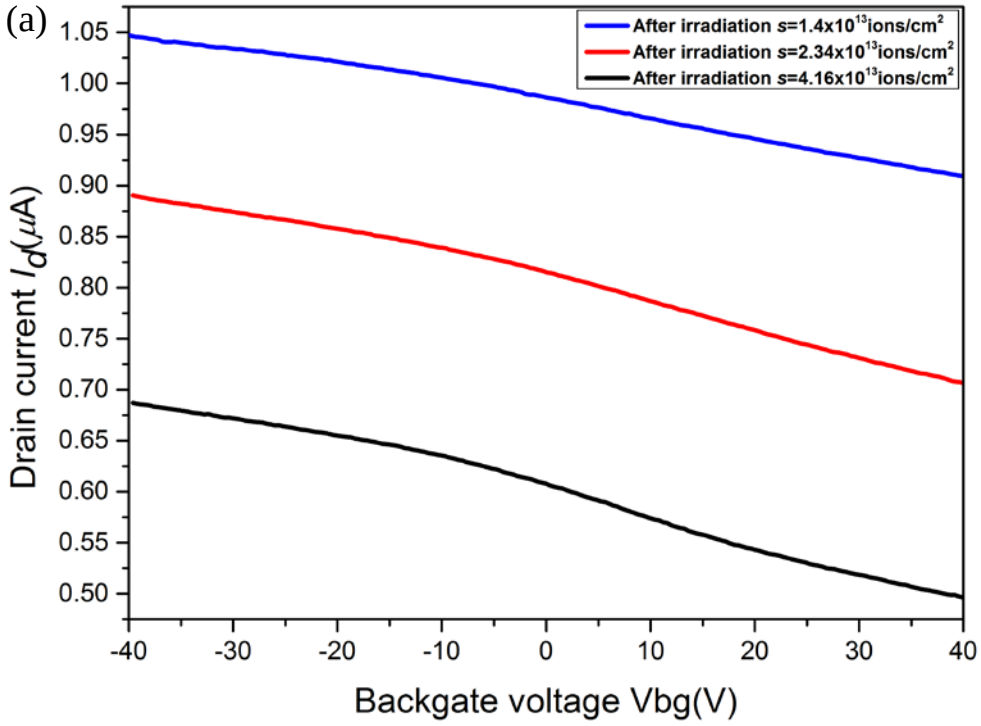

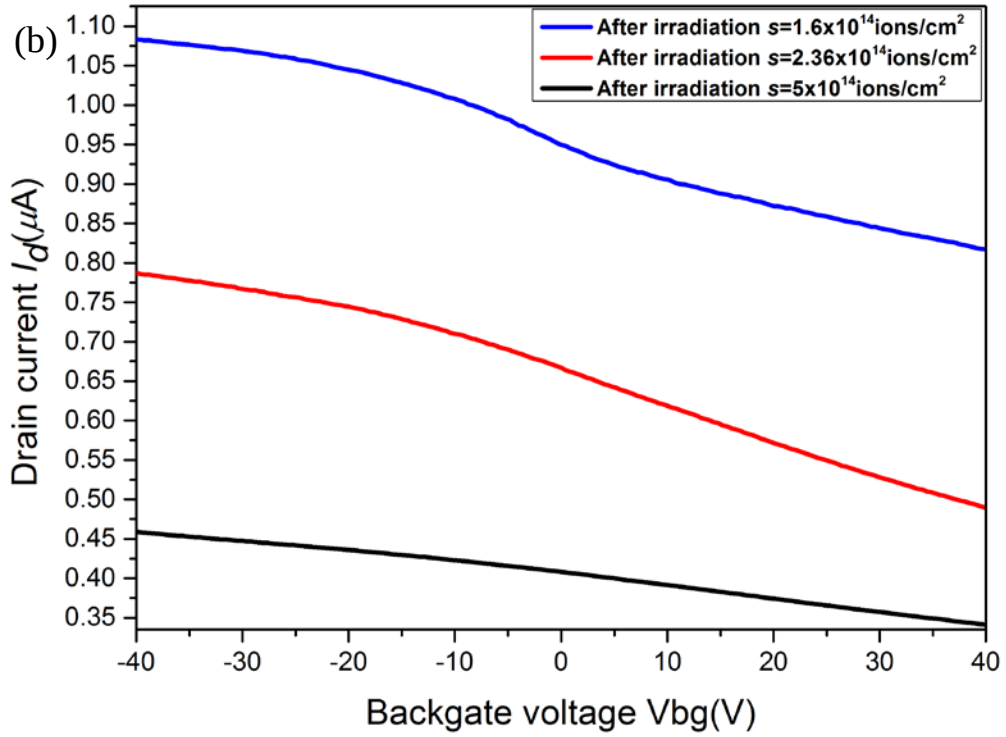

Figure 5.8: Electrical characteristics of GNR channel after He-ions irradiation (a) with a dose level S = 1.4 x 10^{13}, 2.34 x 10^{13}, 4.16 x 10^{13} ions/cm^2, and (b) with a dose level S =1.6 x 10^{14}, 2.36 x 10^{14}, 5 x 10^{14} ions/cm^2.

5.4.2 Micro-Raman scanning across the irradiation boundary

Figure 5.9 shows the evolution of micro Raman spectra of the exposed GNR channel with 12 various irradiation dosage of 1.4 x 10^{13}, 2.34 x 10^{13}, 4.16 x 10^{13}, 1.6 x 10^{14}, 2.36 x 10^{14}, 5x 10^{14}, and 1-6 x 10^{15} ions/cm^2. With increasing the irradiation dose, the peaks originated from graphene are changed: The 2D peak at ~2400-2800 cm^{-1} is disappeared, and the line shapes of the G peak at ~1595 cm^{-1} is affected by emerging intensity of the D' peak. The peaks originated from disorders, D and D' at ~1326 cm^{-1}, 1620 cm^{-1}, respectively, appear for defective samples with increasing the doses[146].

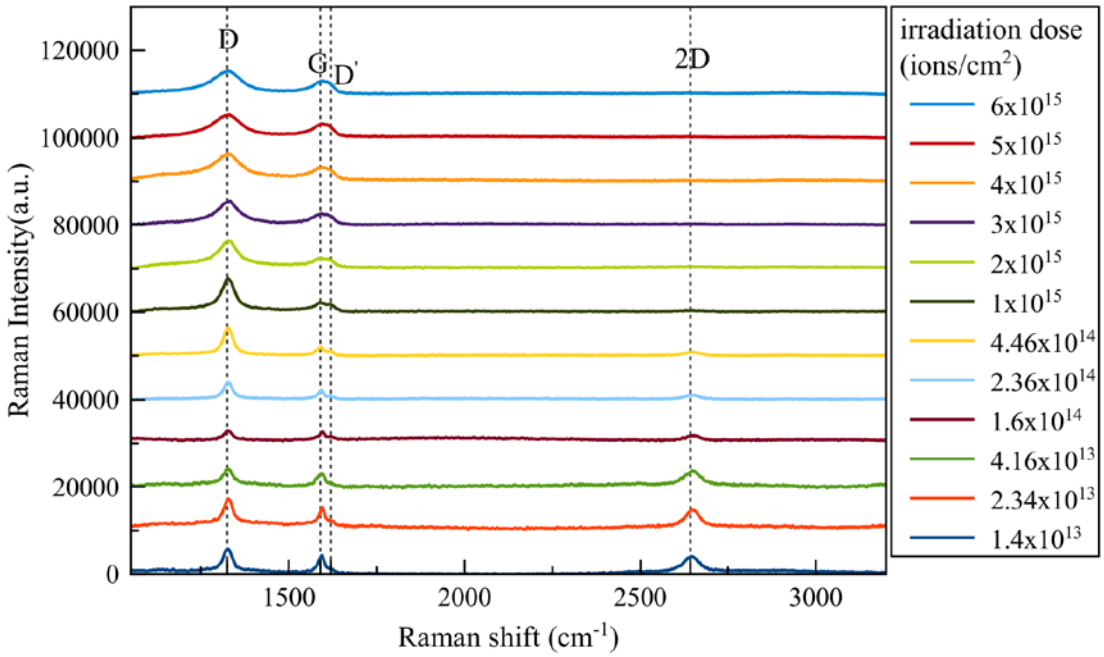

Figure 5.9: Micro-Raman spectra of GNR channel with 12 various dose level of 1.4 x 10^{13}, 2.34 x 10^{13}, 4.16 x 10^{13} ions/cm^2, 1.6 x 10^{14}, 2.36 x 10^{14}, 5 x 10^{14}, 1-6 x 10^{15} ions/cm^2.

Figure 5.10(a), (b) and Figure 5.11 show the ratio of the D peak intensity to the G peak intensity I_D/I_G across the boundary between the irradiation and non-irradiation regions along the graphene channel for each dose level of 1.4 x 10^{13}, 2.34 x 10^{13}, 4.16 x 10^{13} ions/cm^2 (Fig. 5.10 (a)), 1.6 x 10^{14}, 2.36 x 10^{14}, 5 x 10^{14} ions/cm^2 (Fig. 5.10 (b)), and 1-6 x 10^{15} ions/cm^2 Fig. 5.11. I_D/I_G is extracted from the spectral fitting results. In general, I_D/I_G indicates the amount of the defects in graphene. The boundary between the regions is clearly presented as the huge change of the peak intensity for the samples with the dose level of 10^{14}-10^{15} ions/cm^2, while the intensity change between the regions is too small to be investigated for the one with the dose level of ~10^{13} ions/cm^2.This is because after observe graphene with HIM a certain level of He^+ ions is ready induced on the graphene.

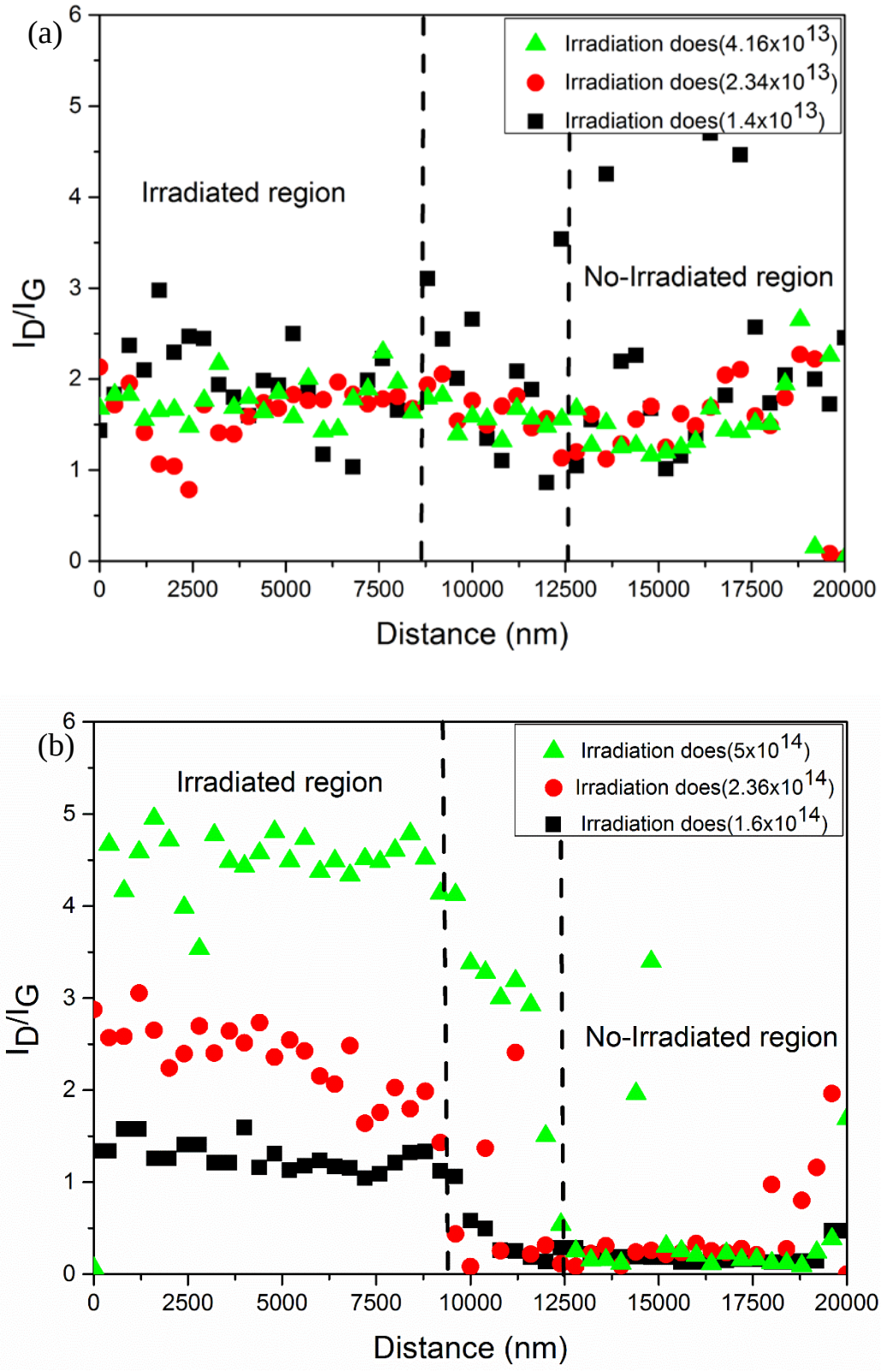

Figure 5.10: Micro-Raman scanning a cross from irradiation region to No-irradiation region. (a) With does level (S=1.4x10^{13}, 2.34x10^{13}, 4.16x10^{13}ions/cm^2). (b) With does level (S=1.6x10^{14}, 2.36x10^{14}, 5x 10^{14} ions/cm^2).

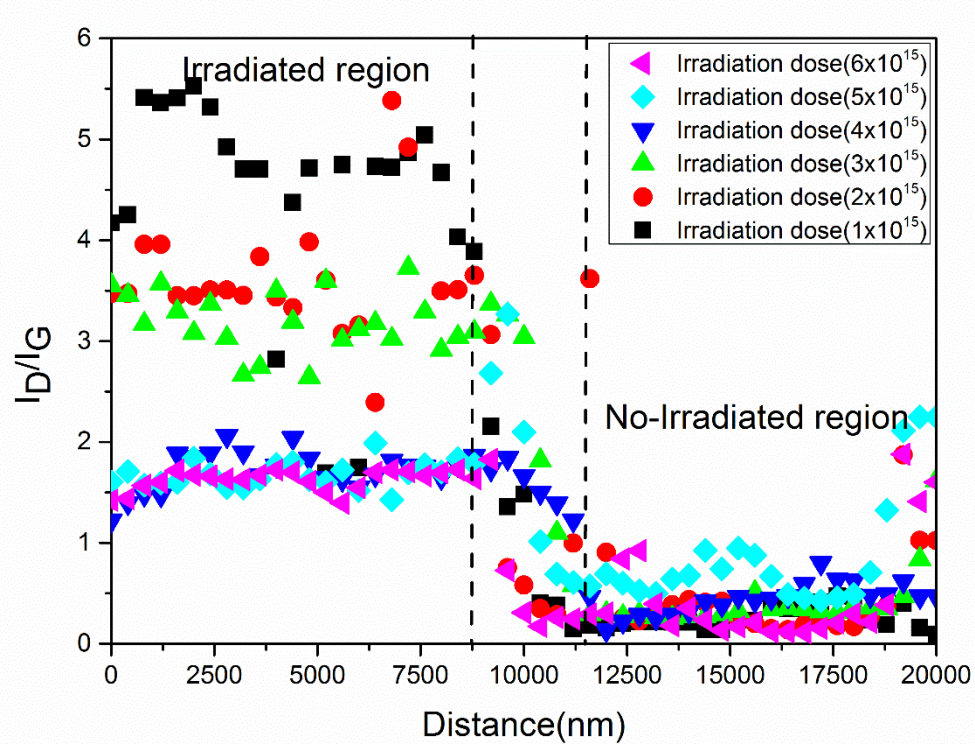

Figure 5.11: Micro-Raman scanning a cross from irradiation region to No-irradiation region with dose level (S=1-6x10^{15}ions/cm^2).

To investigate the effects of helium ion irradiation onto the crystallinity of the graphene, the peak position and the full width half maximum (FWHM) of the 2D, G and D peaks are plotted as a function of the log of the irradiation dose in Fig. 5.12 (a), (b), and Fig. 5.13 (a) , respectively. Figure 5.13 (b) shows the ratio of the D peak intensity to the G peak one, I_D/I_G, and that of 2D to G, I_{2D}/I_G, as a function of the log of the irradiation dose. According to the I_D/I_G plot in Fig 5.13 (b), the defect density starts to increase when the dose level exceeds 2 x 10^{14} ions/cm^2. Then the ratio shows a maximum for the one with ~ 1 x 10^{15} ions/cm^2 and decreases with increasing the dose. Interestingly, compared with the peak position of the 2D and G peaks shown in Fig. 5.12 (a) and (b), the FWHM of the peaks shows significant increase around the S of 2-5 x 10^{14} ions/cm^2, suggesting that crystallinity of the graphene is significantly changed due to the helium ion irradiation. Therefore, in the following TERS measurements, we have focused on studying a sample with the dose level of 5x10^{14} ions/cm^2.

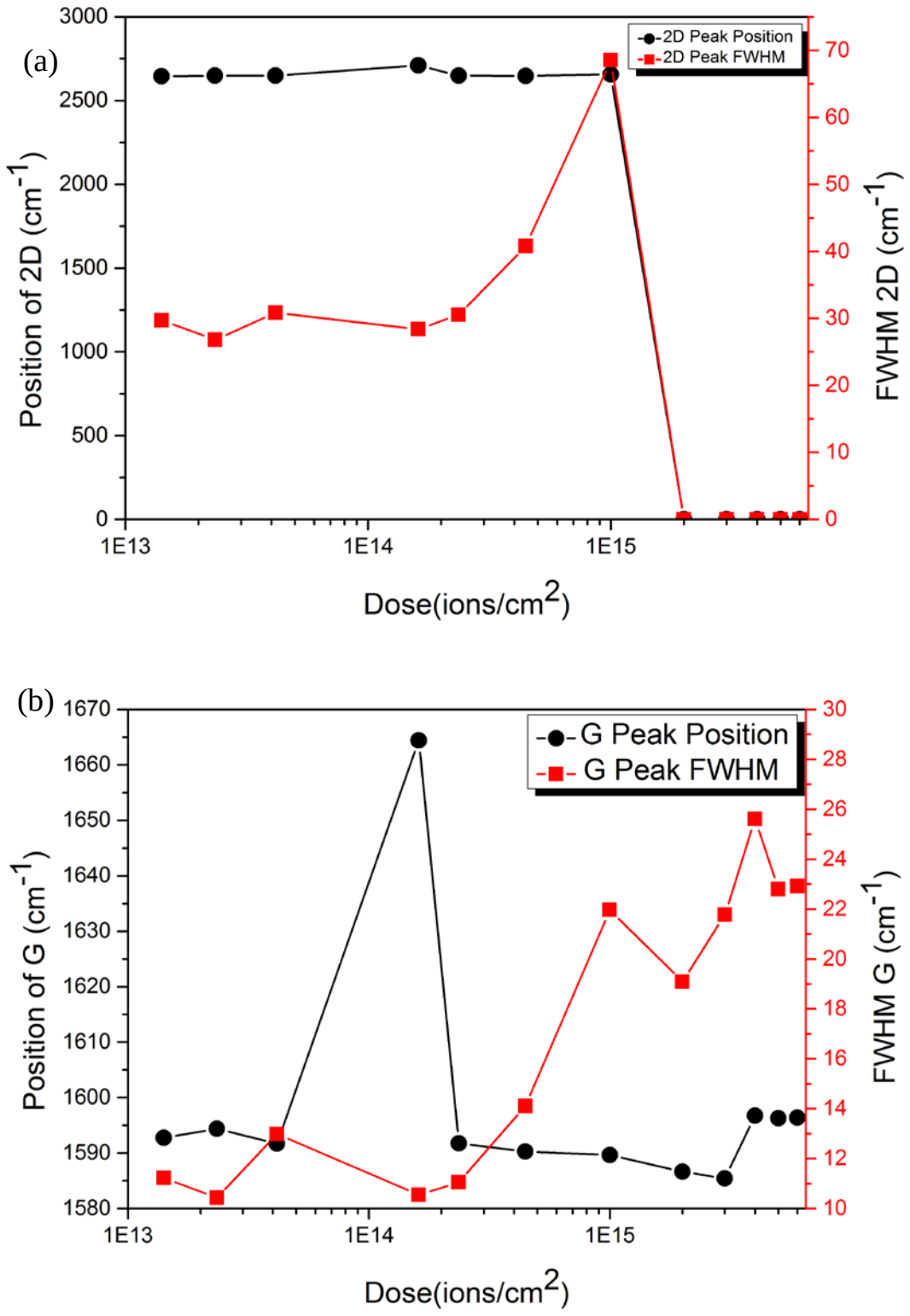

Figure 5.12: The evaluation of the Raman peaks of irradiated graphene as a function of the dose: Position and FMWH of (a) 2D peak, and (b) G peak.

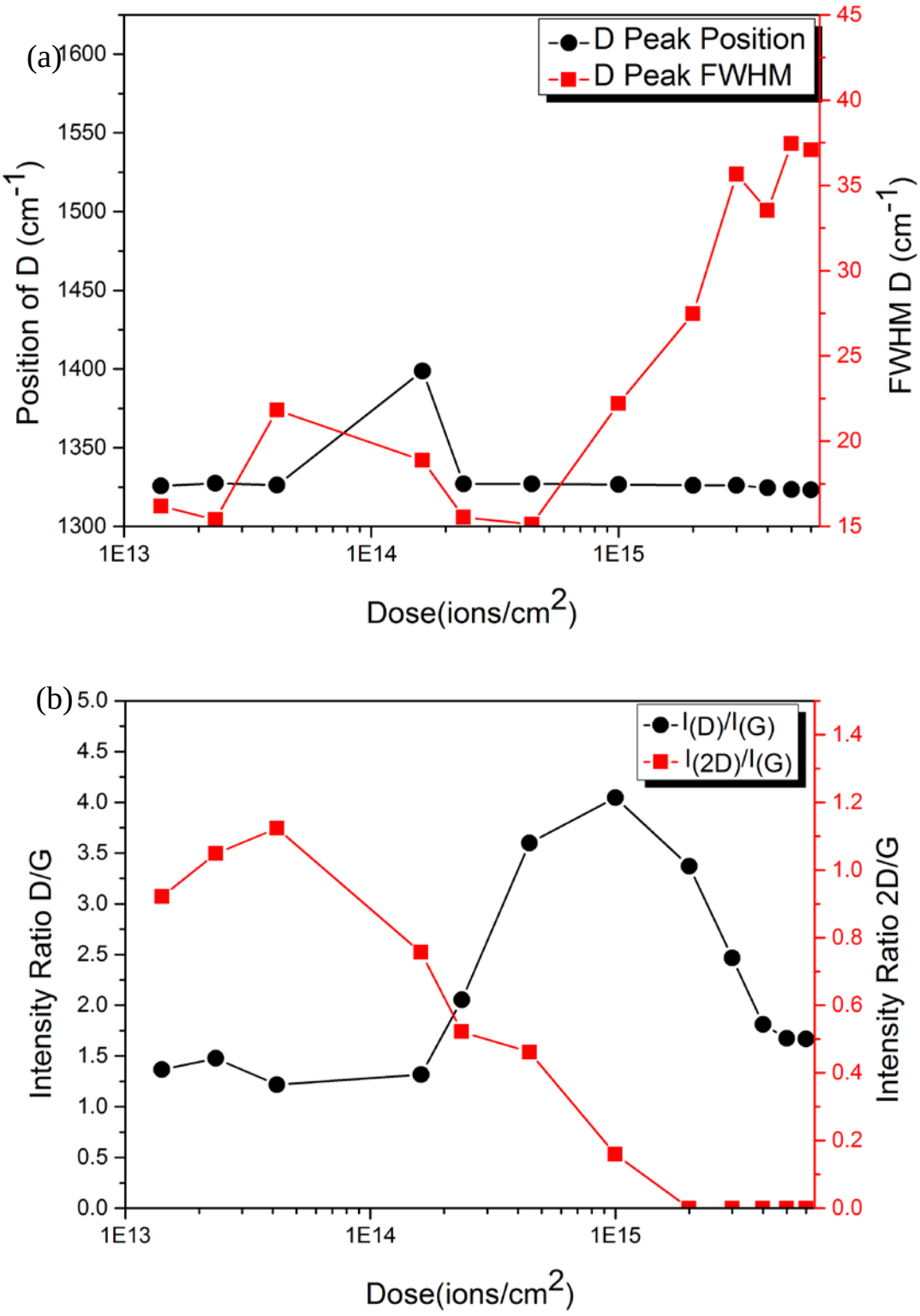

Figure 5.13: The evaluation of the Raman peaks of irradiated graphene as a function of the dose: Position and FMWH of (a) D peak are plotted. (b)Intensity ratios of I_D/I_G and I_{2D}/I_G as a function of the dose level.

5.4.3 TERS scanning across the edge of non-irradiated and irradiated graphene

In this section, the TERS spectra taken across the edges and boundaries are analysed by comparing with theoretical formula. The AFM topography image of the irradiation graphene is showing in Fig.5.14. The three arrows in the figure correspond to the traces of TERS tip scan across (1) the edge of the non-irradiated graphene, (2) the edge of the irradiated graphene, and (3) the boundary between non-irradiated and irradiated regions. According to Ref.[97], the G peak intensity I_G obtained in TERS across the non-irradiated graphene edge can be approximately expressed as

$$I_G = \sqrt{\frac{\pi}{8}} A_2 w_2 \left[1 - erf\left\{\frac{\sqrt{2(x-x_c)}}{w_2}\right\}\right] \qquad (6.\ 1)$$

Where A_2 is the scale factor, x_c is the position of the edge, and w_2 is the spatial resolution of TERS. The fitting result for the edge of non-irradiated graphene using the equation above is shown in Fig. 5.15, where the TERS spatial resolution of $w_2 = 197\ nm$ is obtained. This result is reasonably consistent with the Au particle size at the tip of 200 nm. Similar results were obtained in ref[147]. Figure 5.16 shows a fitting result of the G peak intensity across the edge of irradiated graphene using the equation above. The TERS spatial resolution of$w_2 = 431\ nm$ has been extracted from this fitting. In principle, the spatial resolution should not be changed depending on the sample. The obtained larger w_2 indicates that damaged edge by ion irradiation cannot be described with the equation above so a modification term that parameters related to the disorder should be considered to explain. Furthermore, when the equation above is applied for the G peak intensity across the boundary from the non-irradiated region to irradiated region. It has been found that the spatial resolution parameter is estimated to be $w_2 = 181\ nm$ as shown in Fig. 5.17. Obviously the equation above is not well fitted and applicable for analysis irradiation graphene as the one is for non-irradiated graphene, but it is interesting that a similar w_2 value has been extracted from this analysis. In the case of scanning across the boundary, the G peak intensity should be remained in the both regions. Further development of the theoretical expression considering the defects and disorder will be required for more accurate fitting to extract the parameters associated with the disorder level of the edges and boundaries.

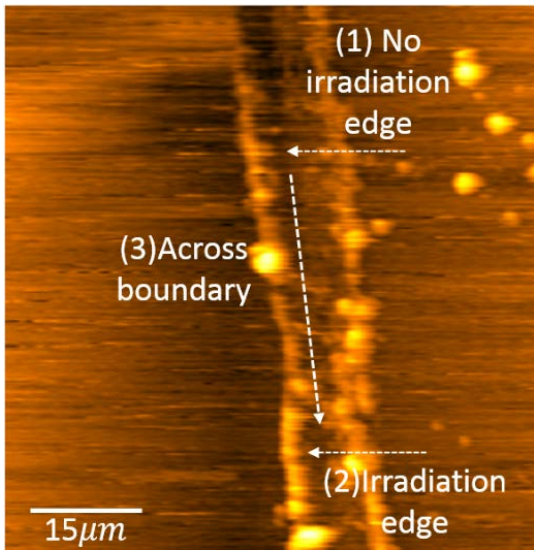

Figure 5.14: AFM topography image of irradiated graphene. The arrows correspond to the traces of TERS tip scan. (1) the edge of the non-irradiated graphene, (2) the edge of the irradiated graphene, and (3) the boundary between non-irradiated and irradiated regions.

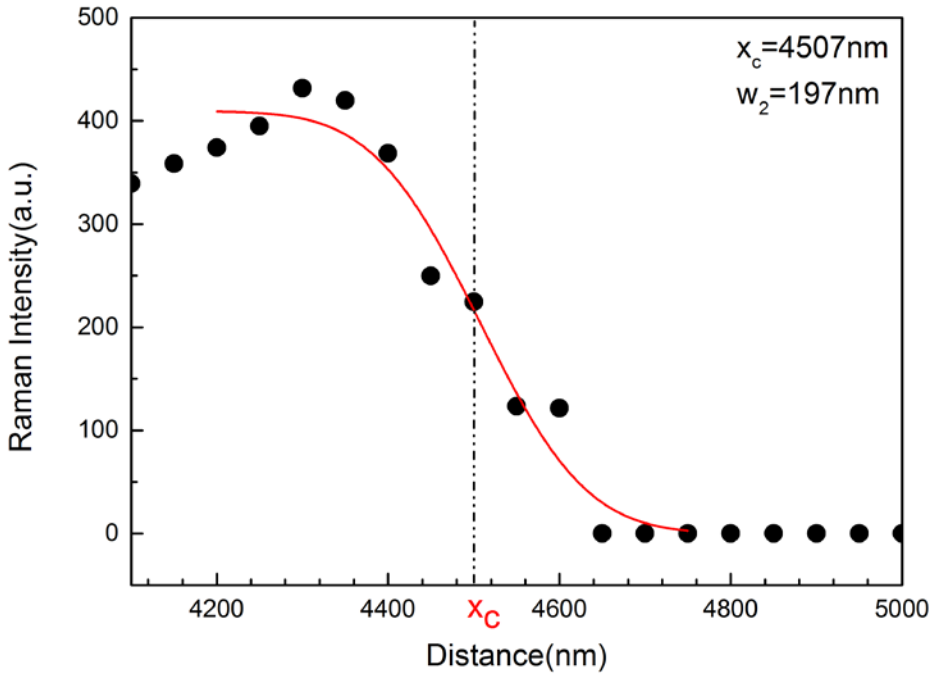

Figure 5.15: The intensity profile of G peak across the edge of non-irradiated graphene.

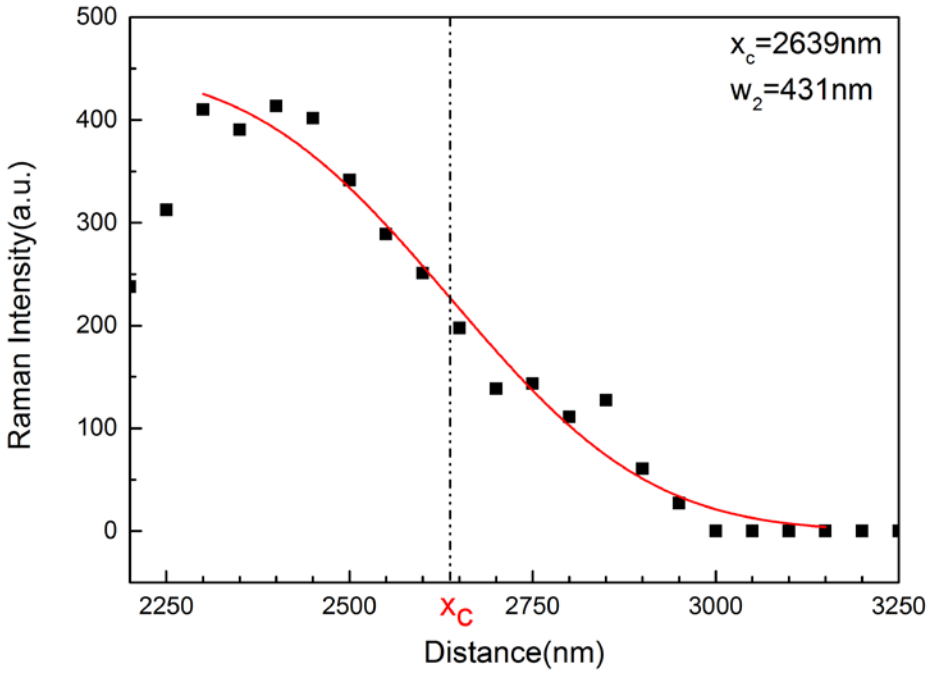

Figure 5.16: The intensity profile of G peak across the edge of irradiated graphene.

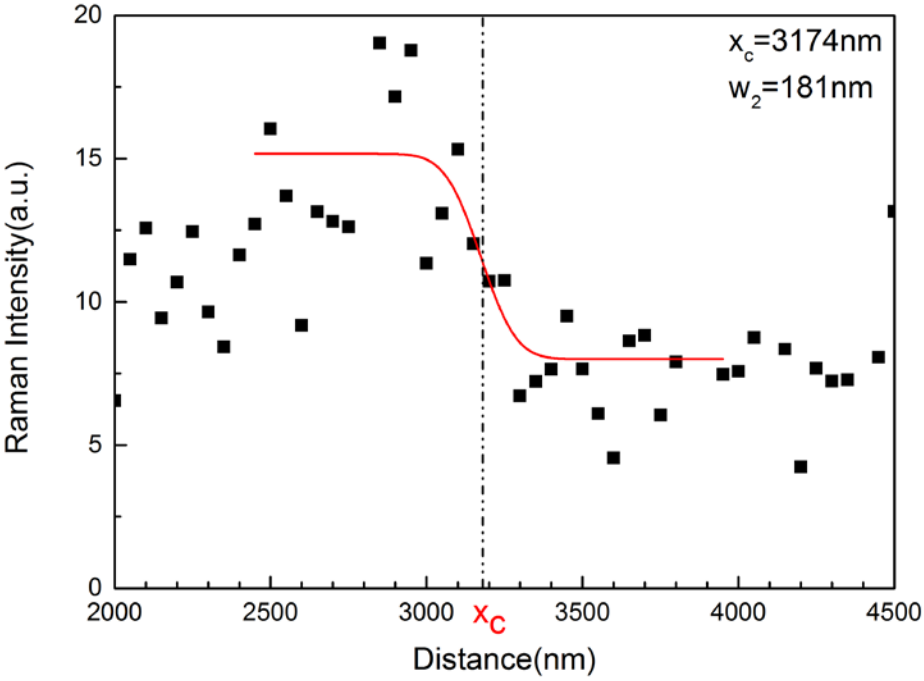

Figure 5.17: The intensity profile of G peak across the boundary between the non-irradiated and irradiated regions.

5.4.4 TERS scanning across the irradiation boundary

Figure 5.18(a) shows an AFM topographic image of a GNR channel, where the top half of the channel is irradiated by He ions with the dose level of 5x 10^{14}ions/cm^2. The red line in the figure suggests the trace where spectral line scanning has been done by using TERS. The

spectra taken for the D and G peaks across the boundary is presented in Fig.5.18 (b) and (c), respectively. As explained before, the TERS spectra are obtained from the subtraction of the spectra with tip contacted form the ones without tip contacted. Clear enhancement of the individual peaks has been confirmed even for irradiated regions as shown in Fig 5.18 (a), where the spectrum with tip contacted is shown in red, with tip retracted in black, and the subtracted spectrum in blue. The strong D peak intensity and the D' peak shoulder observed in the spectra suggest that introduction of defects was successful. After fitting of a series of spectra with tip-retracted, equivalent to the far-field Raman spectra, and TERS spectra, I_D/I_G, G peak position, D peak position and 2D peak position are plotted as a function of the position along the graphene channel in Fig.5.19 (b), (c), (d),and (e), respectively.

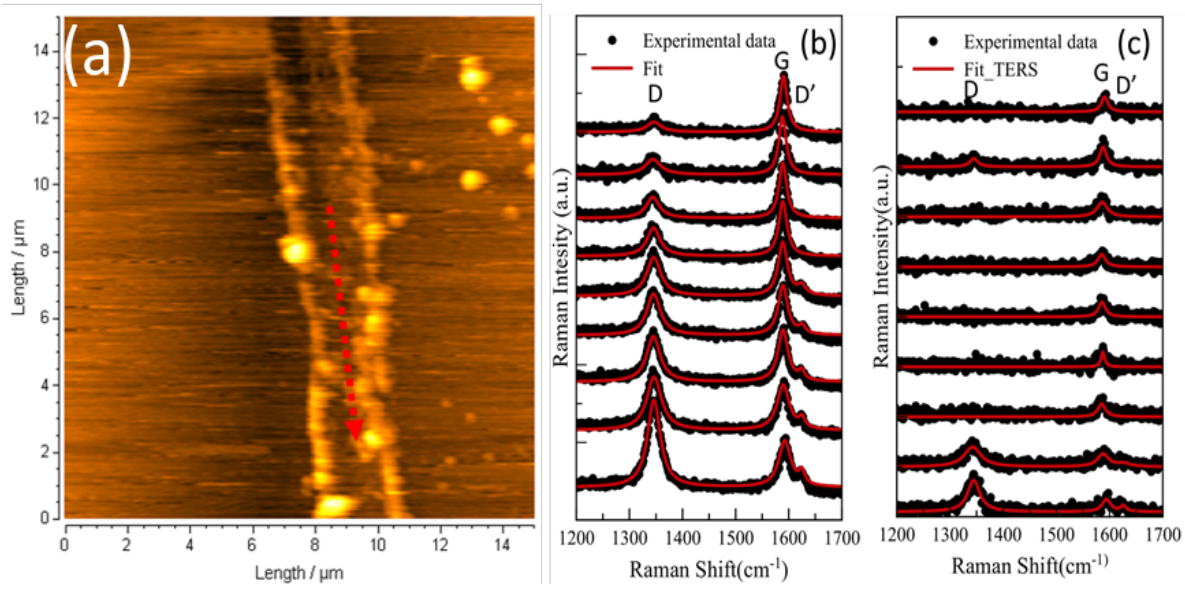

Figure 5.18: (a) AFM topography image of graphene channel. TERS measurement result across the Graphene channel from irradiation to No-irradiation region. (b) Raman signal without tip. (c)TERS spectra.

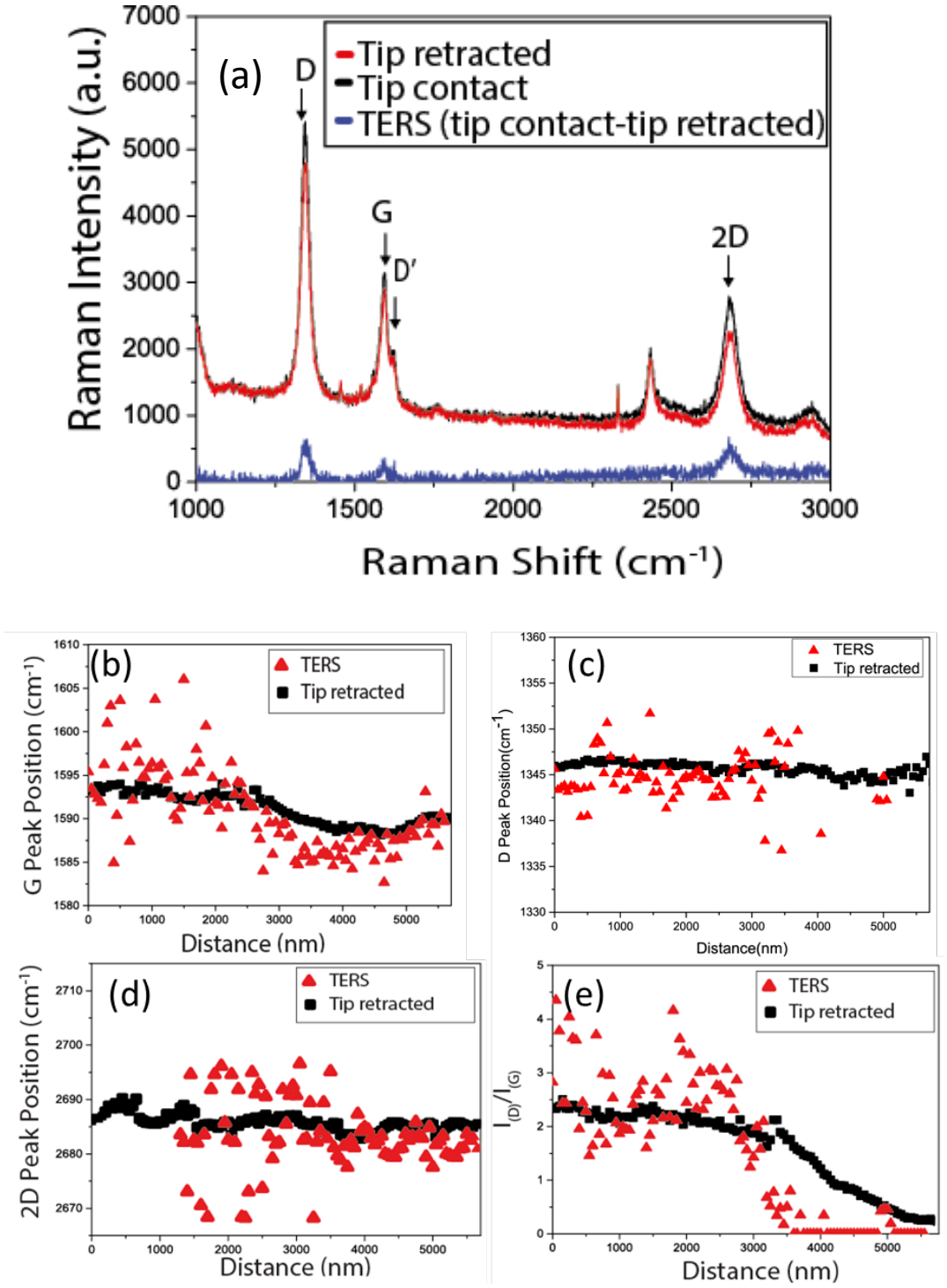

Figure 5.19: (a) Spectra with tip contacted and with tip-retracted, and subtracted TERS taken from irradiation region. The extracted data from the fitting of the far-field and TERS spectra, G peak position, D peak position, 2D peak position ,and I_D/I_G, are plotted along the position on the graphene channel in (b),(c), (d) and(e),respectively.

5.5 Discussion

For the result of electrical measurement, as we briefly discussed above, the fabricated graphene channels show p-type nature. This is a typical behaviour for the graphene measured at an ambient environment and said to be due to effects of O_2 and H_2O molecules adsorbed

in between the graphene and substrate [148], occurring in the graphene transfer process to the substrate. The conductivity of GNR is reduced after He-ion irradiation, and this due to the hole carrier density increases in the substrate [145]. Figure 5.7, and Figure 5.8(a) and (b) clearly show the conductivity of He-ion-irradiated GNR channel decreases with increasing the dose level. This is could be due to two reasons: (1) amorphisation with increasing the defect density and (2) effect of the graphene transfer mentioned above.

Next, we discuss the Raman spectrum result taken for various irradiation doses as shown in Fig.5.9. As mentioned above, the Raman spectra show clear D and D' peaks and these peaks should appear in damaged graphene samples [146]. Therefore, the appearance of these peaks strongly suggests that disorder and defects are generated after He^+ irradiation. With increase irradiation dosage, the intensities of these peaks increase. This is due to further increase of disorder and the defect density on the graphene. On the other hand, the intensities of 2D peaks dramatically decrease with increasing the irradiation dosage, and this means the poor crystallinity of graphene after relatively large amount of irradiation. This point has been observed previously in the literature, where the D peak intensity growth is reported for damaged graphene [149]. Figure 5.12 (a), (b) and Figure 5.13(a) show the ratios of the D peak intensity to G peak intensity I_D/I_G extracted from fitting of Micro Raman spectra across the GNR channel including the boundary from irradiation region to non-irradiation region. With increasing the dosage, the increase of the intensity ratio becomes larger while there is almost no changes in the cases for the samples with the dose level of less than 10^{14} ions/cm^2. This result suggests that among these irradiation conditions used in this study, the defect density level introduced by ion irradiation with the dose level of ~10^{13} ions/cm^2 cannot be detected in the current Raman spectroscopy system. This is another reason why the dose level of ~ 5 x 10^{14} ions/cm^2 has been focused in this study. Figure 5.13 (b) shows the two intensity ratios as a function of the log of the irradiation dose. The I_D/I_G increases with increasing the dosage in the range of 10^{13}-10^{14} ions/cm^2 and then the intensity ratio starts to decrease from the one with 2 x 10^{14} ions/cm^2. For further analyses of Raman results, the three stage theory described in ref [75, 150, 151] is considered. The theory is about disordered and amorphous carbon amorphisation trajectory covering (1) graphite to nanocrystalline graphite, (2) nanocrystalline graphite to low sp3 amorphous carbon, and (3) low sp3 amorphous carbon to high sp3 amorphous carbon. By considering this theory and Raman spectra evolution of in the stage 1 and 2 in ref[75], it is concluded that our I_D/I_G intensity ratio data is more related to the stage 1 and 2. The observation clearly suggests that, due to increase of irradiation exposure, the crystalline phase of graphene has been transferred

to nanocrystalline phase and then amorphous phase. From Figure 5.12(a) and 5.13(a), it is hard to identify Raman peak position shift for the 2D and D peaks. On the other hand, the behaviour of the G peak is explained by following the theory in Ref. [75, 151]. In stage 1, the G peak should be wide and fitted with a single Lorentzian curve, and the peak should be blue-shifted up to ~1595 cm^{-1}. This is roughly consistent with the results of the samples with the dose level of 10^{13}-10^{14} ions/cm^2. In stage 2, the G peak should be red-shifted. This corresponds to the result from the samples with higher dose levels showing the decrease of the shift from ~1595 cm^{-1} to ~1580 cm^{-1} with increasing the dose level. This tendency is supported by the results of FWHM of the G peak that becomes wider with increasing the dose level as well as the increase of FWHM for D and 2D peaks, corresponding to the increase of the disorder. However, the G peak acts strange with high irradiation dosage (> 10^{15} ions/cm^2 comparing with low irradiation dosage of 10^{13} -10^{14} ions/cm^2. This strange behaviour can be due to three effects that might happen to the G peak [80, 152]: (1) the peak width becomes wider due to the fact that the disorder starts to appear under irradiation, (2) the peak width becomes narrower as the doping starts to be produced into irradiated graphene; and (3) strain effect induced after irradiation or relevant fabrication processes such as etching. From Figure 5.12 (b), these effects are not clearly identified but with increasing the irradiation dosage, the disorder-induced D' peak start to be seen. At further higher irradiation dosage, the doping effect is shown, and then the G peak started to be wider.

For more understanding of the transfer from the crystalline phase of graphene to nanocrystalline phase and amorphous, TERS is applied for studying the sample with the irradiation dose 5x10^{14} ions/cm^2. The region where clear step-like changes of I_D/I_G and G peak position are observed corresponds to the boundary of the irradiated region as shown in Fig.5.19 (b) and (c). Note that the slope of the change of the TERS spectra is much steeper than that of the far-field spectra, suggesting that the higher spatial resolution has been achieved. In particular, clear enhancement of I_D/I_G is observed at the edge, indicating further enhancement of the defect density at the edge. Another interesting behaviour is a relatively large shift of the G peak position in TERS. Recently Iwasaki *et al.* have determined the change of doping concentration across wrinkle-like defect structures from the analysis of TERS spectra [147]. In the case of the edge of an irradiated area, characteristic features are (1) G peak position is clearly changed while the 2D peak position is not, and (2) a relatively larger red-shift of the G peak position at the edge in TERS. Not an only change of doping concentration but also induction of strain by swelling may need to be taken into account for the artificially induced edges.

5.6 Conclusions

In this chapter, the electrically measurable graphene channel has been fabricated by using e-beam lithography and effect of helium ion irradiation on the structural and electrical properties of the graphene channel has been investigated by using electrical characterisation and Raman measurements. In particular, a sharp change of the defect density at an artificially-created boundary between the irradiated and non-irradiated graphene has been observed by using Tip-enhanced Raman spectroscopy for the first time. The electrical measurements show the conductivity of the graphene has been decreased after irradiation, suggesting amorphisation of the irradiated area as well as the change of doping concentration. The irradiated graphene channels have showed typical characteristics in Raman spectra, such as appearance of D and D' peaks due to induction of defect and disorder, and disappearance of the 2D peak and G peak broadening at further higher dosage. Evaluation of the intensities ratio I_D/I_G, FWHM, and position of the G peak has specified that the sample under the irradiation, especially at the high dose level, have transformed from the crystalline phase of graphene to nanocrystalline and amorphous phase. Successful observation of the graphene edges and the edge of the He-ion-irradiated region on the graphene channel has confirmed that higher spatial resolution is achievable with TERS.

Chapter 5

Chapter 6: **Conclusion and Future work**

6.1 Conclusion

In this thesis, I have focused on developing TERS as a tool to be applied for nanoscale graphene device imaging and applied for characterising suspended graphene and he-ion-irradiated graphene for the first time.

First, in order to stabilise the TERS tool, test measurements have been conducted by using standard monolayer graphene samples. After considerable attempts by adjusting key parameters such as the laser power, integration time and tip-laser position alignment procedure, I have eventually succeeded in obtaining the stable measurement environment where reproducible enhancement of the main graphene peaks are achieved.

Then the TERS with the high spatial resolution has been used to characterise suspended graphene on SiNW arrays. The strain and stress of suspended graphene on SiNWs, particularly at the edge of the sample has been investigated using TERS. The fabrication process has also been examined using AFM multimode to observe the suspended area of graphene on top of SiNWs array. As a result, a shift has been observed in the TERS spectra at edge of graphene located on the SiNW underneath. However, there has been no significant shift of the major graphene peak position in the Raman spectra without the tip. Furthermore, localised defects at the edge of SiNW has been observed in the intensity ratio I_D/I_G distributions with spatial resolution down to sub 100 nm.

Finally, I have studied the defect boundaries and edges on graphene channels which have been generated by ion bombardment using a helium ion microscope (HIM). Electrical measurements show the conductivity of the graphene has been decreased when the irradiation dose increases. The electrical measurement suggests that both amorphisation of the irradiated area of graphene and change of doping concentration can occur. Micro Raman characterisation across the irradiation boundary has shown the appearance of D and D' peaks due to induction of defect and disorder, and disappearance of the 2D peak and G peak broadening at further higher dosage. I have found that from the evaluation of the intensities ratio I_D/I_G, FWHM, and position of the G peak, the graphene phase is transformed from a crystalline phase to nanocrystalline and amorphous phases with increasing the dose level. Successful observation of the graphene edges and the edge of the He-ion-irradiated region

on the graphene channel has confirmed that higher spatial resolution is achievable with TERS.

6.2 Future works

In this thesis I have focused on graphene nanostructure devices on Si/SiO_2, Tip enhanced Raman spectroscopy technology and helium ion irradiation technology. This project can be extended for future research of graphene nanodevice fabrication and characterisation. Some idea for future works are listed below.

6.2.1 Quantitative analysis of TERS across the irradiation graphene boundary

Only one dose level of irradiated graphene has been studied using TERS in this thesis due to the time constraint. Further investigation and characterisation of the irradiated samples with different dose levels via TERS would provide further quantitative information about the damaged graphene and crystalline-amorphous phase transition. Furthermore, the study of the surface potential of the helium ion irradiation boundary on graphene by using Kelvin probe microscopy (KPFM) to obtain more information about the effect of the defect on doping concentration.

1.2.2 Annealing effect on irradiation graphene

Study of annealing effects using TERS for He^+ irradiated graphene would be interesting in order to reduce the number of the defects on graphene or to remove them. TERS is a great tool to investigate and to understand the effect of annealing on irradiated graphene regarding strain, doping, and edge deformation.

1.2.3 Graphene on a different substrate:

Recently, graphene has been grown or transferred to various types of the substrate, such as Si/SiO_2, Cu, SiC, Si, glass, hexagonal boron nitride (hBN), and PDMS etc. Study of the influence of substrate on graphene using Raman spectroscopy become very important. This has been already investigated by conventional Raman spectroscopy but not been yet using TERS. TERS technology will provide further information of strain which could be generated from the interaction between the graphene and substrate.

1.2.4 HIM irradiation for 2D materials

As shown in Fig. 6.1, the irradiation has been done on half of the graphene channel with the width of 3 μm and the length of 10 μm. This method can be developed by intruding the two square with the same size on the graphene channel. As shown in Fig.6.2. This can be used for single electron transistors (SETs) and, this direction could be aligned with quantum device applications.

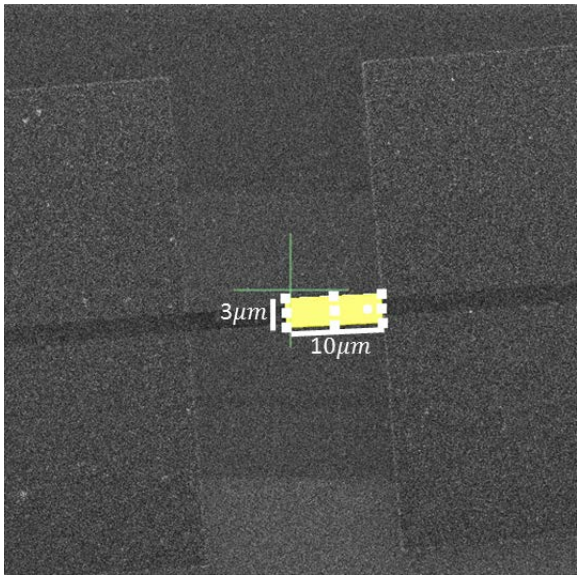

Figure 6.6.1: Helium Ion Microscope (HIM) image of GNR channel irradiation with .square height 3μm and length10μm.

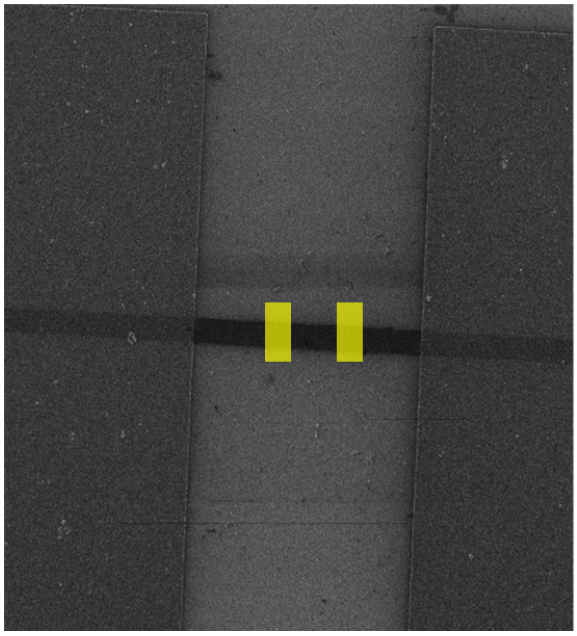

Figure 6.6.2: Helium Ion Microscope (HIM) image of GNR channel irradiation with two square with same dimension.

Chapter 7

Bibliography

[1] K. S. Novoselov, "Electric field effect in atomically thin carbon films," *Science,* vol. 306, pp. 666-669, // 2004.

[2] K. S. Novoselov, "Two-dimensional gas of massless Dirac fermions in graphene," *Nature,* vol. 438, pp. 197-200, // 2005.

[3] S. Z. Butler, S. M. Hollen, L. Cao, Y. Cui, J. A. Gupta, H. R. Gutiérrez*, et al.*, "Progress, challenges, and opportunities in two-dimensional materials beyond graphene," *ACS nano,* vol. 7, pp. 2898-2926, 2013.

[4] K. Bolotin, K. Sikes, J. Hone, H. Stormer, and P. Kim, "Temperature-dependent transport in suspended graphene," *Physical review letters,* vol. 101, p. 096802, 2008.

[5] C. Lee, X. Wei, J. W. Kysar, and J. Hone, "Measurement of the elastic properties and intrinsic strength of monolayer graphene," *science,* vol. 321, pp. 385-388, 2008.

[6] A. A. Balandin, S. Ghosh, W. Bao, I. Calizo, D. Teweldebrhan, F. Miao*, et al.*, "Superior thermal conductivity of single-layer graphene," *Nano letters,* vol. 8, pp. 902-907, 2008.

[7] D. Reddy, L. F. Register, G. D. Carpenter, and S. K. Banerjee, "Graphene field-effect transistors," *Journal of Physics D: Applied Physics,* vol. 44, p. 313001, 2011.

[8] G. Nanda, S. Goswami, K. Watanabe, T. Taniguchi, and P. F. Alkemade, "Defect control and n-doping of encapsulated graphene by helium-ion-beam irradiation," *Nano letters,* vol. 15, pp. 4006-4012, 2015.

[9] X. Li, X. Wang, L. Zhang, S. Lee, and H. Dai, "Chemically Derived, Ultrasmooth Graphene Nanoribbon Semiconductors," *Science,* vol. 319, pp. 1229-1232, 2008.

[10] A. C. Ferrari, F. Bonaccorso, V. Fal'ko, K. S. Novoselov, S. Roche, P. Boggild*, et al.*, "Science and technology roadmap for graphene, related two-dimensional crystals, and hybrid systems," *Nanoscale,* vol. 7, pp. 4598-4810, 2015.

[11] J. C. Meyer, C. Kisielowski, R. Erni, M. D. Rossell, M. Crommie, and A. Zettl, "Direct imaging of lattice atoms and topological defects in graphene membranes," *Nano letters,* vol. 8, pp. 3582-3586, 2008.

[12] L. Liu, M. Qing, Y. Wang, and S. Chen, "Defects in Graphene: Generation, Healing, and Their Effects on the Properties of Graphene: A Review," *Journal of Materials Science & Technology,* vol. 31, pp. 599-606, 2015/06/01/ 2015.

[13] Z. Ni, L. Ponomarenko, R. Nair, R. Yang, S. Anissimova, I. Grigorieva*, et al.*, "On resonant scatterers as a factor limiting carrier mobility in graphene," *Nano letters,* vol. 10, pp. 3868-3872, 2010.

[14] J.-H. Chen, W. Cullen, C. Jang, M. Fuhrer, and E. Williams, "Defect scattering in graphene," *Physical review letters,* vol. 102, p. 236805, 2009.

[15] D. Van Tuan, J. Kotakoski, T. Louvet, F. Ortmann, J. C. Meyer, and S. Roche, "Scaling properties of charge transport in polycrystalline graphene," *Nano letters,* vol. 13, pp. 1730-1735, 2013.

[16] D. Gunlycke and C. T. White, "Graphene Valley Filter Using a Line Defect," *Physical Review Letters,* vol. 106, p. 136806, 03/28/ 2011.

[17] P. T. Araujo, M. Terrones, and M. S. Dresselhaus, "Defects and impurities in graphene-like materials," *Materials Today,* vol. 15, pp. 98-109, 2012.

[18] R. M. Stöckle, Y. D. Suh, V. Deckert, and R. Zenobi, "Nanoscale chemical analysis by tip-enhanced Raman spectroscopy," *Chemical Physics Letters,* vol. 318, pp. 131-136, 2000.

[19] A. Hartschuh, E. J. Sánchez, X. S. Xie, and L. Novotny, "High-resolution near-field Raman microscopy of single-walled carbon nanotubes," *Physical Review Letters,* vol. 90, p. 095503, 2003.

[20] B. Pettinger, B. Ren, G. Picardi, R. Schuster, and G. Ertl, "Nanoscale probing of adsorbed species by tip-enhanced Raman spectroscopy," *Physical review letters,* vol. 92, p. 096101, 2004.

[21] A. Hartschuh, "Tip-enhanced optical spectroscopy," *Philosophical Transactions of the Royal Society of London A: Mathematical, Physical and Engineering Sciences,* vol. 362, pp. 807-819, 2004.

[22] P. Hung, T. E. O'Loughlin, A. Lewis, R. Dechter, M. Samayoa, S. Banerjee*, et al.*, "Potential application of tip-enhanced Raman spectroscopy (TERS) in semiconductor manufacturing," in *SPIE Advanced Lithography*, 2015, pp. 94241S-94241S-13.

[23] B. Ward, J. A. Notte, and N. Economou, "Helium ion microscope: A new tool for nanoscale microscopy and metrology," *Journal of Vacuum Science & Technology B: Microelectronics and Nanometer Structures Processing, Measurement, and Phenomena,* vol. 24, pp. 2871-2874, 2006.

[24] D. C. Bell, "Contrast mechanisms and image formation in helium ion microscopy," *Microscopy and Microanalysis,* vol. 15, pp. 147-153, 2009.

[25] J. Morgan, J. Notte, R. Hill, and B. Ward, "An introduction to the helium ion microscope," *Microscopy today,* vol. 14, pp. 24-31, 2006.

[26] D. C. Bell, M. C. Lemme, L. A. Stern, J. R. Williams, and C. M. Marcus, "Precision cutting and patterning of graphene with helium ions," *Nanotechnology,* vol. 20, p. 455301, 2009.

[27] D. C. Bell, M. C. Lemme, L. A. Stern, and C. M. Marcus, "Precision material modification and patterning with He ions," *Journal of Vacuum Science & Technology B: Microelectronics and Nanometer Structures Processing, Measurement, and Phenomena,* vol. 27, pp. 2755-2758, 2009.

[28] C. A. Sanford, L. Stern, L. Barriss, L. Farkas, M. DiManna, R. Mello*, et al.*, "Beam induced deposition of platinum using a helium ion microscope," *Journal of Vacuum Science & Technology B: Microelectronics and Nanometer Structures Processing, Measurement, and Phenomena,* vol. 27, pp. 2660-2667, 2009.

[29] M. Melli, A. Polyakov, D. Gargas, C. Huynh, L. Scipioni, W. Bao*, et al.*, "Reaching the theoretical resonance quality factor limit in coaxial plasmonic nanoresonators fabricated by helium ion lithography," *Nano letters,* vol. 13, pp. 2687-2691, 2013.

[30] Y. Wang, M. Abb, S. A. Boden, J. Aizpurua, C. De Groot, and O. L. Muskens, "Ultrafast nonlinear control of progressively loaded, single plasmonic nanoantennas fabricated using helium ion milling," *Nano letters,* vol. 13, pp. 5647-5653, 2013.

[31] O. Scholder, K. Jefimovs, I. Shorubalko, C. Hafner, U. Sennhauser, and G.-L. Bona, "Helium focused ion beam fabricated plasmonic antennas with sub-5 nm gaps," *Nanotechnology,* vol. 24, p. 395301, 2013.

[32] Z. Moktadir, S. Hang, and H. Mizuta, "Defect-induced Fermi level pinning and suppression of ambipolar behaviour in graphene," *Carbon,* vol. 93, pp. 325-334, 11// 2015.

[33] Y.-B. Zhou, Z.-M. Liao, Y.-F. Wang, G. S. Duesberg, J. Xu, Q. Fu*, et al.*, "Ion irradiation induced structural and electrical transition in graphene," *The Journal of chemical physics,* vol. 133, p. 234703, 2010.

[34] G. Nanda, S. Goswami, K. Watanabe, T. Taniguchi, and P. F. A. Alkemade, "Defect Control and n-Doping of Encapsulated Graphene by Helium-Ion-Beam Irradiation," *Nano Letters,* vol. 15, pp. 4006-4012, 2015/06/10 2015.

[35] D. C. Valentina, "Structural and electrical characterization of graphene after ion irradiation," 2010.

[36] P. R. Wallace, "The Band Theory of Graphite," *Physical Review,* vol. 71, pp. 622-634, 05/01/ 1947.

[37] C. Rao, U. Maitra, and H. Matte, "Synthesis, characterization, and selected properties of graphene," *Graphene: Synthesis, Properties, and Phenomena,* pp. 1-47, 2012.

[38] E. Y. Andrei, G. Li, and X. Du, "Electronic properties of graphene: a perspective from scanning tunneling microscopy and magnetotransport," *Reports on Progress in Physics,* vol. 75, p. 056501, 2012.

[39] A. Kumari, N. Prasad, P. K. Bhatnagar, P. C. Mathur, A. K. Yadav, C. V. Tomy*, et al.*, "Electrical transport properties of polycrystalline CVD graphene on SiO2/Si substrate," *Diamond and Related Materials,* vol. 45, pp. 28-33, 2014/05/01/ 2014.

[40] M. E. Schmidt, "Plasma enhanced chemical vapor deposition of nanocrystalline graphene and device fabrication development," University of Southampton, 2012.

[41] J. Wang, R. Zhao, M. Yang, Z. Liu, and Z. Liu, "Inverse relationship between carrier mobility and bandgap in graphene," *The Journal of chemical physics,* vol. 138, p. 084701, 2013.

[42] T. Echtermeyer, M. C. Lemme, J. Bolten, M. Baus, M. Ramsteiner, and H. Kurz, "Graphene field-effect devices," *The European Physical Journal-Special Topics,* vol. 148, pp. 19-26, 2007.

[43] M. C. Lemme, T. J. Echtermeyer, M. Baus, and H. Kurz, "A graphene field-effect device," *IEEE Electron Device Letters,* vol. 28, pp. 282-284, 2007.

[44] A. C. Ferrari and D. M. Basko, "Raman spectroscopy as a versatile tool for studying the properties of graphene," *Nature nanotechnology,* vol. 8, pp. 235-246, 2013.

[45] G.-D. Lee, C. Wang, E. Yoon, N.-M. Hwang, D.-Y. Kim, and K. Ho, "Diffusion, coalescence, and reconstruction of vacancy defects in graphene layers," *Physical review letters,* vol. 95, p. 205501, 2005.

[46] L. Li, S. Reich, and J. Robertson, "Defect energies of graphite: density-functional calculations," *Physical Review B,* vol. 72, p. 184109, 2005.

[47] J. Ma, D. Alfe, A. Michaelides, and E. Wang, "Stone-Wales defects in graphene and other planar s p 2-bonded materials," *Physical Review B,* vol. 80, p. 033407, 2009.

[48] J. Kotakoski, J. Meyer, S. Kurasch, D. Santos-Cottin, U. Kaiser, and A. Krasheninnikov, "Stone-Wales-type transformations in carbon nanostructures driven by electron irradiation," *Physical Review B,* vol. 83, p. 245420, 2011.

[49] A. El-Barbary, R. Telling, C. Ewels, M. Heggie, and P. Briddon, "Structure and energetics of the vacancy in graphite," *Physical Review B,* vol. 68, p. 144107, 2003.

[50] F. Banhart, J. Kotakoski, and A. V. Krasheninnikov, "Structural defects in graphene," *ACS nano,* vol. 5, pp. 26-41, 2010.

[51] M. T. Lusk and L. D. Carr, "Nanoengineering Defect Structures on Graphene," *Physical Review Letters,* vol. 100, p. 175503, 04/30/ 2008.

[52] J. Lahiri, Y. Lin, P. Bozkurt, I. I. Oleynik, and M. Batzill, "An extended defect in graphene as a metallic wire," *Nature nanotechnology,* vol. 5, pp. 326-329, 2010.

[53] N. Kurra, V. S. Bhadram, C. Narayana, and G. Kulkarni, "Field effect transistors and photodetectors based on nanocrystalline graphene derived from electron beam induced carbonaceous patterns," *Nanotechnology,* vol. 23, p. 425301, 2012.

[54] A. Kumar and C. H. Lee, "Synthesis and Biomedical Applications of Graphene: Present and Future Trends," 2013.

[55] A. V. Eletskii, I. M. Iskandarova, A. A. Knizhnik, and D. N. Krasikov, "Graphene: fabrication methods and thermophysical properties," *Physics-Uspekhi,* vol. 54, pp. 227-258, 2011.

[56] J. R. Gong, *Graphene – Synthesis, Characterization, Properties and Applications*: InTech, 2011.

[57] D. Kondo, S. Sato, K. Yagi, N. Harada, M. Sato, M. Nihei*, et al.*, "Low-temperature synthesis of graphene and fabrication of top-gated field effect transistors without using transfer processes," *Applied physics express,* vol. 3, p. 025102, 2010.

[58] P. W. Sutter, J.-I. Flege, and E. A. Sutter, "Epitaxial graphene on ruthenium," *Nature materials,* vol. 7, pp. 406-411, 2008.

[59] I. Pletikosić, M. Kralj, P. Pervan, R. Brako, J. Coraux, A. N'diaye*, et al.*, "Dirac cones and minigaps for graphene on Ir (111)," *Physical Review Letters,* vol. 102, p. 056808, 2009.

[60] X. Li, C. W. Magnuson, A. Venugopal, R. M. Tromp, J. B. Hannon, E. M. Vogel*, et al.*, "Large-area graphene single crystals grown by low-pressure chemical vapor deposition of methane on copper," *Journal of the American Chemical Society,* vol. 133, pp. 2816-2819, 2011.

[61] A. Reina, X. Jia, J. Ho, D. Nezich, H. Son, V. Bulovic*, et al.*, "Large area, few-layer graphene films on arbitrary substrates by chemical vapor deposition," *Nano letters,* vol. 9, pp. 30-35, 2008.

[62] A. Reina, S. Thiele, X. Jia, S. Bhaviripudi, M. S. Dresselhaus, J. A. Schaefer*, et al.*, "Growth of large-area single-and bi-layer graphene by controlled carbon precipitation on polycrystalline Ni surfaces," *Nano Research,* vol. 2, pp. 509-516, 2009.

[63] K. S. Kim, Y. Zhao, H. Jang, S. Y. Lee, J. M. Kim, K. S. Kim*, et al.*, "Large-scale pattern growth of graphene films for stretchable transparent electrodes," *Nature,* vol. 457, pp. 706-710, 2009.

[64] C. Mattevi, H. Kim, and M. Chhowalla, "A review of chemical vapour deposition of graphene on copper," *Journal of Materials Chemistry,* vol. 21, pp. 3324-3334, 2011.

[65] C. Miao, C. Zheng, O. Liang, and Y.-H. Xie, "Chemical vapor deposition of graphene," *Physics and applications of graphene-experiments,* p. 2011, 2011.

[66] L. Liao, Y.-C. Lin, M. Bao, R. Cheng, J. Bai, Y. Liu*, et al.*, "High-speed graphene transistors with a self-aligned nanowire gate," *Nature,* vol. 467, pp. 305-308, 2010.

[67] R. Cheng, J. Bai, L. Liao, H. Zhou, Y. Chen, L. Liu*, et al.*, "High-frequency self-aligned graphene transistors with transferred gate stacks," *Proceedings of the National Academy of Sciences,* vol. 109, pp. 11588-11592, 2012.

[68] C. Chen, S. Rosenblatt, K. I. Bolotin, W. Kalb, P. Kim, I. Kymissis*, et al.*, "Performance of monolayer graphene nanomechanical resonators with electrical readout," *Nature nanotechnology,* vol. 4, pp. 861-867, 2009.

[69] K. M. Milaninia, M. A. Baldo, A. Reina, and J. Kong, "All graphene electromechanical switch fabricated by chemical vapor deposition," *Applied Physics Letters,* vol. 95, p. 183105, 2009.

[70] S. M. Kim, E. B. Song, S. Lee, S. Seo, D. H. Seo, Y. Hwang*, et al.*, "Suspended few-layer graphene beam electromechanical switch with abrupt on-off characteristics and minimal leakage current," *Applied Physics Letters,* vol. 99, p. 023103, 2011.

[71] J. Kotakoski, A. Krasheninnikov, U. Kaiser, and J. Meyer, "From point defects in graphene to two-dimensional amorphous carbon," *Physical Review Letters,* vol. 106, p. 105505, 2011.

[72] B. W. Smith and D. E. Luzzi, "Electron irradiation effects in single wall carbon nanotubes," *Journal of Applied Physics,* vol. 90, pp. 3509-3515, 2001.

[73] E. Bailo and V. Deckert, "Tip-enhanced Raman scattering," *Chemical Society Reviews,* vol. 37, pp. 921-930, 2008.

[74] A. Eckmann, A. Felten, A. Mishchenko, L. Britnell, R. Krupke, K. S. Novoselov*, et al.*, "Probing the Nature of Defects in Graphene by Raman Spectroscopy," *Nano Letters,* vol. 12, pp. 3925-3930, 2012/08/08 2012.

[75] L. G. Cançado, A. Jorio, E. M. Ferreira, F. Stavale, C. Achete, R. Capaz*, et al.*, "Quantifying defects in graphene via Raman spectroscopy at different excitation energies," *Nano letters,* vol. 11, pp. 3190-3196, 2011.

[76] C. Casiraghi, A. Hartschuh, H. Qian, S. Piscanec, C. Georgi, A. Fasoli*, et al.*, "Raman spectroscopy of graphene edges," *Nano Letters,* vol. 9, pp. 1433-1441, 2009.

[77] Z. H. Ni, T. Yu, Y. H. Lu, Y. Y. Wang, Y. P. Feng, and Z. X. Shen, "Uniaxial strain on graphene: Raman spectroscopy study and band-gap opening," *ACS nano,* vol. 2, pp. 2301-2305, 2008.

[78] T. Mohiuddin, A. Lombardo, R. Nair, A. Bonetti, G. Savini, R. Jalil*, et al.*, "Uniaxial strain in graphene by Raman spectroscopy: G peak splitting, Grüneisen parameters, and sample orientation," *Physical Review B,* vol. 79, p. 205433, 2009.

[79] S. Hang, Z. Moktadir, and H. Mizuta, "Raman study of damage extent in graphene nanostructures carved by high energy helium ion beam," *Carbon,* vol. 72, pp. 233-241, 2014.

[80] DasA, PisanaS, ChakrabortyB, PiscanecS, S. K. Saha, U. V. Waghmare*, et al.*, "Monitoring dopants by Raman scattering in an electrochemically top-gated graphene transistor," *Nat Nano,* vol. 3, pp. 210-215, 04//print 2008.

[81] M. M. Lucchese, F. Stavale, E. M. Ferreira, C. Vilani, M. Moutinho, R. B. Capaz*, et al.*, "Quantifying ion-induced defects and Raman relaxation length in graphene," *Carbon,* vol. 48, pp. 1592-1597, 2010.

[82] "Archiv fur Mikroskopische Anatomie. Bd. III, heft iii. Supplementary Notice," *Journal of Microscopy,* vol. 145, pp. 27-51, 1987.

[83] A. Eckmann, A. Felten, I. Verzhbitskiy, R. Davey, and C. Casiraghi, "Raman study on defective graphene: Effect of the excitation energy, type, and amount of defects," *Physical Review B,* vol. 88, p. 035426, 2013.

[84] S. Nie and S. R. Emory, "Probing single molecules and single nanoparticles by surface-enhanced Raman scattering," *science,* vol. 275, pp. 1102-1106, 1997.

[85] M. S. Anderson, "Locally enhanced Raman spectroscopy with an atomic force microscope," *Applied Physics Letters,* vol. 76, pp. 3130-3132, 2000.

[86] W. Sun and Z. Shen, "A practical nanoscopic Raman imaging technique realized by near-field enhancement," *Materials Physics and Mechanics,* vol. 4, pp. 17-21, 2001.

[87] H. Hanafusa, N. Hirose, A. Kasamatsu, T. Mimura, T. Matsui, H. M. Chong*, et al.*, "Strain distribution analysis of sputter-formed strained Si by tip-enhanced Raman spectroscopy," *Applied physics express,* vol. 4, p. 025701, 2011.

[88] J. Stadler, T. Schmid, and R. Zenobi, "Nanoscale chemical imaging of single-layer graphene," *ACS nano,* vol. 5, pp. 8442-8448, 2011.

[89] P. Wang, D. Zhang, L. Li, Z. Li, L. Zhang, and Y. Fang, "Reversible defect in graphene investigated by Tip-enhanced Raman spectroscopy," *Plasmonics,* vol. 7, pp. 555-561, 2012.

[90] R. H. Rickman and P. R. Dunstan, "Enhancement of lattice defect signatures in graphene and ultrathin graphite using tip-enhanced Raman spectroscopy," *Journal of Raman Spectroscopy,* vol. 45, pp. 15-21, 2014.

[91] S. Vantasin, I. Tanabe, Y. Tanaka, T. Itoh, T. Suzuki, Y. Kutsuma*, et al.*, "Tip-Enhanced Raman Scattering of the Local Nanostructure of Epitaxial Graphene Grown on 4H-SiC (000$\bar{1}$)," *The Journal of Physical Chemistry C,* vol. 118, pp. 25809-25815, 2014/11/06 2014.

[92] F. Tuinstra and J. L. Koenig, "Raman spectrum of graphite," *The Journal of Chemical Physics,* vol. 53, pp. 1126-1130, 1970.

[93] A. Das, S. Pisana, B. Chakraborty, S. Piscanec, S. Saha, U. Waghmare*, et al.*, "Monitoring dopants by Raman scattering in an electrochemically top-gated graphene transistor," *Nature nanotechnology,* vol. 3, pp. 210-215, 2008.

[94] Y. Saito, P. Verma, K. Masui, Y. Inouye, and S. Kawata, "Nano-scale analysis of graphene layers by tip-enhanced near-field Raman spectroscopy," *Journal of Raman Spectroscopy,* vol. 40, pp. 1434-1440, 2009.

[95] V. Snitka, R. D. Rodrigues, and V. Lendraitis, "Novel gold cantilever for nano-Raman spectroscopy of graphene," *Microelectronic Engineering,* vol. 88, pp. 2759-2762, 2011.

[96] K. Ikeda, M. Takase, N. Hayazawa, S. Kawata, K. Murakoshi, and K. Uosaki, "Plasmonically Nanoconfined Light Probing Invisible Phonon Modes in Defect-Free Graphene," *Journal of the American Chemical Society,* vol. 135, pp. 11489-11492, 2013/08/07 2013.

[97] W. Su and D. Roy, "Visualizing graphene edges using tip-enhanced Raman spectroscopy," *Journal of Vacuum Science & Technology B,* vol. 31, p. 041808, 2013.

[98] R. Beams, L. G. Cançado, A. Jorio, A. N. Vamivakas, and L. Novotny, "Tip-enhanced Raman mapping of local strain in graphene," *Nanotechnology,* vol. 26, p. 175702, 2015.

[99] F. Pashaee, F. Sharifi, G. Fanchini, and F. Lagugné-Labarthet, "Tip-enhanced Raman spectroscopy of graphene-like and graphitic platelets on ultraflat gold nanoplates," *Physical Chemistry Chemical Physics,* 2015.

[100] M. Ghislandi, G. G. Hoffmann, E. Tkalya, L. Xue, and G. D. With, "Tip-Enhanced Raman Spectroscopy and Mapping of Graphene Sheets," *Applied Spectroscopy Reviews,* vol. 47, pp. 371-381, 2012.

[101] K. F. Domke and B. Pettinger, "Tip-enhanced Raman spectroscopy of 6H-SiC with graphene adlayers: selective suppression of E1 modes," *Journal of Raman Spectroscopy,* vol. 40, pp. 1427-1433, 2009.

[102] J. Wang, X. Wu, R. Wang, and M. Zhang, "Detection of Carbon Nanotubes Using Tip-Enhanced Raman Spectroscopy," 2011.

[103] J. Wessel, "Surface-enhanced optical microscopy," *JOSA B,* vol. 2, pp. 1538-1541, 1985.

[104] J. Stadler, T. Schmid, and R. Zenobi, "Developments in and practical guidelines for tip-enhanced Raman spectroscopy," *Nanoscale,* vol. 4, pp. 1856-1870, 2012.

[105] N. Anderson, A. Hartschuh, S. Cronin, and L. Novotny, "Nanoscale Vibrational Analysis of Single-Walled Carbon Nanotubes," *Journal of the American Chemical Society,* vol. 127, pp. 2533-2537, 2005/03/01 2005.

[106] A. Hartschuh, "Tip-Enhanced Near-Field Optical Microscopy," *Angewandte Chemie International Edition,* vol. 47, pp. 8178-8191, 2008.

[107] W. Sun and Z. Shen, "Near-field scanning Raman microscopy using apertureless probes," *Journal of Raman Spectroscopy,* vol. 34, pp. 668-676, 2003.

[108] N. Hayazawa, Y. Inouye, Z. Sekkat, and S. Kawata, "Metallized tip amplification of near-field Raman scattering," *Optics Communications,* vol. 183, pp. 333-336, 2000.

[109] J. Steidtner and B. Pettinger, "Tip-enhanced Raman spectroscopy and microscopy on single dye molecules with 15 nm resolution," *Physical Review Letters,* vol. 100, p. 236101, 2008.

[110] D. A. Long and P. A. Curran, "BOOK TOOLS," *Vectors,* vol. 1, pp. 381-406, 2002.

[111] S. RAOOF. ((2009/2010 6). 6 June

). *Waves around us*. Available: http://shariqa.com/waves%20around%20us.htm

[112] N. Kumar, S. Mignuzzi, W. Su, and D. Roy, "Tip-enhanced Raman spectroscopy: principles and applications," *EPJ Techniques and Instrumentation,* vol. 2, p. 9, 2015.

[113] C. L. Haynes, A. D. McFarland, and R. P. V. Duyne, "Surface-enhanced Raman spectroscopy," *Analytical Chemistry,* vol. 77, pp. 338 A-346 A, 2005.

[114] E. Bailo and V. Deckert, "Tip-Enhanced Raman Spectroscopy of Single RNA Strands: Towards a Novel Direct-Sequencing Method," *Angewandte Chemie International Edition,* vol. 47, pp. 1658-1661, 2008.

[115] A. Hartschuh, "Tip-Enhanced Near-Field Optical Microscopy," *Angewandte Chemie International Edition,* vol. 47, pp. 8178-8191, 2008.

[116] W. Zhang, H. Fischer, T. Schmid, R. Zenobi, and O. J. F. Martin, "Mode-Selective Surface-Enhanced Raman Spectroscopy Using Nanofabricated Plasmonic Dipole Antennas," *The Journal of Physical Chemistry C,* vol. 113, pp. 14672-14675, 2009/08/20 2009.

[117] W. Zhang, H. Fischer, T. Schmid, R. Zenobi, and O. J. Martin, "Mode-selective surface-enhanced Raman spectroscopy using nanofabricated plasmonic dipole antennas," *The Journal of Physical Chemistry C,* vol. 113, pp. 14672-14675, 2009.

[118] B. Pettinger, B. Ren, G. Picardi, R. Schuster, and G. Ertl, "Tip-enhanced Raman spectroscopy (TERS) of malachite green isothiocyanate at Au(111): bleaching behavior under the influence of high electromagnetic fields," *Journal of Raman Spectroscopy,* vol. 36, pp. 541-550, 2005.

[119] W. Zhang, B. S. Yeo, T. Schmid, and R. Zenobi, "Single molecule tip-enhanced Raman spectroscopy with silver tips," *The Journal of Physical Chemistry C,* vol. 111, pp. 1733-1738, 2007.

[120] G. SUPERMARKT. (2009, 07 Feb). *Monolayer Graphene on 285 nm SiO2 Wafer: 5 pack*. Available: https://graphene-supermarket.com/Monolayer-Graphene-on-a--285-nm-Silicon-Dioxide-Wafer-5-pack.html

[121] A. C. Ferrari, "Raman spectroscopy of graphene and graphite: disorder, electron–phonon coupling, doping and nonadiabatic effects," *Solid State Communications,* vol. 143, pp. 47-57, 2007.

[122] A. C. Ferrari, J. C. Meyer, V. Scardaci, C. Casiraghi, M. Lazzeri, F. Mauri*, et al.*, "Raman Spectrum of Graphene and Graphene Layers," *Physical Review Letters,* vol. 97, p. 187401, 10/30/ 2006.

[123] S. Niyogi, E. Bekyarova, M. E. Itkis, H. Zhang, K. Shepperd, J. Hicks*, et al.*, "Spectroscopy of covalently functionalized graphene," *Nano letters,* vol. 10, pp. 4061-4066, 2010.

[124] A. C. Ferrari, "Raman spectrum of graphene and graphene layers," *Phys. Rev. Lett.,* vol. 97, p. 187401, // 2006.

[125] A. Ferrari, J. Meyer, V. Scardaci, C. Casiraghi, M. Lazzeri, F. Mauri*, et al.*, "The Raman fingerprint of graphene," *arXiv preprint cond-mat/0606284,* 2006.

[126] B. Vasić, M. Kratzer, A. Matković, A. Nevosad, U. Ralević, D. Jovanović*, et al.*, "Atomic force microscopy based manipulation of graphene using dynamic plowing lithography," *Nanotechnology,* vol. 24, p. 015303, 2013.

[127] M. Dresselhaus, A. Jorio, A. Souza Filho, and R. Saito, "Defect characterization in graphene and carbon nanotubes using Raman spectroscopy," *Philosophical Transactions of the Royal Society of London A: Mathematical, Physical and Engineering Sciences,* vol. 368, pp. 5355-5377, 2010.

[128] H. Li, L. Daukiya, S. Haldar, A. Lindblad, B. Sanyal, O. Eriksson*, et al.*, "Site-selective local fluorination of graphene induced by focused ion beam irradiation," *Scientific reports,* vol. 6, p. 19719, 2016.

[129] A. E. Vladár, M. T. Postek, and B. Ming, "On the sub-nanometer resolution of scanning electron and helium ion microscopes," *Microscopy Today,* vol. 17, 2009.

[130] L. Scipioni, L. Stern, J. Notte, S. Sijbrandij, and B. Griffin, "Helium ion microscope," *Advanced Materials and Processes,* vol. 166, p. 27, 2008.

[131] G. Ostrovsky. (6 June). *The Orion Helium Ion Microscope*. Available: https://www.medgadget.com/2007/09/the_orion_helium_ion_microscope.html

[132] K. Sherer. (6 June). *ORION helium ion microscope*. Available: http://www.gizmag.com/go/8262/

[133] J. Notte, B. Ward, N. Economou, R. Hill, R. Percival, L. Farkas*, et al.*, "An introduction to the helium ion microscope," in *AIP Conference Proceedings*, 2007, pp. 489-496.

[134] M. T. Postek, A. E. Vladar, J. Kramar, L. A. Stern, J. Notte, S. McVey*, et al.*, "Helium ion microscopy: a new technique for semiconductor metrology and nanotechnology," in *AIP Conference Proceedings*, 2007, pp. 161-167.

[135] D. Cohen-Tanugi and N. Yao, "Superior imaging resolution in scanning helium-ion microscopy: A look at beam-sample interactions," *Journal of Applied Physics,* vol. 104, p. 063504, 2008.

[136] M. C. Prado, D. Jariwala, T. J. Marks, and M. C. Hersam, "Optimization of graphene dry etching conditions via combined microscopic and spectroscopic analysis," *Applied Physics Letters,* vol. 102, p. 193111, 2013.

[137] S. Engels, A. Epping, C. Volk, S. Korte, B. Voigtländer, K. Watanabe*, et al.*, "Etched graphene quantum dots on hexagonal boron nitride," *Applied Physics Letters,* vol. 103, p. 073113, 2013.

[138] M. Irannejad, W. Alyalak, S. Burzhuev, A. Brzezinski, and M. Bo, "Engineering of Bi−/monolayer graphene film using reactive ion etching," *Trans Electr Electron Mater,* vol. 16, pp. 169-172, 2015.

[139] L.-J. Wang, H.-O. Li, T. Tu, G. Cao, C. Zhou, X.-J. Hao*, et al.*, "Controllable tunnel coupling and molecular states in a graphene double quantum dot," *Applied Physics Letters,* vol. 100, p. 022106, 2012.

[140] H. Al-Mumen, F. Rao, W. Li, and L. Dong, "Singular sheet etching of graphene with oxygen plasma," *Nano-Micro Letters,* vol. 6, pp. 116-124, 2014.

[141] L.-J. Wang, G.-P. Guo, D. Wei, G. Cao, T. Tu, M. Xiao*, et al.*, "Gates controlled parallel-coupled double quantum dot on both single layer and bilayer graphene," *Applied Physics Letters,* vol. 99, p. 112117, 2011.

[142] L.-J. Wang, H.-O. Li, T. Tu, G. Cao, C. Zhou, X.-J. Hao*, et al.*, "Controllable tunnel coupling and molecular states in a graphene double quantum dot," *Applied Physics Letters,* vol. 100, p. 022106, 2012.

[143] C. Stampfer, J. Güttinger, F. Molitor, D. Graf, T. Ihn, and K. Ensslin, "Tunable Coulomb blockade in nanostructured graphene," *Applied Physics Letters,* vol. 92, p. 012102, 2008.

[144] M. M. TECHNOLOGIES, "UVN™30 NEGATIVE DUV PHOTORESIST," ed, 2004.

[145] C. Lee, J. Kim, S. Kim, Y. J. Chang, K. S. Kim, B. Hong*, et al.*, "Strong hole-doping and robust resistance-decrease in proton-irradiated graphene," vol. 6, p. 21311, 02/18/online 2016.

[146] M. S. Dresselhaus, A. Jorio, M. Hofmann, G. Dresselhaus, and R. Saito, "Perspectives on carbon nanotubes and graphene Raman spectroscopy," *Nano letters,* vol. 10, pp. 751-758, 2010.

[147] T. Iwasaki, T. Zelai, S. Ye, Y. Tsuchiya, H. M. Chong, and H. Mizuta, "Local hole doping concentration modulation on graphene probed by tip-enhanced Raman spectroscopy," *Carbon,* vol. 111, pp. 67-73, 2017.

[148] Z. H. Ni, H. M. Wang, Z. Q. Luo, Y. Y. Wang, T. Yu, Y. H. Wu*, et al.*, "The effect of vacuum annealing on graphene," *Journal of Raman Spectroscopy,* vol. 41, pp. 479-483, 2010.

[149] B. Krauss, T. Lohmann, D.-H. Chae, M. Haluska, K. von Klitzing, and J. H. Smet, "Laser-induced disassembly of a graphene single crystal into a nanocrystalline network," *Physical Review B,* vol. 79, p. 165428, 2009.

[150] L. Tao, C. Qiu, F. Yu, H. Yang, M. Chen, G. Wang*, et al.*, "Modification on single-layer graphene induced by low-energy electron-beam irradiation," *The Journal of Physical Chemistry C,* vol. 117, pp. 10079-10085, 2013.

[151] A. C. Ferrari and J. Robertson, "Interpretation of Raman spectra of disordered and amorphous carbon," *Physical review B,* vol. 61, p. 14095, 2000.

[152] J. E. Lee, G. Ahn, J. Shim, Y. S. Lee, and S. Ryu, "Optical separation of mechanical strain from charge doping in graphene," *arXiv preprint arXiv:1209.0234,* 2012.